博士論文

Investigation of Microstructure Evolutions in 12Cr-ODS Steel under Electron Irradiations

(電子照射下における 12Cr-ODS 鋼の微細組織変化に関する研究)

呉　宣怜
OH Sun-Ryung

Table of Contents

Abstract

Oxide Dispersion Strengthened (ODS) steels are promising structural material for fusion reactors due to both excellent mechanical strength and irradiation resistance. A high number density of the dispersed Y-Ti-O nanoparticles (NPs), mainly $Y_2Ti_2O_7$ and Y_2TiO_5, embedded in the Fe-Cr matrix contributes to enhancement in high-temperature creep strength and irradiation resistance. To implement ODS steels in fusion reactors like DEMO, the stability of the Y-Ti-O NPs under high-temperature irradiation is critical. According to previous literature, based on different radiation sources and the chemical composition of the irradiated materials, the radiation response of the NPs differed. For instance, under neutron irradiation on 13Cr-ODS steel, NPs were stable; while under electron and Fe^{+2} ion irradiations on 9Cr-ODS steel, NPs were shrinking. To clarify the radiation response of NPs, three factors were controlled in this research: radiation energy, temperature, and electron beam condition. At different irradiation conditions, microstructural evolutions were closely investigated under in-situ Transmission Electron Microscope (TEM).

Firstly, the microstructural evolutions of Y-Ti-O NPs in ferritic 12Cr-ODS steel under high energy electron irradiations were investigated using H-3000 at Osaka University. From the previous research, the displacement threshold energy of Y in Y_2O_3 is reported as 57 eV and electron energy above 1.25 MeV can dissolve Y_2O_3 as its displacement threshold energy of Y is 64 eV. Thus, in this research, 2 MeV electron energy is used to irradiate the ODS steel. Under 2 MeV electron energy, irradiations were performed at 723K and 823K to investigate the temperature effect on NPs dissolution. Also, under both irradiation temperatures, electron beam conditions - focused and uniform - were controlled to study the vacancy concentration gradient effect on NPs.

The focused beam technique was employed to study the effect of vacancy concentration gradient where the electron beam intensity has a Gaussian distribution. The NPs volumetric change under the focused and the uniform beam conditions were compared throughout the irradiations with the irradiation time step as short as 60 s. Also, for each NP, both the size and shape evolution were investigated throughout the short-time irradiation steps. Unlike the typically reported monotonic size change of nanoparticles, both rapid growth and shrinkage were observed simultaneously under 723K irradiation in each time step. In both the focused and the uniform beam irradiations, this stochastic size change behavior of NPs at the early irradiation stage is first reported in this study. Contrary to 723K irradiation results, at 823K uniform irradiation, the radiation-induced growth phenomenon was observed. The morphological evolution along with growth was also observed: regardless of initial shape of NPs, the final shape was either cuboidal or polygon.

Lastly, for the in-depth study on the instability mechanism of NPs, the single particle irradiation is performed using JEM-ARM1300 at Hokkaido University. The dissolution mechanism for the NP is investigated using this in-situ High Resolution TEM (HRTEM). It was operated at 1.25 MeV with irradiation temperature at 573K. From Fast Fourier Transformation (FFT) of the single nanoparticle, diffraction patterns are acquired time-sequentially.

Two patterns from the FFT are analyzed and the detected diffraction patterns could indicate that the nanoparticle is composed of two layers with shell-like structure. Area

corresponding to the interface between the NP and bulk was selected to closely investigate the dislocation movement under the electron irradiation. Through Inverse Fast Fourier Transformation (IFFT) analysis, the change in interplanar distance was found from spacing measurements of lattice fringes. Based on the analysis, the structural vacancies in the NP before irradiation are confirmed and irradiation induced dislocation motion enhancement is concluded to be a mechanism for the particle dissolution.

CHAPTER 1

Introduction

The world is built upon energy-intensive industries and the needed energies are vastly supplied by power plants operated by fossil fuels – coal, natural gas, and oil. The usage of fossil fuels has caused carbon emission and the subsequent result of overusing fossil fuels is indicating global climate change. Since 1951 to 2010, the increase of global mean surface temperature due to human activities is estimated at 0.5 to 1.3 °C [1]. Climate change has gathered countries to discuss and implement policies to reduce carbon emission at the national down to the regional level. From the Framework Convention on Climate Change (UNFCCC) (1992), the Kyoto Protocol (1997), and the Paris agreement (2015). However, global carbon emission is annually increasing with most developed countries being the major carbon-emitting countries as shown in both Fig.1.1 and 1.2, and developing countries still need tremendous energy to support their growing domestic industries.

To maintain the supply of the world's current energy consumption, under the fossil fuel power plants, the world will most likely to face acceleration of climate change. Instead, nuclear power presents advantages in energy generation due to its incomparably high energy density compares to other sources of energy. Also, nuclear energy is clean energy as nuclear reactors do not produce any carbon or greenhouse gases.

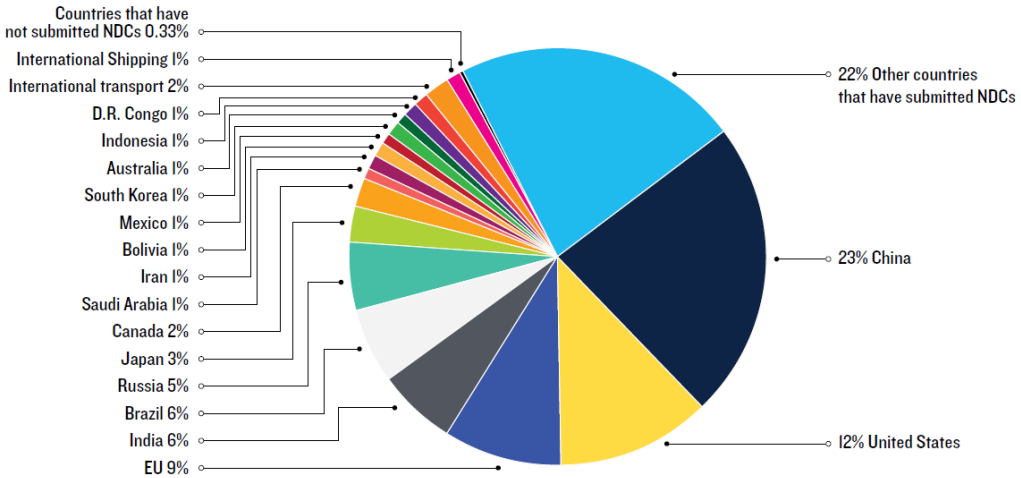

Fig. 1.1 Total greenhouse gas emissions in the world for 2012 [1].

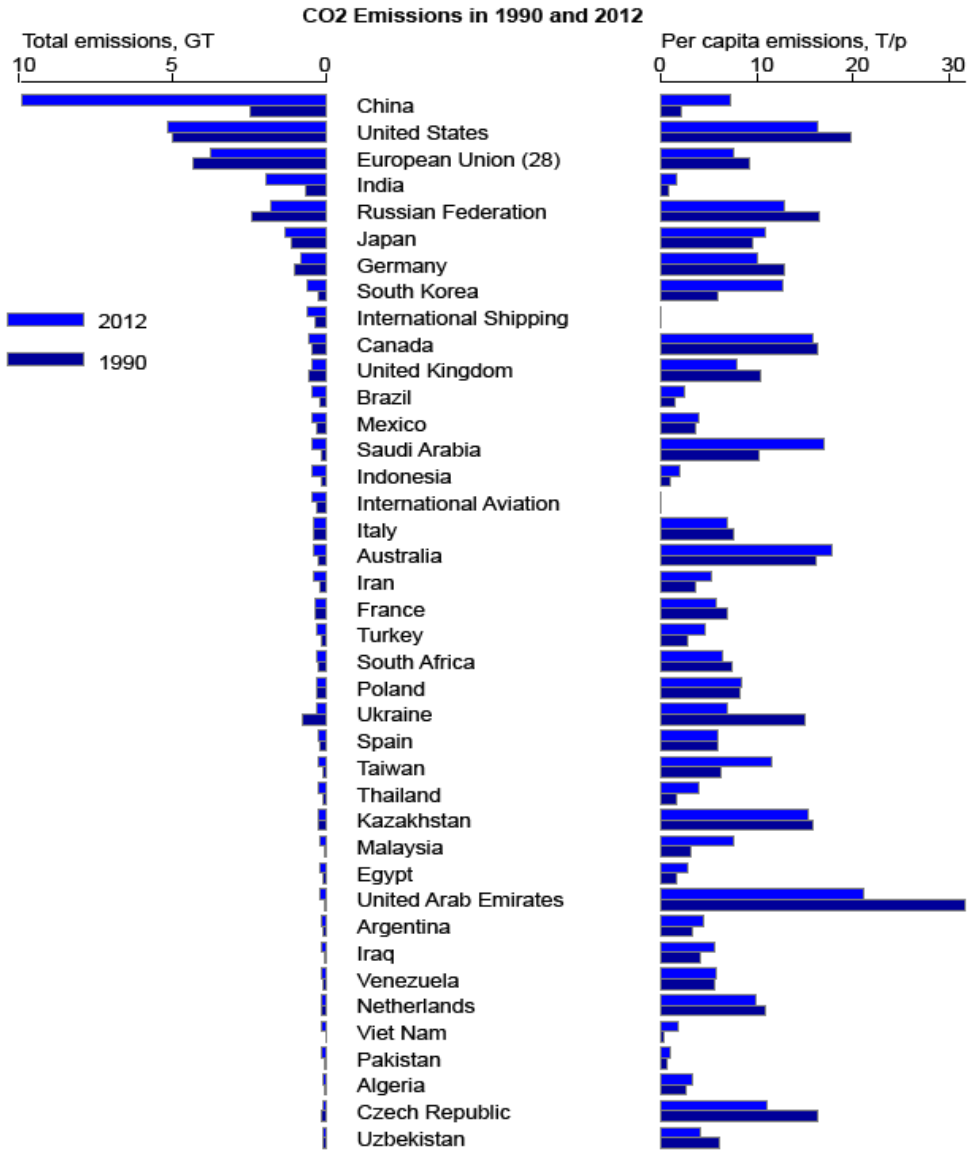

Fig. 1.2 Top 40 carbon emitting countries in the world from 1990 to 2012 [2].

Regardless of incomparably high-power output and zero greenhouse gases emission by nuclear reactors, the nuclear industry is still facing several obstacles to be widely constructed and potentially replace fossil fuel. As a commercial type reactor, nuclear fission reactors are widely operating which produce radioactive wastes that require mostly land burial. Also, the usage of uranium and plutonium which are fissile materials poses the risk of nuclear proliferation that can lead to potential terrorism. Public discomfort and fear of nuclear energy exist due to several major nuclear accidents – Three Mile Island, Chernobyl, and Fukushima.

Nuclear fusion can overcome many disadvantages of nuclear fission. From the safety perspective, in case of emergency, the plasma instantly cools down and the reaction stops; thus, the previously occurred catastrophic nuclear accidents which involved reactor core meltdown can never happen in nuclear fusion.

1.1 Principle of Nuclear Fusion

Unlike nuclear fission which produces heat by the splitting of heavy radioactive atoms, nuclear fusion produces energy by deuterium-tritium reaction. The fusion of hydrogen o helium in the Sun and other stars occurs in three stages. First, two ordinary hydrogen nuclei (1H), which are actually just single protons, fuse to form an isotope of hydrogen called deuterium (2H), which contains one proton and one neutron. A positron (e^+) and a neutrino (ν) are also produced. The positron is very quickly annihilated in the collision with an electron, and the neutrino travels right out of the Sun:

$$^1H + {}^1H \rightarrow {}^2H + e^+ + \nu \qquad (1.1.1)$$

Once created, the deuterium fuses with yet another hydrogen nucleus to produce ^{3}He—an isotope of ^{4}He. At the same time, a high-energy photon, or γ ray, is produced. The reaction is

$$^2H + {}^1H \rightarrow {}^3He + \gamma \qquad (1.1.2)$$

The final step in the reaction chain, which is called the proton-proton cycle, takes place when a second 3He nucleus, created in the same way as the first, collides and fuses with another ^{3}He, forming ^{4}He and two protons. In symbols,

$$^3He + {}^3He \rightarrow {}^4He + 2\,{}^1H \qquad (1.1.3)$$

The net result of the proton-proton cycle is that four hydrogen nuclei combine to create one helium nucleus. The mass of the end product is 0.0475 x 10^{27} kg less than the combined mass of the ^{3}He nuclei. This mass difference, known as mass defect in the parlance of nuclear physics, is converted into 26.7 MeV of energy as known from Einstein's equation E = mc^2. Among the various possible fusion reactions, the important reactions are described in below the Table 1.1.

Table 1.1 Energy release Q and cross sections at 10 keV and 100 keV center of mass energy for some important fusion reaction that can be employed in future fusion reactors.

Reaction	Q [MeV]	σ (10keV) [barn]	σ (100keV) [barn]
$p + p \rightarrow D + e^+ + \nu$	1.44	$(3.6 \cdot 10^{-26})$	$(4.4 \cdot 10^{-25})$
$D + D \rightarrow T + p$	4.04	$2.81 \cdot 10^{-4}$	$3.3 \cdot 10^{-2}$
$D + D \rightarrow {}^3He + n$	3.27	$2.78 \cdot 10^{-4}$	$3.7 \cdot 10^{-2}$
$D + T \rightarrow \alpha + n$	17.59	$2.72 \cdot 10^{-2}$	3.43
$D + {}^3He \rightarrow \alpha + p$	18.35	$2.2 \cdot 10^{-7}$	0.1
$T + T \rightarrow \alpha + 2n$	11.33	$7.9 \cdot 10^{-4}$	$3.4 \cdot 10^{-2}$
$p + {}^6Li \rightarrow \alpha + {}^3He$	4.02	$6 \cdot 10^{-10}$	$7 \cdot 10^{-3}$
$p + {}^12C \rightarrow {}^{13}N + \gamma$	1.94	$(1.9 \cdot 10^{-26})$	$2.0 \cdot 10^{-10}$

1.2 Development of Fusion Reactor: ITER and DEMO

Generation and confinement of very high-temperature plasmas are still extremely challenging tasks in nuclear fusion industry. To reach the final goal of stable and reliable electricity production for commercial purpose, through international collaboration, seven-member entities (the European Union, India, Japan, China, Russia, South Korea, and the United

States) have decided to lead the fusion reactor study by creating an experimental fusion reactor called ITER (International Thermonuclear Experimental Reactor). Also, starting from the ITER project, DEMO (DEMOnstration power plant) is planned to integrate technological outcomes from the ITER and bring the nuclear fusion from experimental level to industry level as the first electricity demonstration power plant as shown in Fig. 1.2.1 through 1.2.3. As the target of ITER and DEMO differs, the main differences are organized as shown in Table 1.2.

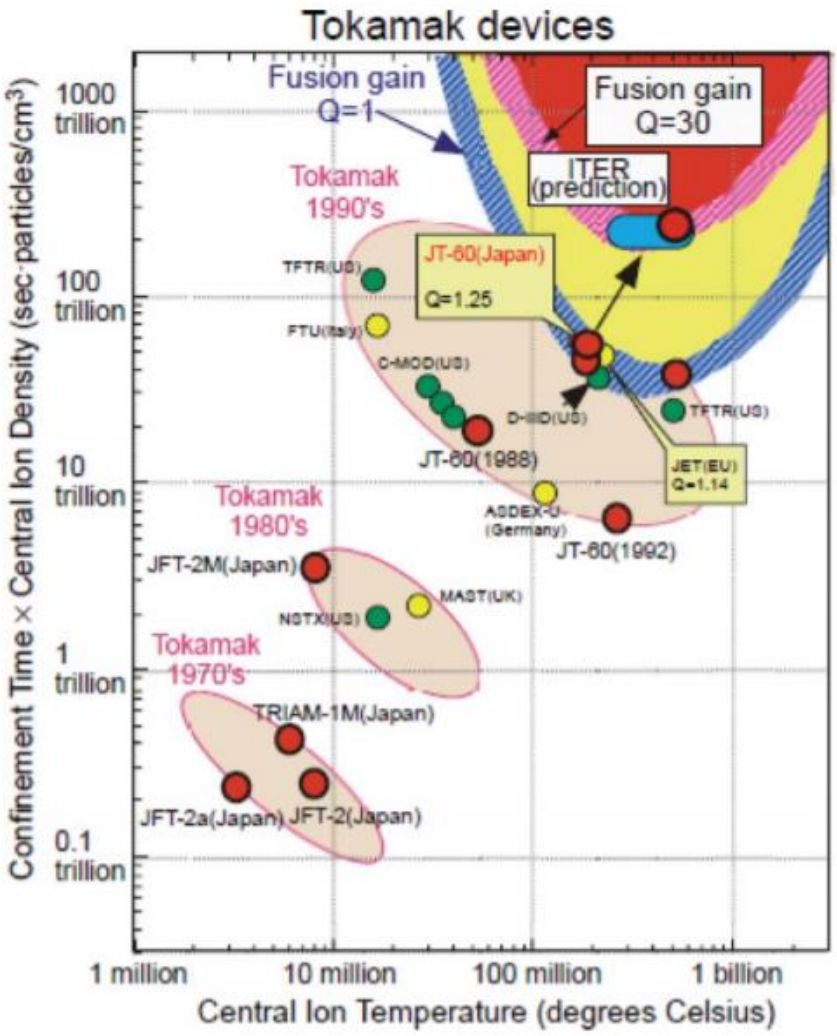

Fig. 1.2.1 Plasma performance progress towards fusion reactors [3].

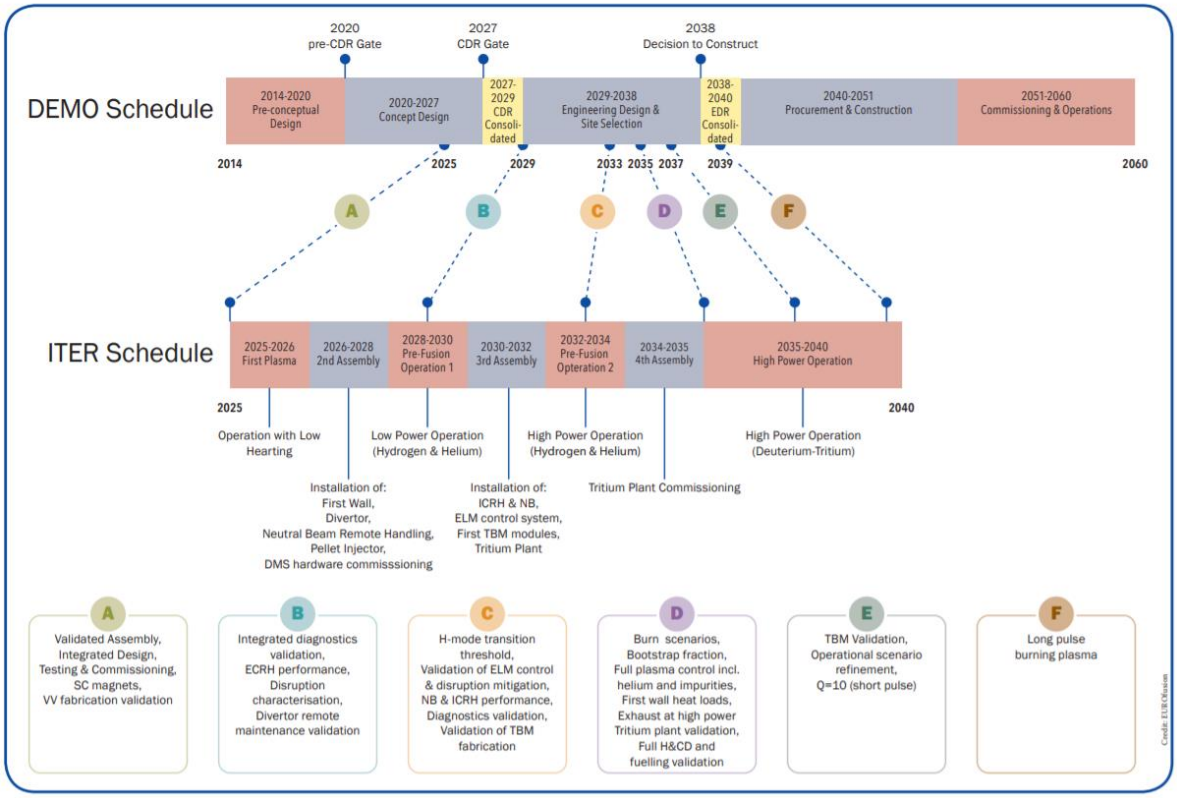

Fig. 1.2.2 Timeline for developing ITER and DEMO [4].

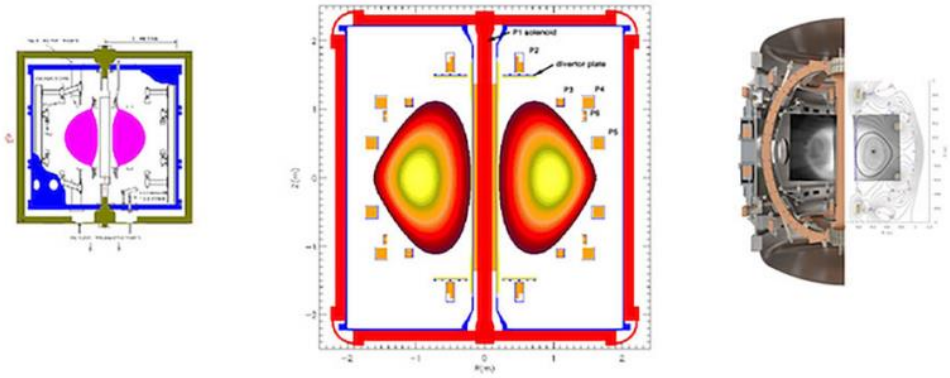

	START	MAST	ST40
major radius R_0	~0.32 m	~0.8 m	0.4 m
aspect ratio R/a	1.3	1.3	1.8
max centre column current	0.5 MA	2.2 MA	6 MA
max $B_t(R_0)$	0.31 T	0.55 T	3 T
plasma current I_p	<310 kA	1.35 MA	target 2 MA

Fig. 1.2.3 Images of the START, MAST and ST40STs and their main parameters [5].

The basic design for ITER and DEMO is similar, but there is an intrinsic difference of self-breed tritium through tritium breeding blanket which only DEMO can accomplish. The blanket system provides a physical boundary for the plasma transients and contributes to the thermal and nuclear shielding of the vacuum vessel and external ITER components [1,2]. The main parameters for various DEMO reactors are shown in the above Fig. 1.2. It covers ∼600 m^2 and consists of blanket modules (BM) comprising two major components: a plasma facing First Wall (FW) panel and a shield block (SB). Each BM is about (1 m × 1.4 m × 0.5 m) and is attached to the vacuum vessel through a mechanical attachment system of flexible supports and a system of keys. Each BM has electrical straps providing electrical connection to the vacuum vessel. As structural material, the target of the R&D programme is the development of a reduce activation (RA) version of the type 8–9CrWVTa able to withstand neutron damage of 70 dpa for the DEMO with target up to 150 dpa for a future fusion power plant (FPP).

The blanket provides the physical boundary for the plasma and shields the vacuum vessel along with other external machine components. Also, each module consists of shield block and first wall. As the blanket will be directly facing the ultra-hot plasma and large electromagnetic forces, it is considered one of the most critical components. Thus, advanced material development for the blanket is important.

Table. 1.2 Main differences between ITER and DEMO [6].

ITER	DEMO
Experimental device with physics and technology missions	Nearer to a commercial power plant, but with some development missions
400 s pulses (some longer at lower power), long dwell time	Long pulse, quasi-steady state
Experimental campaigns. Outages for maintenance and component replacements	Maximize availability
Large number of diagnostics	Only those required for operation
Multiple heating and current drive systems	Fewer
Large design margins, necessitated by uncertainties and lack of fully appropriate design codes	With ITER (and other) experience, design could have smaller uncertainties
Cooling system optimized for minimum stresses and sized for modest heat rejection	Cooling system optimized for electricity generation efficiency (e.g. higher temperature)
Test blanket modules introduce range of diverse concepts	Single blanket concept
Unique one-off design optimized for experimental goals within cost constraints	Move towards design choices suitable for series production
No tritium breeding requirement (except very small quantity in TBMs)	Tritium breeding needed for self-sufficiency
Conventional 316 stainless steel structure	Novel low activation materials as structure (at least for some components)
Very modest lifetime neutron fluence, low dpa and He production	High fluence, significant materials damage
Licensing as experimental facility allows some credit for experimental nature (e.g. no dependence of safety on plasma behaviour)	Stricter approach may be necessary to avoid large design margins
During conceptual design (including "EDA"), licensing in any ITER member country had to be possible	Fewer constraints

CHAPTER 2.

Structural Material in Fusion Reactor: ODS Steel

For nuclear applications of oxide dispersion-strengthened steels, the Cr concentration is between 8 and 14 wt% for the matrix and may expect a α′ precipitation. Typically, based on Schaeffler constitution diagram, 9Cr-ODS steel is ferritic/martensitic with fcc structure; while, 12Cr-ODS steel is ferrite with bcc structure. According to Fig. 2.1 of phase diagram for ODS steel , α′ precipitation occurs at T < 300 °C for 9 wt% of Cr and at T < 450 °C for 14 wt% of Cr [7]. The precipitation may be too slow to be observed during isothermal annealing on accessible times, but it can be strongly accelerated by irradiation, because point defect concentrations may then be higher than the equilibrium ones (by orders of magnitude), leading to much faster diffusion. Besides a strong acceleration, these experiments show few differences in the precipitate microstructure between isothermal aging and irradiation. Moreover, the Cr solubility limit was found to be much higher under irradiation than at equilibrium (≃ 30%, instead of ≃ 9%).

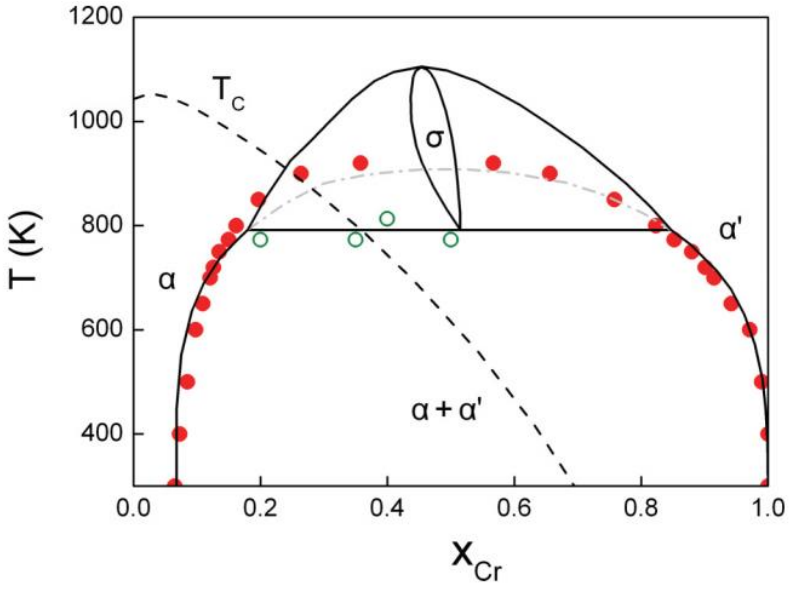

Fig. 2.1 The Fe-Cr phase diagram [8]. The red circles represent the $\alpha - \alpha'$miscibility gap of the present model. The dotted line shows the Curie temperature of the bcc solid solution and the dashed-dotted line represents the metastable part of the miscibility gap.

2.1 Strengthening Mechanism of ODS Steel

Oxide dispersion strengthened (ODS) ferritic steel is one of promising fusion and Generation IV structural materials which exhibit excellent mechanical strength at high temperature and radiation tolerance due to the existence of nanometer-scale oxide dispersoids [9–17]. The examples of excellent mechanical properties are high temperature creep strength, corrosion and oxidation resistance, and irradiation damage resistance. One of the advantages of nanoparticles embedded in the matrix is the Zener pinning effect which retards the motion of both dislocations and grain boundaries thus leads to enhancement of creep resistance and tensile strength [9,11].

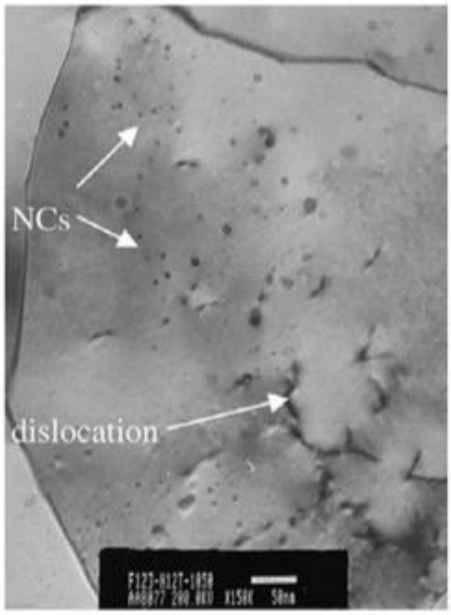

Fig. 2.1.1 Bright field image of dislocations and Y-Ti-O nanoparticles [10].

2.1.1 Microstructure

Microstructures of dispersed nanoparticles in 12Cr-ODS steel are known to have complex structures, and there are mainly three types that can be found: Y_2O_3, Y_2TiO_5, and

$Y_2Ti_2O_7$. Pyrochlore type of $Y_2Ti_2O_7$ is known to be non-stoichiometric which can be decomposed into Y_2TiO_5 and TiO_2. Y-Ti-O nanoparticles have been reported to be both non-stoichiometric and stoichiometric based on their size as their chemical compositions vary. For the non-stoichiometric case of $Y_2Ti_2O_7$, diameter is usually between 2 and 15 nm with Y/Ti ≈ 0.5 being smallest and Y/Ti < 1.0 being larger particle [18]. For near-stoichiometric case, diameter is between 15 to 35 nm with Y/Ti ≈ 1.0. Also, the pyrochlore structure of $Y_2Ti_2O_7$ is known to have oxygen defects inside the structure [19].

Based on literature, ceramics such as Al_2O_3 and Y_2O_3 are possible candidates for inert matrix fuels as the threshold electronic stopping power values are significantly higher than the electronic stopping powers anticipated in fission or fusion reactors [20,21]. Thus, ceramics such as Y_2O_3, Y_2TiO_5, and $Y_2Ti_2O_7$ themselves are suspected to be stable against irradiation due to their complicated structure and difficulty in dislocation motion inside the structure.

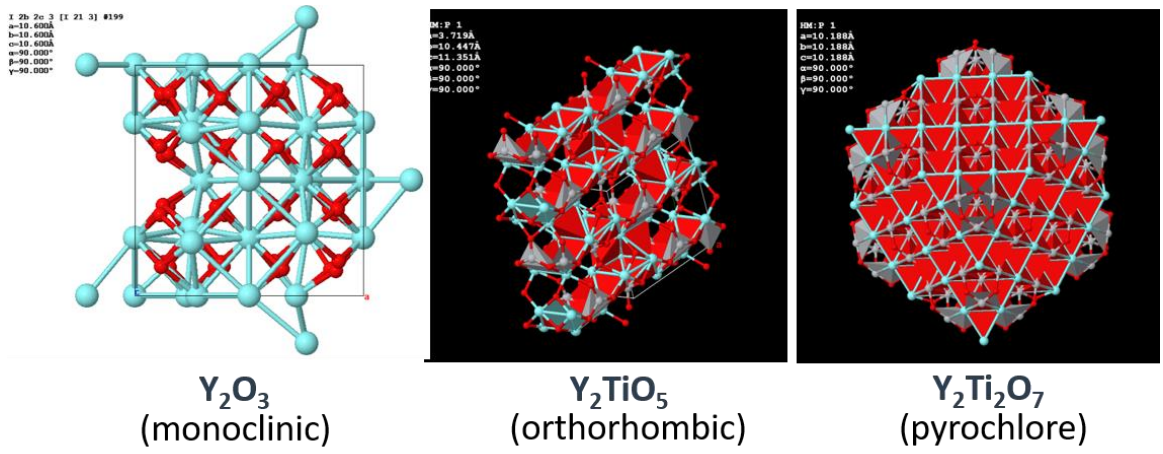

Fig. 2.1.2 Structure of three types of nanoparticles embedded in ODS steel: Y_2O_3, Y_2TiO_5, and $Y_2Ti_2O_7$ [22].

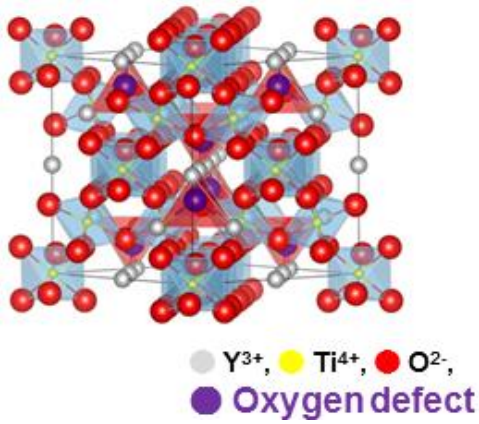

Fig. 2.1.3 Pyrochlore structure of $Y_2Ti_2O_7$ [19].

In this study, microstructure of a ferritic 12Cr-ODS steel with a composition of 12Cr-2W-0.3Ti-0.25Y2O3 (wt%) was investigated which was fabricated at KOBELCO for nuclear applications [23]. In this study, the 12Cr-ODS steel has been 80% recrystallized with an average nanoparticle diameter of 3.5 ± 0.7 nm and number density of 1.3×10^{23} m^3. Through high-angle angular dark- field (HAADF) and energy dispersive spectroscopy (EDS) mapping, the chemical composition of nanoparticles was analyzed and were identified as either Y_2O_3 or Y-Ti-O complex. Furthermore, through high-resolution transmission electron microscope (HRTEM), Y-Ti-O nanoparticles were identified to be orthorhombic- and hexagonal-Y_2TiO_5, and cubic-$Y_2Ti_2O_7$ as shown in Fig. 2.1.2 through 2.1.6.

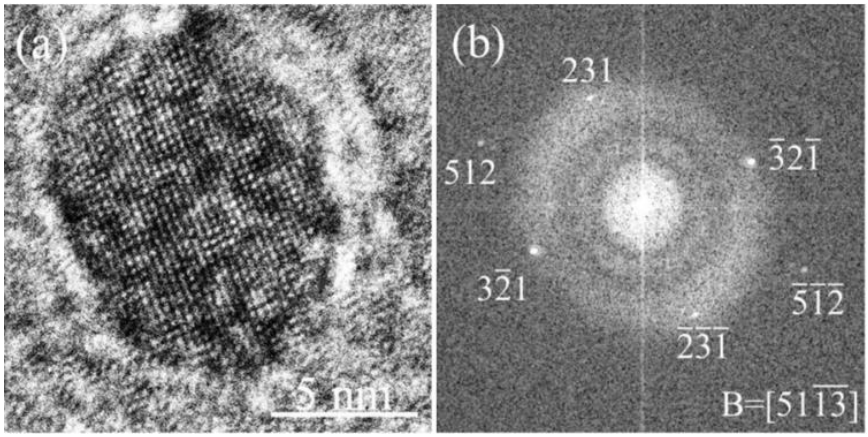

Fig. 2.1.2. (a) The HRTEM image of Y_2O_3 particle with cubic structure, and (b) FFT power spectrum with indexing [23].

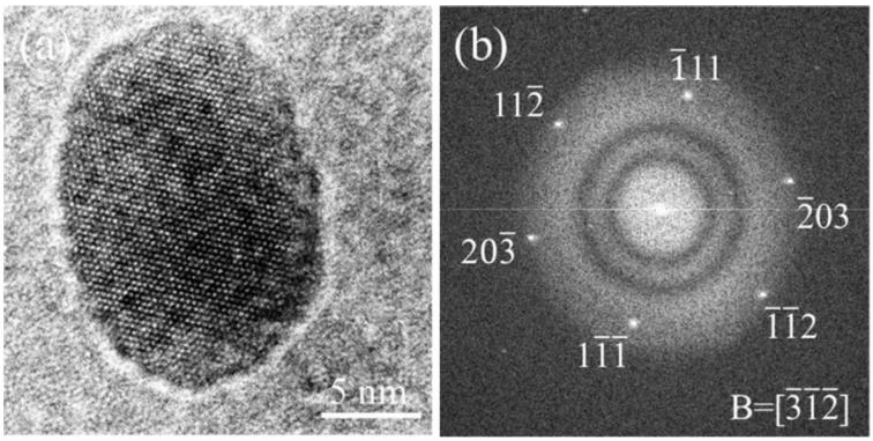

Fig. 2.1.3. (a) The HRTEM image of Y_2O_3 particle with monoclinic structure, and (b) FFT power spectrum with indexing [23].

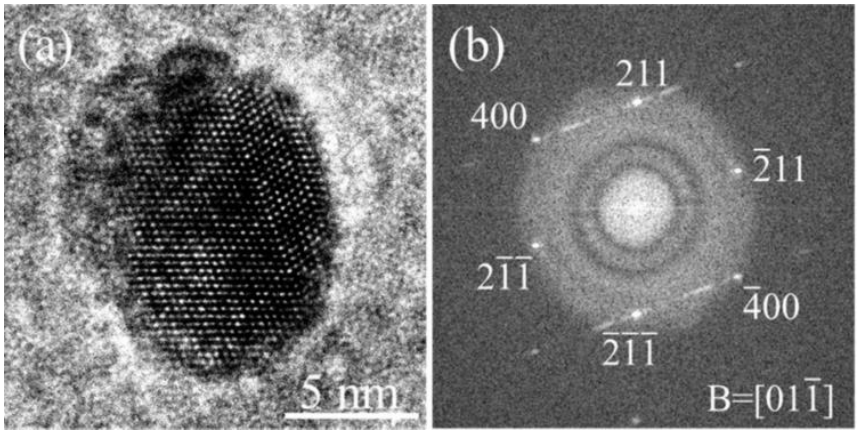

Fig. 2.1.4. (a) The HRTEM image of Y_2TiO_5 particle with orthorhombic structure, and (b) FFT power spectrum with indexing [23].

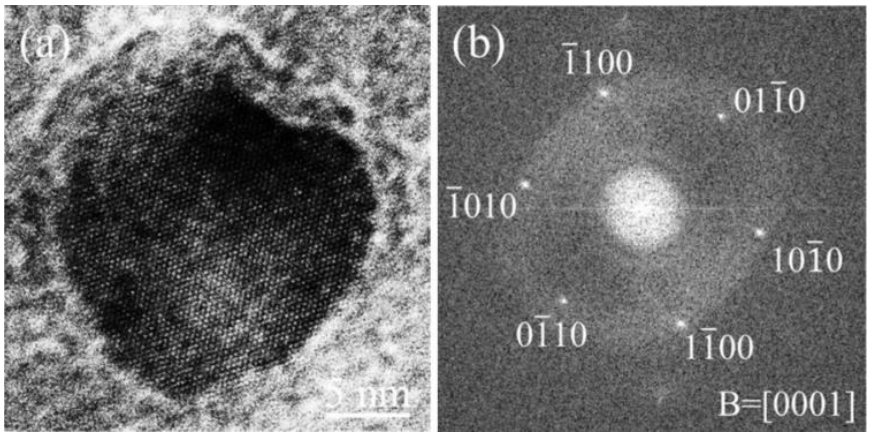

Fig. 2.1.5. (a) The HRTEM image of Y_2TiO_5 particle with hexagonal structure, and (b) FFT power spectrum with indexing [23].

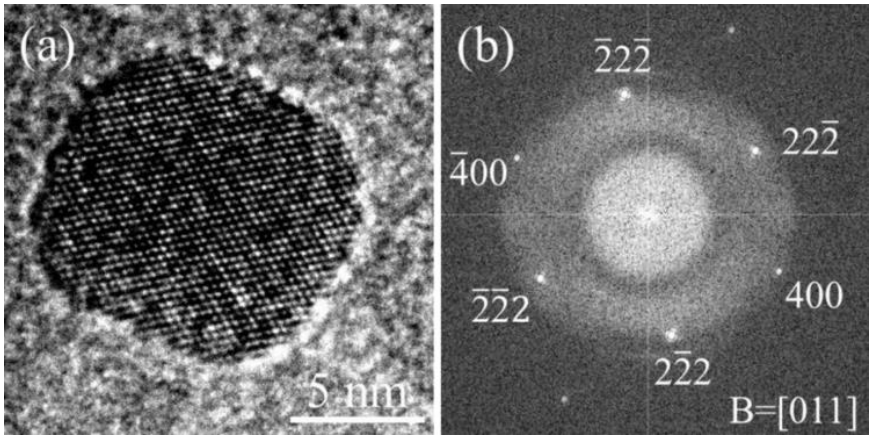

Fig. 2.1.6. (a) The HRTEM image of $Y_2Ti_2O_7$ particle with cubic structure, and (b) FFT power spectrum with indexing [23].

Through energy-dispersive X-ray spectrometry and confirmed that the nanoparticles can be grouped into two categories of 2 - 15 nm and 15 - 35 nm in diameter [24,25]. The smaller size group is known to be non-stoichiometric ($Y_2Ti_2O_7$) while the larger size group is stoichiometric (Y_2TiO_5).

As an alternative description, the $Y_2Ti_2O_7$ can be viewed as the $A_2^{3+}B_2^{4+}O_6O'$ pyrochlore structure which is made up of two interpenetrating covalent networks: $(A_2O')^{4+}$ and $(BO_3)^{4-}$, that are linked by the O^{2-} anions of the $(BO_3)^{4-}$ network mainly via ionic bonding [26]. In case of Cr-doped titanate the formula of $Y_2A_{2-x}B_xO_6O'$ exists, where A = Ti; B = Cr; x = 0, 0.02, 0.07, 0.25, 0.50, 0.75, 1.

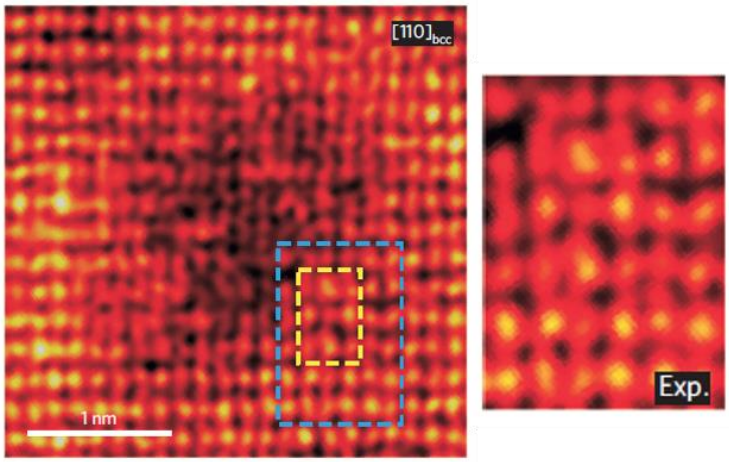

Fig. 2.1.7. HAADF-STEM characterization of Ti(Y,Fe,Cr)-O nanocluster [27].

In Fig.2.1.7, a nanocluster with dark contrast and distorted lattices can be clearly observed due to weaker interference from the surrounding bcc matrix. The size of the cluster is about 2–3 nm and at the central part of the cluster is much more defective whereas the cluster/matrix interface region shows excellent lattice coherence with a particular periodicity composed of brighter and darker atomic contrasts arising from the metal (brighter) and oxygen (darker) atomic columns of the nanocluster coherently overlapping the bcc lattice of the matrix [27]. Hirata et al. claimed that for an enrichment of Cr, the excellent lattice coherency at the interface may be associated with mediation of the lattice mismatch between the bcc Fe and oxide.

Prior to the irradiation experiment, the microstructure of ODS specimen was observed using JEM-2100 as in Fig.2.1.8. The high number density of dispersed nanoparticles and inhomogeneous dispersion state of nanoparticles is confirmed. From the 3mm disk specimen, certain area has homogeneous dispersion of nanoparticles with dense population, while other area has inhomogeneous state with varying particle number density. Also, post irradiation microstructure state was investigated using optical microscope in Fig. 2.1.9. The specimen was irradiated under 2 MeV with irradiation temperature of 723K. From the figure, due to characteristic of ODS steel for high particle number density, even after the high temperature irradiation experiment, many nanoparticles still survived and located heavily around the grain boundaries. Stable nanoparticles within the grains and at grain boundaries can provide resistance to steady-state creep at elevated temperatures which enhances the strength of the alloys.

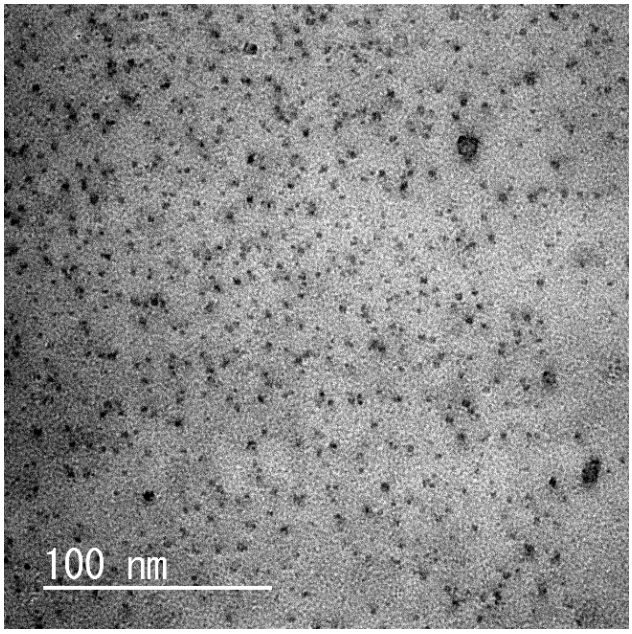

Fig. 2.1.8 Microstructure of 12Cr-ODS steel before the irradiation.

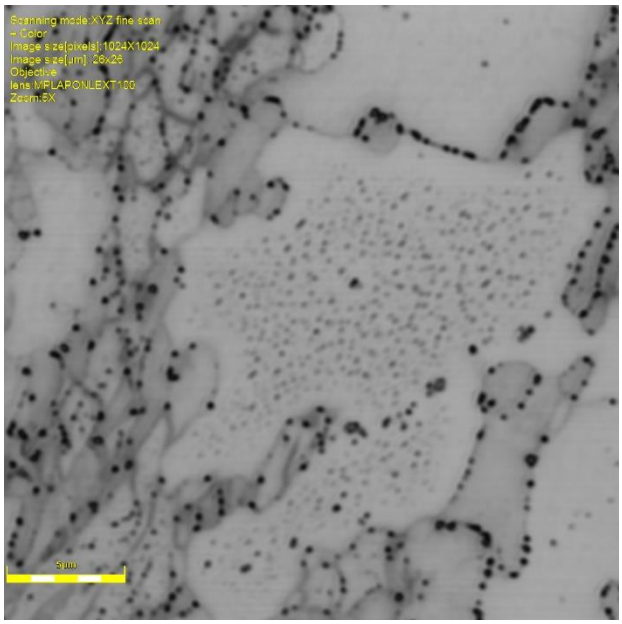

Fig. 2.1.9 Microstructure after the irradiation of 12Cr-ODS steel under 2 MeV at 723K using optical microscope (x5 magnified).

2.2 Mechanical Strength

ODS steels are targeted to be used as structural material under the harsh environment of high temperature and high radiation. In case of the structural material inside the fusion

reactor, it will have a contact with coolant which could be led to corrosion. Corrosion can deposit oxide layer which can further weaken the material. Also, ODS alloys will be subject to temperatures in the range of 500 – 700 ^{o}C and irradiation fluences on the order of several hundred displacements per atom.

Table 2.2.1 Summary of the alloy parameters and processing conditions [28].

Alloy designation	Metal particle size (μm)	Y_2O_3 content (wt%)	Y_2O_3 particle size (nm)	Milling time (h)
14WT-SM[a]	45–150	–	17–31	40
14YWT-SM[a]	45–150	0.3	17–31	40
14YWT-SM[a]	45–150	0.3	17–31	80
14YWT-CR[b]	<45	0.3	17–31	40

Table 2.2.2 Vicker hardnesses (VPN) of the 14WT and 14YWT alloys in the as-extruded condition and after 1 h at 1000 ^{o}C. Data from the 12 YWT in the as-processed condition and after 1 h at 1300 ^{o}C are included for comparison [28].

Condition	12YWT		14WT-SM 40 h mill		14YWT-SM 40 h mill		14YWT-SM 80 h mill		14YWT-CR 40 h mill	
	Hardness	SD	Hardness	SD	Hardness	SD	Hardness	SD	Hardness	SD
As-processed	411.2	16.1								
As-extruded			325.4	13.8	459	4.6	465.3	13.7	451.2	12
1000 °C/1 h			254.8	9.3	377	6.1	440.9	12.9	386	33.6
1300 °C/1 h	298.5	6.2								

2.3 Radiation Response

Previously, researchers have focused on investigating the radiation effects in ceramics such as defect production and migration in irradiated ceramics. Based on the studies, radiation induced diffusion processes such as subthreshold elastic collisions and ionization induced diffusion may produce low migration energies during irradiation [29]. Also, dramatic microstructural evolution occurs at a certain ratio of the electronic to nuclear stopping power. Researchers confirmed that the observed microstructural evolution appears to be sensitive to

the ionizing radiation dose rate. However, they also concluded that the ionizing radiation does not always have a strong influence on the microstructure of materials. Thus, radiation induced microstructural evolution in materials have several parameters to consider and is complex mechanism.

Table 2.3.1 The displacement threshold energy (E_d) for Y, Mg, and O and the maximum transferred energy (E_t) by 1 or 1.2 MeV electron [30].

	E_d	E_t 1 MeV	E_t 1.2 MeV
Y in Y_2O_3	57	49	64
O in Y_2O_3	57	271	357
Mg in MgO	55	178	235
O in MgO	55	271	357

Recently, it was found that the evolution of the oxide under irradiation could also depends on the chemical composition of the oxides. The dissolution rate of oxides, according to damage dose inside the oxide, is higher for oxides which are known to be less resistant to irradiation (MgO, Al_2O_3 by comparison to $MgAl_2O_4$), indicating that the dissolution rate of the oxides depends on the chemical composition [15]. This confirms that ballistic dissolution is not enough. Rather, the irradiation effect induced in the oxide plays a role in the oxide dissolution. Y rich precipitates, as in standard ODS alloys, appear to be the best choice for limiting the precipitates dissolution. This is due to the high energy threshold displacement of Y, leading to a lower dose in dpa in the oxide comparing to other oxides.

Table 2.3.1 Controversial radiation response results of ferritic ODS steels.

Ferritic ODS steel	Radiation type	Dose (dpa)	Temperature (°C)	Particle stability
12YWT [27]	Ion	0.7	300	Decrease
1DK [38]	Neutron	10.5 – 21	450 – 560	Increase
DY [39]	Neutron	81	400 – 580	Decrease
DY [40]	Neutron	75.4	400 – 480	Decrease
DY [41]	Ion	50	475	Stable
DY [27]	Ion	0.05	400	Stable
DY [27]	Ion	33	400	Decrease
DY [27]	Electron	33	300 – 550	Decrease
F94 [42]	Neutron	2.5 - 15	400 - 530	Stable

Table 2.3.2 Comparison between calculated and experimental decrease of diameter [15].

T (°C)	dpa (matrix)	EM10+	$\phi_{initial}$ (nm)	Estimate ϕ_{final} (nm)	Experimental ϕ_{final} (nm)	Loss (nm)
300	50	MgO	700	696	660	40
300	100	MgO	450	444	358	92
400	100	MgO	546	537	390	156
500	100	MgO	628	621	440	168
400	100	$MgAl_2O_4$	640	625	554	86
500	100	$MgAl_2O_4$	690	675	578	112
400	100	Al_2O_3		290	270	174

Neutron irradiation cause displacement cascade which has 4 stages: Ballistic, thermal spike, quench, and anneal. However, under high energy electron irradiation, only single or possibly double atom displacements of constituent elements can occur by the knock-on mechanism. In the crystalline phase, a vacancy and an interstitial are introduced under the irradiation. Typically, existence of an interstitial can be ignored in materials without irradiation. In case of electron irradiation, a threshold acceleration voltage for the single atom displacement by the electron knock-on effect exists. Under an irradiation with an acceleration voltage lower than a threshold acceleration voltage, no atomic displacement based on an elastic collision between an electron and constituent atom is introduced.

The disadvantage of neutron irradiation in investigating the particle dissolution mechanism is that it has the thermal spike associated with the primary knock-on. The primary knock-on causes damage other than the simple creation of vacancy-interstitial pairs. This other

damage can be disruptive if the purpose of the study is to understand the basic mechanism behind the particle instability.

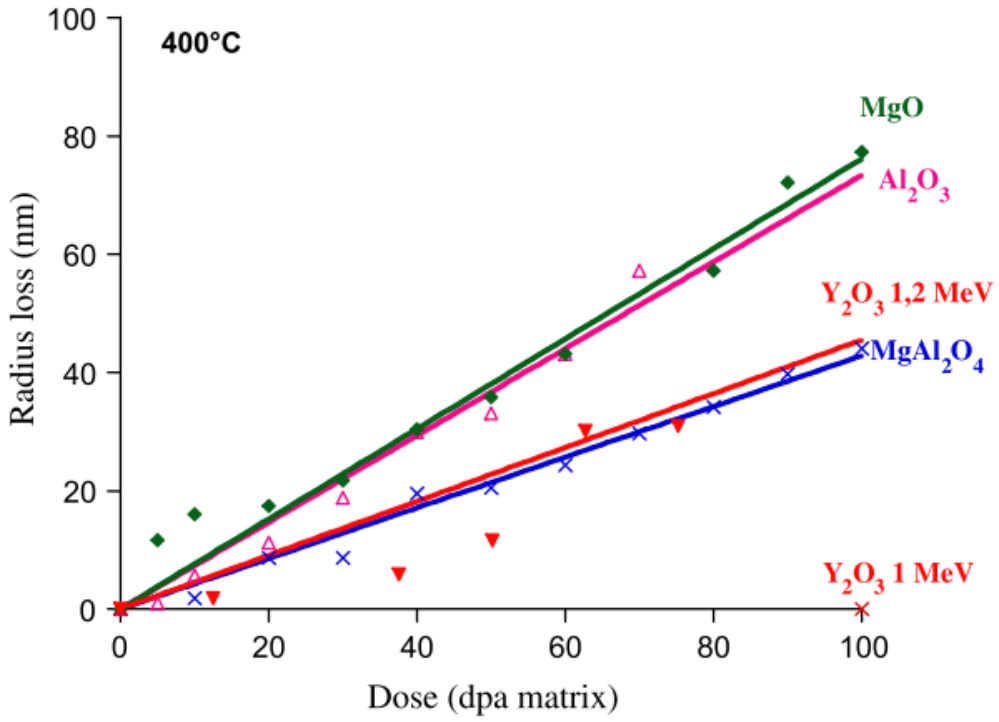

Fig. 2.3.1 Radius evolution of oxides during 1 MeV electron irradiation at 400 °C in a high voltage microscope according to the dose in the ferritic matrix [15].

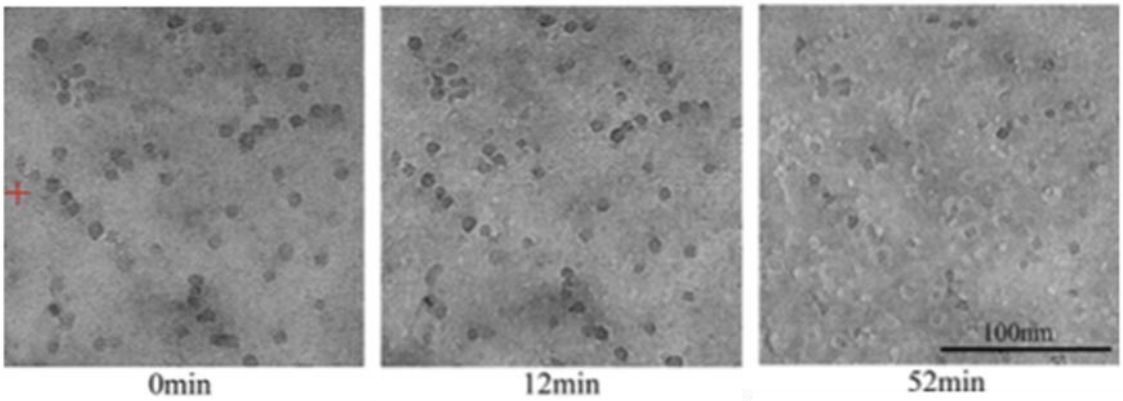

Fig. 2.3.2 Microstructure evolution under electron irradiation by in-situ HVEM at 400 °C [31].

Based on the previous researches, microstructural observations of the irradiated oxide indicate that the oxide evolution consists in four phenomena [15,30,32,33]:

1. The interfaces of the oxide particles with the matrix become irregular for the Ti rich nanoparticles.

2. The uniform distribution of the finest oxides (< 20 nm) disappears in high-dose irradiated specimens (> 60 dpa)

3. A halo of fine oxides appears around the larger ones and halo width increases with fluence.

4. The chemical composition of the oxides changes, even for specimens irradiated at low dose. The oxides lose more aluminum and titanium atoms than yttrium atoms.

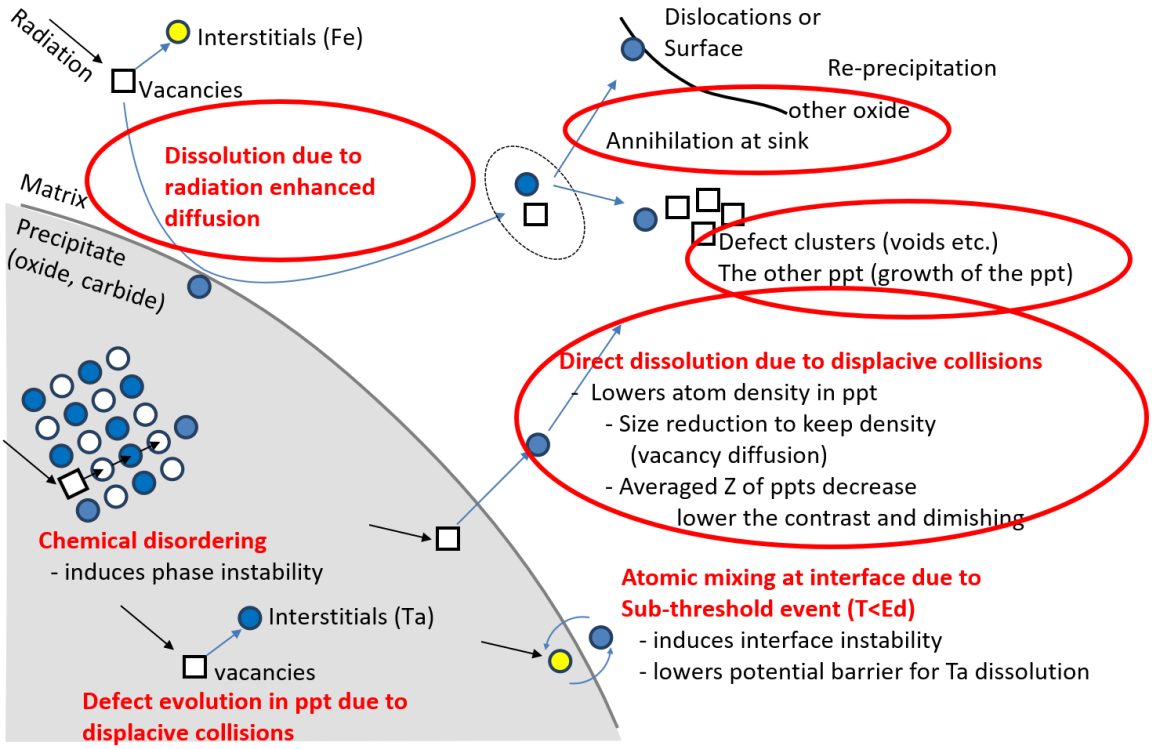

Fig. 2.3.3 Anticipated particle dissolution mechanisms under irradiation.

2.4 Research Purpose

A high number density of the dispersed Y-Ti-O nanoparticles, mainly $Y_2Ti_2O_7$ and Y_2TiO_5, embedded in the Fe-Cr matrix contributes to enhancement in high-temperature creep strength and irradiation resistance. To implement ODS steels in fusion reactors like DEMO,

the stability of Y-Ti-O under high-temperature irradiation is critical: Stable nanoparticles within the grains and at grain boundaries can provide resistance to steady-state creep at elevated temperatures which enhances the strength of the alloys.

According to previous literature, based on different radiation sources and the chemical composition of the irradiated materials, the radiation response of nanoparticles was different. To clarify the radiation response of NPs, three factors were controlled in this research: radiation energy, temperature, and electron beam condition. At different irradiation conditions, microstructural evolutions were closely investigated under in-situ Transmission Electron Microscope (TEM). In-situ TEM technique is selected as high voltage electron microscope can be used for the electron irradiation. From the previous research, the displacement threshold energy of Y in Y_2O_3 is reported as 57 eV and electron energy above 1.25 MeV can dissolve Y_2O_3 as its displacement threshold energy of Y is 64 eV. Thus, 1.25 MeV and 2 MeV electron irradiations were performed on the ODS steel to observe the effects of radiation damage on nanoparticles. In-situ HVEM technique allows to closely observe nanoparticles at high magnification (80,000 for H-3000 and 300,000 for JEM-ARM1300) as the average nanoparticle size is smaller than 5 nm. From utilizing the in-situ HVEM and -HRTEM, both size and shape evolutions of nanoparticles under irradiation were tracked time-sequentially.

CHAPTER 3.

Radiation Damage Phenomena in Solids

There is no perfect crystal and rather various types of crystal defects exist like point, line, surface, and volume defects. Point defects are vacancies, self-interstitials, interstitial or substitutional impurity atoms. Line defects are dislocation, and surface defects are grain boundaries. Finally, volume defects are voids, cavities, and precipitates.

Point defects are zero-dimensional and are associated with imperfections in a localized region. Vacancy is a vacant lattice site and can be predicted by the laws of thermodynamics. The vacancy formation energy is typically on the order of 1 eV. There are several methods of measuring vacancy concentration: electrical resistivity and the slope of the semilog plot of C_v versus 1/T.

$$C_v = exp\left(-\frac{E_v}{kT}\right) \tag{3.1.1}$$

Self-interstitial atom (SIA) is a type a point defect where a lattice atom occupies an interstitial site instead of its regular position. The equilibrium concentration of SIA is given by

$$C_i = \frac{n_i}{N_i} = exp\left(-\frac{E_i}{kT}\right) \tag{3.1.2}$$

where n_i is the number of interstitial atom and N_i is the number of interstitial sites.

Line defect or dislocation is critical as it is responsible for a plastic deformation of crystalline material. Dislocations are not equilibrium defects like point defects because the associated energy is higher than the increase in the enthalpy. The dislocation line perpendicular to the slip direction is called edge or Orowan-Taylor dislocation, and that parallel to the slip direction is called screw or Burgers dislocation. Dislocation density which is the number of dislocations in a given volume can be quantified and used to describe mechanical behavior of crystalline materials. Thus, dislocation density is primarily defined as “the total line length of dislocations per unit volume.”

Surface defects are two-dimensional defects known as planar defects. Grain boundaries or interphase boundaries (coherent, semicoherent, and incoherent) are the examples. Grain boundaries play an important role in strengthening in that finer grain sizes lead to higher strength known as Hall-Petch strengthening. They can lower the thermal/electrical conductivity of the material. Also, grain boundaries can be the preferred sites for corrosion and new phase precipitation sites.

Diffusion is the effective movement of atoms/molecules relative to their neighbors under the influence of a gradient. The diffusion process is assisted by the intrinsic thermal or kinetic energy of atoms. The driving force for a diffusion can be chemical potentials arising from the concentration gradient or gradients in electrical field or mechanical stresses. The movement of atoms could be over a large number of interatomic distances (long-range diffusion) or over one or two interatomic distances (short-range diffusion). In terms of the different chemical compositions of the nanoparticles and the matrix, the growth of the nanoparticle requires long-range diffusion of solute atoms to the precipitate-matrix interface and to the transfer of solute atoms across the interface.

For the different phases of nanoparticle and matrix, the growth of nanoparticle can only occur if diffusion can transport the solute atoms toward the interface. If the solute atoms can readily transfer across the interface, then the growth rate of the nanoparticle will be governed by the diffusion rate of solute atoms. This process is called diffusion-controlled growth.

However, if the solute atoms cannot readily cross the interface, the growth rate will then be governed by the interface kinetics which is called interface-controlled growth.
When the diffusion process and interface reaction occur at similar rates, then the migration of the interface will be mixed controlled.

The growth of spherical nanoparticles can be described as

$$R = \chi\sqrt{Dt} \qquad (3.1.3)$$

where the nanoparticle radius R after time t is governed by the χ of the solute supersaturation function and the diffusivity of solute atoms D.

For volume diffusion-controlled coarsening, the coarsening of spherical nanoparticles can be approximated as

$$r^3 - r_o^3 \propto D_v \gamma_i C_e t \quad (3.1.4)$$

where the average radius of spherical nanoparticles at time t and 0 as r and r_o, and the volume diffusion coefficient of the solute element as D_v, and the specific interfacial energy between nanoparticle and matrix phases as γ_i, and C_e as the equilibrium solid solubility of solute in the matrix phase in weight percentage.

Based on this volume diffusion-controlled coarsening equation, the equilibrium solid solubility and solid-sate diffusivity of the solute element, and the interfacial energy between the nanoparticle and the matrix phase controls the coarsening of nanoparticles.

To achieve low coarsening rates of nanoparticles at elevated temperatures, alloying elements should have low equilibrium solid solubility and low solid-state diffusivity in the matrix phase and the dispersed nanoparticles should preferably be coherent with the matrix. Also, the dispersed nanoparticles for strengthening mechanism should be intrinsically stable at elevated temperatures.

A low interfacial energy between precipitate phases and the matrix phase is critical for achieving low coarsening rates and for homogeneous solid-state precipitation of the nanoparticles.

At elevated temperatures ($T > 0.5T_m$), in terms of deformation, dislocation gliding is not the dominant mechanism. Typically, based on the applied stress and the temperature, the plastic deformation of alloys occurs primarily by mechanisms of dislocation climb, grain boundary sliding or vacancy diffusion. However, for a large volume fraction of thermally stable

nanoparticles within the grains and at grain boundaries, it can provide resistance to steady-state creep at elevated temperatures which enhances the strength of the alloys.

3.1 Neutron Damage Phenomena

There are various types of radiation defects induced by intense nuclear radiation of high energy neutrons ($E \geq 0.1$ MeV):

- Vacancies.
- Interstitials.
- Impurity atoms produced by transmutation.
- Thermal spikes which are regions with atoms in high-energy states.
- Displacement spikes which are regions with displaced atoms, vacancies, self-interstitials (Frenkel pairs) produced by primary and secondary knock-on atoms.
- Depleted zones which are regions with vacancy clusters.
- Voids.
- Bubbles which are voids stabilized by filled gases such as He.
- Replacement collisions which are scattered interstitial atoms falling into vacant sites after collisions between moving interstitial and stationary atoms and dissipating their energies through lattice vibrations.

Under the neutron irradiation, anticipated phenomena are displacement cascade and point defect. Defects can build up and move. They can be diffused or transferred ballistically by more radiation damages. For the displacement cascade, the final state of the cascade is extremely important as the end of the cascade is the starting point for defect diffusion, agglomeration, and destruction. Vacancies can transform into voids, and void can cause

swelling. Also, radiation damage leads to embrittlement which is amorphization. These yield the observable effects of irradiation in solids.

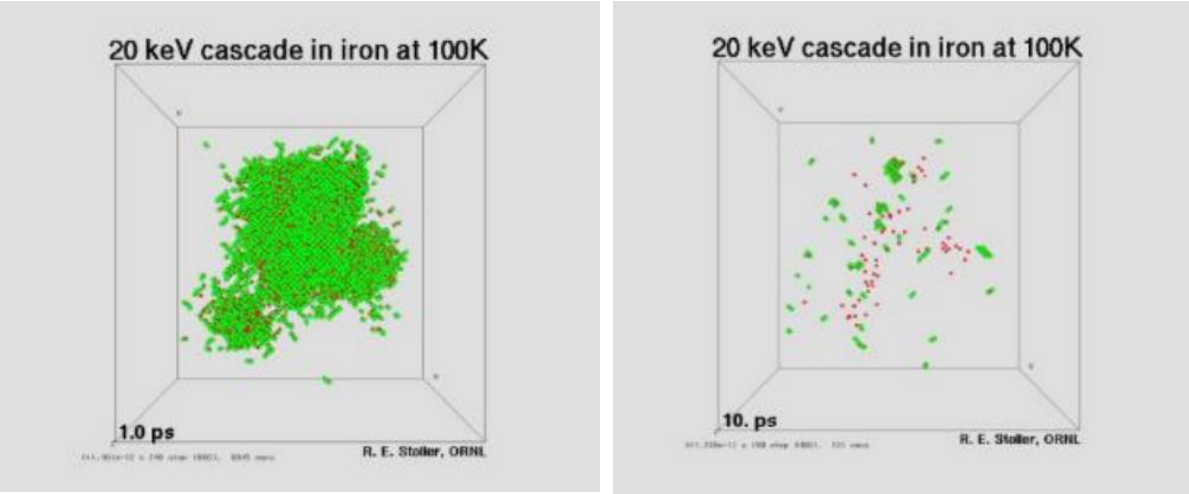

Fig. 3.1.1 Typical point defect configuration from a 20 keV MD cascade simulation in Fe at 100K. The peak damage state occurs at 1 ps (left) and the final damage state occurs at 10 ps (right) [34].

In displacement cascade, there are four stages: Collisional, thermal spike, quenching, and annealing [35]:

1. Collisional

It occurs before 1 ps and the primary recoil atom initiates a displacement cascade. In this stage, there is no formation of stable lattice defects.

2. Thermal spike

The collisional energy of the displaced atoms is shared among neighbouring atoms in the high deposited energy density region. The spike can occur in several zones and the atoms resemble molten material.

3. Quenching

It occurs around 10 ps and the system reaches thermodynamic equilibrium. Energy is transferred to the surrounding atoms and the molten zones return to the condensed form. Stable lattice defects form as point defects or defect clusters.

4. Annealing

Further rearrangement and interaction of defects by thermally activated diffusion of mobile lattice defects. This stage can last till all mobile defects escape the cascade region.

A point defect formation under neutron irradiation is a creation of Frenkel pairs. When the Frenkel pairs are created there are number of effects on material:

1. Increase of dislocation density which leads to embrittlement.
2. Formation of voids that leads to swelling.
3. Increase on diffusivity which leads to local segregation.
4. Amorphization or crystallization that results in unexpected phase changes.

Neutron irradiation cause displacement cascade which has 4 stages: Ballistic, thermal spike, quench, and anneal. However, under high energy electron irradiation, only single or possibly double atom displacements of constituent elements can occur by the knock-on mechanism. In the crystalline phase, a vacancy and an interstitial are introduced under the irradiation. Typically, existence of an interstitial can be ignored in materials without irradiation. In case of electron irradiation, a threshold acceleration voltage for the single atom displacement by the electron knock-on effect exists. Under an irradiation with an acceleration voltage lower than a threshold acceleration voltage, no atomic displacement based on an elastic collision between an electron and constituent atom is introduced.

The disadvantage of neutron irradiation in investigating the particle dissolution mechanism is that it has the thermal spike associated with the primary knock-on. The primary knock-on causes damage other than the simple creation of vacancy-interstitial pairs. This other damage can be disruptive if the purpose of the study is to understand the basic mechanism behind the particle instability.

3.2 Theory of Electron-Atom Interaction

An incident electron loses energy during its passage through matter by collisions with target electrons, collisions with target atoms, and through radiation. The most important contributions are the ionization losses due to inelastic collisions with electrons. Multiple scattering can happen due to small-angle elastic collisions with the target nuclei, and this tends to increase the path length of the electron in the substance. This also implies that electron's path gets wider like a cone shape which deviates from the originally unidirectional beam. The angular dispersion of electrons depends on the electron energy and the sample thickness along with other factors. The angular distribution of the electrons can be represented by a Gaussian distribution.

The scattering of the electron beam through the material can form different angular distribution and it can be either forward scattering or back scattering interaction. If an electron is scattered below 90 degree, then it is forward scattered; otherwise, it is backscattered. If the specimen is thicker, fewer electrons are forward scattered and more are backscattered. Incoherent, backscattered electrons are the only small parts of the incident beam for bulk (non-transparent specimens). The reason that electrons can be scattered through different angles is related to the fact that an electron can be scattered more than once. Generally, the more scattering occurs, the greater the angle of scattering. In fact, forward scattering includes the

direct beam, most elastic scattering, refraction, diffraction (mostly Bragg diffraction), and inelastic scattering.

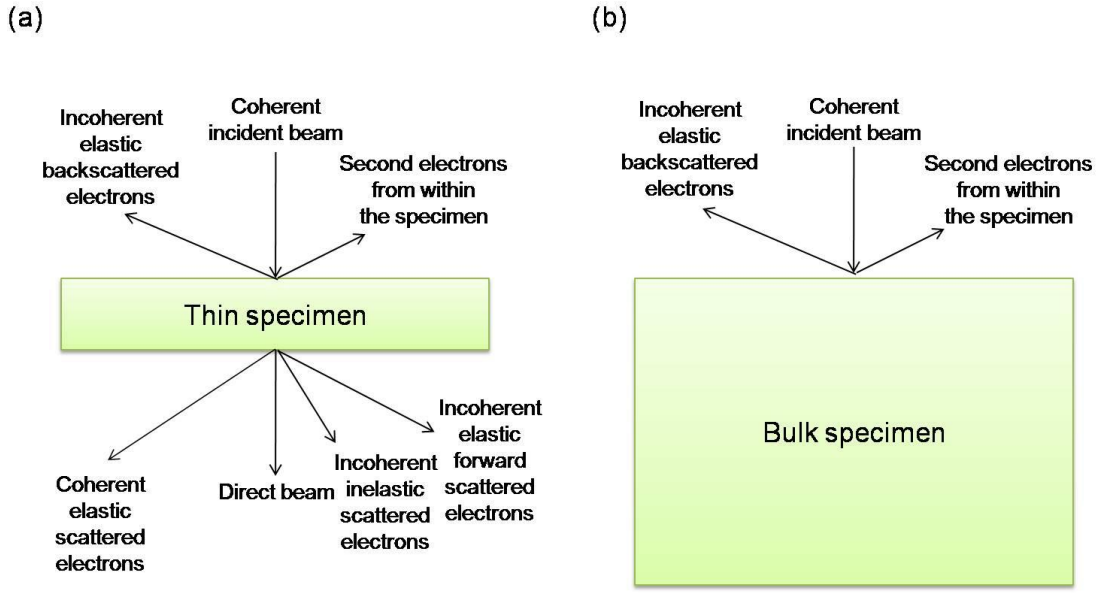

Fig. 3.2.1 Different types of electron scattering in (a) a thin specimen and (b) a bulk specimen [36].

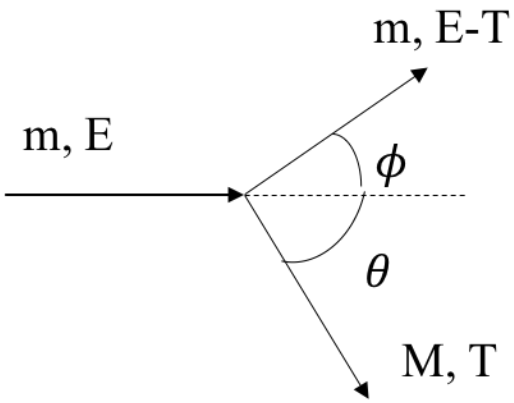

Fig. 3.2.2 The scattering of an energetic electron by an atom.

The elastic scattering process can eventually lead into atomic displacement. In the classical mechanics of the conservation laws of energy and momentum, the electron scattering angle (ϕ) and the atomic recoil angle (θ) can be related to the energy transferred to strike an atom and its scattering angle as shown in equations 3.2.1 and 3.2.2.

$$\theta = \frac{\pi}{2} - \frac{\phi}{2} \quad (3.2.1)$$

$$T = T_m sin^2\left(\frac{\phi}{2}\right) = T_m cos^2\theta \quad (3.2.2)$$

$$T = \frac{4mM}{(m+M)^2} E \quad (3.2.3)$$

The maximum transmitted energy (T_m) occurs in a head-on collision. In the case of electrons with $m \ll M$ and $E \ll Mc^2$, the maximum transmitted energy becomes

$$T_m = \frac{560.8}{A}\epsilon(\epsilon + 2) \text{ in eV} \quad (3.2.4)$$

where A represents the atomic mass and $\epsilon = E/mc^2$.

The displacement cross section is needed to calculate the number of recoil atoms displaced after having received the energy T. When the knock-on atom receives an energy T which exceeds twice of the threshold energy for displacement ($T > 2T_d$), more than one displaced atom can occur due to one electron-atom collision events. The number of displaced atoms as a function of transmitted energy can be calculated by Kinchin and Pease model which is described in detail in chapter 3.2.2.

3.2.1 High Energy Electron Irradiation

Electron irradiation only produce point defects without cascade effects. Thus it can offer much clear image of the point defects mechanism on the change of target material property. Through combination with the modern transmission electron microscope, in-situ image of the irradiation process could be shown by the experiment. Also, through utilizing the in-situ TEM, one can observe the microstructure evolution at fixed geometry of specimen throughout the whole irradiation period. For this to be accomplished, the TEM specimen must be thin below 200 nm. In this case, the surface effect as a point defect sink is hardly negligible.

Electrons experience large numbers of interactions and in general gradually lose energy until they are stopped. This is expressed in terms of electron range and material stopping powers.

3.2.2 Electron dose effect

The displacement per atom (dpa) amount in a matrix irradiated by electron can be calculated by McKinley-Feshbach approximation and Kinchin-Pease model. McKinley-Feshbach approximation gives differential scattering cross-section, and Kinchin-Pease model allows to approximate damage function.

McKinley-Feshbach approximation is defined as:

$$d\sigma_{M-F} = \frac{4\pi\alpha^2 Z_2^2 E_R^2}{m_e^2 c^4}\frac{1-\beta^2}{\beta^4}\left[1-\beta^2\frac{T}{T_M}+\pi\alpha\beta\left(\sqrt{\frac{T}{T_M}}-\frac{T}{T_M}\right)\right]\frac{T_M}{T^2}dT$$

$$\sigma_{tot}(E_1, E_d) = \int_{E_d}^{T_M} \upsilon(T)\frac{\mathrm{d}\sigma_{M-F}}{\mathrm{d}T}\mathrm{d}T$$

Kinchin-Pease model is defined as:

$$\upsilon(T) = \begin{cases} 0 & for\ T < E_d \\ 1 & for\ E_d < T < 2E_d \\ \dfrac{T}{2E_d} & for\ 2E_d < T < E_c \\ \dfrac{E_c}{2E_d} & for\ T \geq E_c \end{cases}$$

Based on the above equations, dose rate can be calculated as follows:

$$\frac{dpa}{s} = \frac{\varphi \times \sigma_d \times \upsilon(T)}{N_A}$$

3.3 Microstructural Evolution of Nanoparticles under Irradiation

Microstructural evolution of nanoparticles under irradiation is critical as any changes can be linked with change in mechanical properties and material performance under high irradiation environment. Thus, the study of mechanism for microstructure evolution of irradiated nanoparticles is important. So far, many studies have been done on growth of nanoparticles while the particle number density decreases.

In terms of the different chemical compositions of the nanoparticles and the matrix, the growth of the nanoparticle requires long-range diffusion of solute atoms to the precipitate-matrix interface and to the transfer of solute atoms across the interface.

Diffusion-controlled growth

For the different phases of nanoparticle and matrix, the growth of nanoparticle can only occur if diffusion can transport the solute atoms toward the interface. If the solute atoms can readily transfer across the interface, then the growth rate of the nanoparticle will be governed by the diffusion rate of solute atoms. This process is called diffusion-controlled growth.

Interface-controlled growth

However, if the solute atoms cannot readily cross the interface, the growth rate will then be governed by the interface kinetics which is called interface-controlled growth.

When the diffusion process and interface reaction occur at similar rates, then the migration of the interface will be mixed controlled. The growth of spherical nanoparticles can be described as Eq. (3.1.3).

Volume diffusion-controlled coarsening

For volume diffusion-controlled coarsening, the coarsening of spherical nanoparticles can be approximated as Eq. (3.1.4). Based on this volume diffusion-controlled coarsening equation, the equilibrium solid solubility and solid-sate diffusivity of the solute element, and

the interfacial energy between the nanoparticle and the matrix phase controls the coarsening of nanoparticles.

To achieve low coarsening rates of nanoparticles at elevated temperatures, alloying elements should have low equilibrium solid solubility and low solid-state diffusivity in the matrix phase and the dispersed nanoparticles should preferably be coherent with the matrix. Also, the dispersed nanoparticles for strengthening mechanism should be intrinsically stable at elevated temperatures.

A low interfacial energy between precipitate phases and the matrix phase is critical for achieving low coarsening rates and for homogeneous solid-state precipitation of the nanoparticles.

At elevated temperatures ($T > 0.5T_m$), in terms of deformation, dislocation gliding is not the dominant mechanism. Typically, based on the applied stress and the temperature, the plastic deformation of alloys occurs primarily by mechanisms of dislocation climb, grain boundary sliding or vacancy diffusion. However, for a large volume fraction of thermally stable nanoparticles within the grains and at grain boundaries, it can provide resistance to steady-state creep at elevated temperatures which enhances the strength of the alloys.

3.3.1 Controversial Results on Nanoparticles Stability

The stability of Y-Ti-O nanoparticles dispersed in Fe-Cr matrix came under the spotlight due to inconsistent results regarding the nanoparticles' response to radiation [9,31,37]. Several researchers have reported that nanoparticles are either shrinking or disappearing due to radiation exposure that could degrade the enhanced mechanical property of the steel [14,31]. Among the studies of high temperature (573-773K) irradiation on ferritic ODS steels, Y-Ti-O nanoparticles have been observed to be stable under neutron and proton irradiation on 9Cr-

ODS steel [33,38], while the size of Y-Ti-O or Y-Ti-Cr-O nanoparticles in 18Cr-ODS steel has been increased under Fe+ ion irradiation [39]. On the other hand, a size decrease in Y-Ti-O nanoparticles has been reported under electron irradiation [30,31]. These inconsistent results indicate the inconclusive radiation response of Y-Ti-O nanoparticles and that further research should be carried out to identify the mechanism behind this complex phenomenon.

Several studies have focused on the irradiation response of the nanoparticles at high dose with long irradiation time, but there is a lack of literature regarding the initial short-time radiation effect with a low dose on the nanoparticles [40]. The main objective of this study is, therefore, to investigate the microstructural evolution of Y-Ti-O nanoparticles in ferritic 12Cr-ODS steel under in-situ electron radiation. Under electron irradiation, instability mechanisms for carbide type nanoparticle dissolution in F82H is reported and the carbide instability was investigated under in-situ electron radiation [41,42]. It has concluded that due to various irradiation conditions, the flow rate of vacancy-type defects could dissolve constituent atoms of carbides into matrix [42]. In this study, the focused electron beam technique was employed to investigate the stability of the nanoparticles in the matrix as it could be affected by the radiation effects on the nanoparticles and the interaction of radiation-induced defects in a matrix with nanoparticles [43]. Also, the focused beam technique has a steep vacancy concentration distribution, and this enhances vacancy diffusion compare with a defocused beam. From the previous research, the displacement threshold energy of Y in Y_2O_3 is reported as 57 eV and electron energy above 1.25 MeV can dissolve Y_2O_3 as its displacement threshold energy of Y is 64 eV. In order to investigate the radiation response of nanoparticles, a 2 MeV high voltage electron microscope (HVEM) was used for the direct in-situ observation of microstructure evolution. In the case of electron irradiation, energy higher than 1 MeV is known to cause atomic displacements in iron [44]. Also, through comparison of the focused and the defocused beam effects on nanoparticles, damage mechanisms are studied.

Table 3.3.1 Summary of previous studies of oxide nanoparticle evolution from the literature [40].

Material	Type	Irrad. Particle	Irrad. Temp. (°C)	Irrad. Dose (dpa)	Dose Rate (dpa/s)	Method	Structure	Chemistry	Size	Number Density	Ref
F94	F	Fast n	400–530	2.5–15		TEM	n.s.	n.s.	Stable	Stable	[24]
MA957	F	Fast n	325	6		TEM, SANS	n.s.	n.s.	Stable	n.s.	[66]
9Cr ODS	M	Ni^{+}	500–700	5, 50, 150	1.4×10^{-3}	HR-TEM	n.s.	n.s.	Decrease	Increase	[7], [67]
MA957	F	$He^{+} + Ni^{+}$	450, 650	150	2×10^{-3}	TEM	n.s.	n.s.	Stable	Stable	[68]
MA957	F	Fast n	412–670	109–113		APT	n.s.	Stable	Stable	Stable	[69]
9Cr ODS	F	H^{+}	525	1	5×10^{-6}	APT, EFTEM	n.s.	Stable	Decrease	Decrease	[70]
14YWT	F	H^{+}	400	1, 3	5×10^{-6}	EFTEM	n.s.	n.s.	Increase	Increase	[11]
14YWT	F	Ni^{2+}	~75–600	5, 50, 100	2×10^{-3}	APT	n.s.	n.s.	Decrease at $T_{irr} < 600$ °C; else stable	Stable	[11]
14YWT	F	Ni^{2+}	~75–600	5, 50, 100	2×10^{-3}	EFTEM	n.s.	n.s.	Increase	Decrease for $T_{irr} \leq 300$ °C; else increase	[11]
14YWT	F	Fast n	500	3	1×10^{-7}	APT, EFTEM	n.s.	n.s.	Decrease	Increase	[11]
12Cr ODS	F/M	Fe^{2+}	325–625	100, 200	n.s.	HRTEM	Larger phases lose coherency	n.s.	Decrease	Decrease	[8]
12Cr ODS	F/M	$Fe^{8+} + He^{+} + H^{+}$	21	4.4		EFTEM	n.s.	Stable	Stable	Stable	[71]
9Cr ODS	F	Fe^{2+}	400	50	1×10^{-4}	APT	n.s.	n.s.	Stable	Decrease	[72]
DY	F	Fast n	400–580	81		TEM	Halo; irregular O/M interfaces	Ti, Al loss	Decrease	Decrease	[16]
14YT	F	Fe^{3+}	700	50		APT	n.s.	Y:Ti decrease	Increase	Increase	[25]
14YWT	F	Ni^{2+}	300–600	100	1.39×10^{-2}	APT	n.s.	Y:Ti increase at 300 °C	Decrease	Decrease	[18]
9Cr ODS	F	H^{+}	400	3.7	0.5×10^{-5}	APT	n.s.	Y:Ti increase	Increase	Decrease	[19]
MA957	F	$He^{+} + Ni^{+}, C^{-}$	475–625	200	$3.0–14 \times 10^{-3}$	TEM	n.s.	n.s.	Stable	Stable	[73]
9Cr, 12Cr ODS	M, F	Fast n	420–835	28–51		TEM	n.s.	n.s.	Stable	Stable	[74]
MA957	F	Fe^{+}	25	18		TEM	Amorphize	n.s.	Stable	n.s.	[42]
MA957	F	Kr^{+}	500	200		TEM	Stable	n.s.	Stable	n.s.	[42]
K6	F	n.s. ion	300–700	20	9.9×10^{-5}	HRTEM	n.s.	n.s.	Stable	Stable	[75]
K1, K4	F	Fe^{3+}	500–700	20, 150	1×10^{-3}	STEM	n.s.	n.s.	Stable	Stable	[76]
SOC-1	F	Fe^{3+}	650	60	5×10^{-4}	STEM	n.s.	Stable	Stable	Stable	[77]
18Cr ODS	F	Fe^{+}	500	4–45		EFTEM	Interfaces become irregular		Stable	Stable	[39]
18Cr ODS	F	Fe^{+}	500	150		APT, EFTEM	n.s.	Approaches $Y_2Ti_2O_7$ stoich.	Increase	Decrease	[9]
18Cr ODS	F	Au^{2+}	RT	156		APT, EFTEM	Amorphization	n.s.	Dissolution	Dissolution	[9]
9Cr-2W ODS	M	e^{-}	400			TEM	Amorphization	n.s.	Decrease	Decrease	[44]
DY	F	$Cr^{6+} + He^{+}$	475	50	3.0×10^{-4}	TEM	Complex oxides not observed	n.s.	Stable	n.s.	[78]
F82H, 16Cr ODS	F	Fe^{3+}	380	20	1.1×10^{-3}	HRTEM	n.s.	n.s.	Decrease	Decrease	[79]
14Cr ODS	F	Fe^{3+}	Cryo - 700	15	3×10^{-3}	GIXRD	Stable	n.s.	Dissolution at cryo; else decrease or stable	Dissolution at cryo; else decrease or stable	[13]
MA957	F	Therm. n	325	2.0, 5.5	2.9×10^{-7}	TEM, SANS	Stable	n.s.	Stable	Stable	[80]
DY	F	Fast n	400–480	75.4		XAFS, TEM	Disordering	n.s.	Decrease (larger oxides)	Not Specified	[35]
MA957	F	Fast n	600	3	3.7×10^{-7}	APT	n.s.	Y:Ti decrease	Stable	Stable	[26]
DY	F	Kr^{18+}	RT			STEM	Amorphize		Stable	Stable	[45]
EM10 ODS	F	e^{-}	300–500	100	$3–6 \times 10^{-3}$	HRTEM	n.s.	Stable	Decrease	n.s.	[17]
DY, EM10 ODS	F	He^{+}	400	0.05		HRTEM	n.s.	Stable	Stable	Stable	[20]
DY, EM10 ODS	F	Ar^{+}	400	33		HRTEM	Amorphize	n.s.	Decrease	Decrease	[20]
DY	F	Fast n	400–580	≤81		HRTEM	Halo		Decrease > 70 dpa		[20]

Table 3.3.2 Radiation response in fully ferrite ODS steels under various conditions.

Ferritic ODS steel	Radiation type	Dose (dpa)	Temperature (°C)	Particle stability
12YWT [27]	Ion	0.7	300	Decrease
1DK [38]	Neutron	10.5 – 21	450 – 560	Increase
DY [39]	Neutron	81	400 – 580	Decrease
DY [40]	Neutron	75.4	400 – 480	Decrease
DY [41]	Ion	50	475	Stable
DY [27]	Ion	0.05	400	Stable
DY [27]	Ion	33	400	Decrease
DY [27]	Electron	33	300 – 550	Decrease
F94 [42]	Neutron	2.5 - 15	400 - 530	Stable

CHAPTER 4.

Experiment

4.1 Fabrication Method of 12Cr-ODS Steel

ODS steels are developed to further improve the mechanical properties under high temperature and neutron irradiation environment, and this enhancement in properties is through altering microstructure. A fabrication of ODS steels is done through mechanical alloying and power metallurgical technique. Mechanical alloying process is when mixtures of powders undergo severe deformation until atomic solutions are formed. Following mechanical allying, through powder metallurgical technique, the particles are consolidated. From this fabrication technique, uniform sub- micrometer grain structures, high-density dislocations and a dispersion of fine particles are achieved. As the manufacturing processes are critical for the final microstructure of ODS steels which leads to the mechanical properties, the detailed description of the 12Cr-ODS steel fabrication is shown in Fig. 4.1.1. The ferritic 12Cr-ODS steel with a composition of 12Cr-2W-0.3Ti-0.25Y_2O_3 (wt%) was produced in Institute for Materials Research (IMR) under a framework of Japan Science and Technology project after the nuclear accident in 2011 [11].

The detail of its chemical composition is listed in Table 4.1. In this study, from the as-fabricated 12Cr-ODS steel, it has undergone cold rolling 60% for thickness reduction, thermal annealing at 1200 ^oC for 1 hour, and finally recrystallized by 80%. The ODS steel has an average nanoparticle diameter of 3.5 ± 0.7 nm and number density of $1.3\times10^{23}\,m^3$ [45]. Through high-angle angular dark- field (HAADF) and energy dispersive spectroscopy (EDS) mapping, the chemical composition of nanoparticles was analyzed and were identified as either Y_2O_3 or Y-Ti-O complex [23]. Furthermore, through high-resolution transmission electron microscope

(HRTEM), Y-Ti-O nanoparticles were identified to be orthorhombic- and hexagonal-Y_2TiO_5, and cubic-$Y_2Ti_2O_7$ [23].

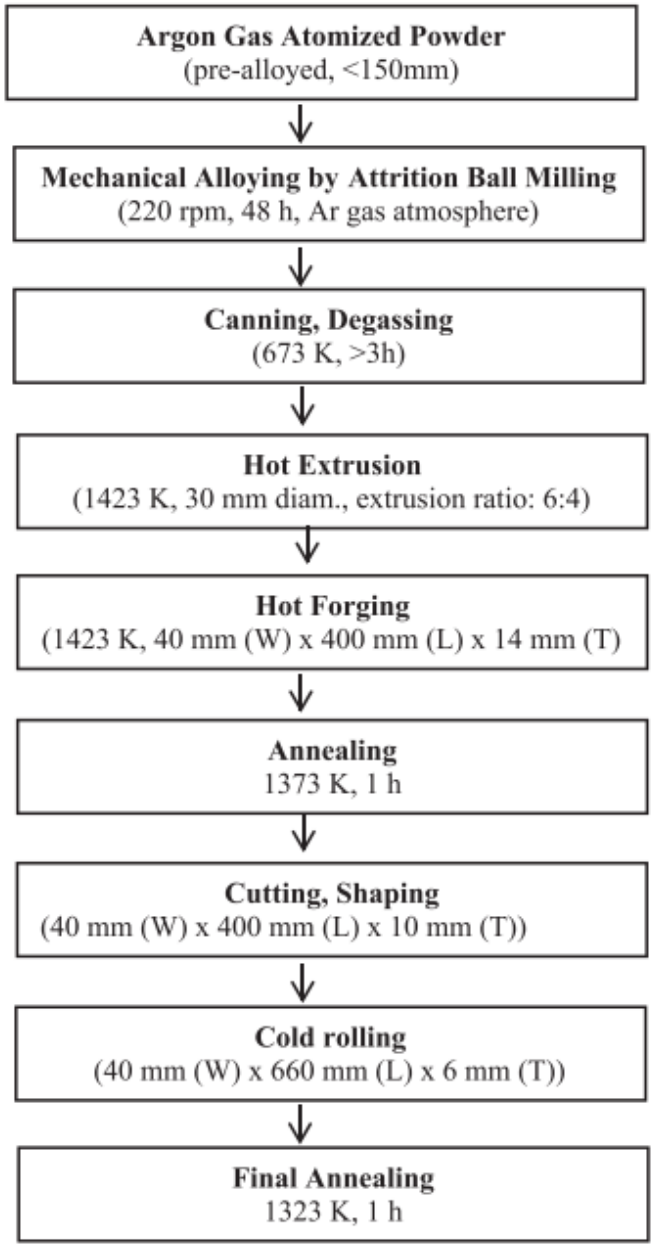

Fig. 4.1.1. Manufacturing processes for the 12Cr-ODS steel [11].

Table 4.1 Chemical composition of the 12Cr-ODS ferritic steel (wt%)

Cr	W	Ti	Y	O	C	N	Fe
12.01	1.91	0.31	0.2	0.117	0.033	0.008	Bal.

4.2 TEM Specimen Preparation

From the bulk specimen, 3 mm diameter discs were prepared by cutting then mechanical grinding with gradually increasing grit number from 600 to 2000 grit on both surfaces until thickness below 100 μm was obtained. Afterward, electrochemical polishing was performed at room temperature in a 5% perchloric acid in acetic acid solution to achieve electron transparency. The TEM specimen was prepared for two different irradiation conditions: the focused beam of the Gaussian flux profile and the defocused beam of uniform flux profile. Prior to high-temperature irradiation, the specimen surface was observed in TEM and confirmed that the fabricated 12Cr-ODS steel has a heterogeneous distribution of nanoparticles.

The specimen thickness measurement was done using thickness fringe method. Through this method, the local thickness of a TEM foil was acquired. For this method, diffraction pattern was taken at s=0 condition (two-beam condition). At s=0 condition, the distance between the two neighbored fringes is the greatest.

For this measurement, JEM-2100 with operating voltage of 200 kV was used. From the diffraction pattern analysis of the TEM image, z=[110] is found. Based on electron wavelength data and extinction distance, a thickness fringe can be calculated.

$$\xi_{200\ kV} = 1.267\xi_{100\ kV}$$

$\xi_{100\ kV}$ = 27 nm

$\xi_{200\ kV}$ = 1.267 × 27 nm = 34.209 nm

For a single thickness fringe condition, $t_1=(1+1/2)\,\xi_{200\ kV}$ = 51.3 nm

After the acquisition of specimen thickness, it can be computed with number of particles in the TEM image to calculate a particle number density.

For the in-situ HVEM experiment, a thin foil is prepared with thickness less than 60 nm. In a thin foil case, the concentration of interstitials rapidly reaches a steady state as the production rate is matched by the escape rate to the surface [78]. The loss of interstitials to sinks and interstitial loops can occur. Also, in the case of high vacancy mobility at high temperature, the vacancy-interstitial mutual annihilation reaction due to the motion of vacancies becomes effective when the vacancies accumulate in the matrix. Thus, by utilizing the in-situ HVEM irradiation, an assumption can be applied that interstitial atoms escape towards the surface and the observed microstructural evolution can be governed by the diffusion of vacancies.

4.3 In-situ HVEM at Osaka University

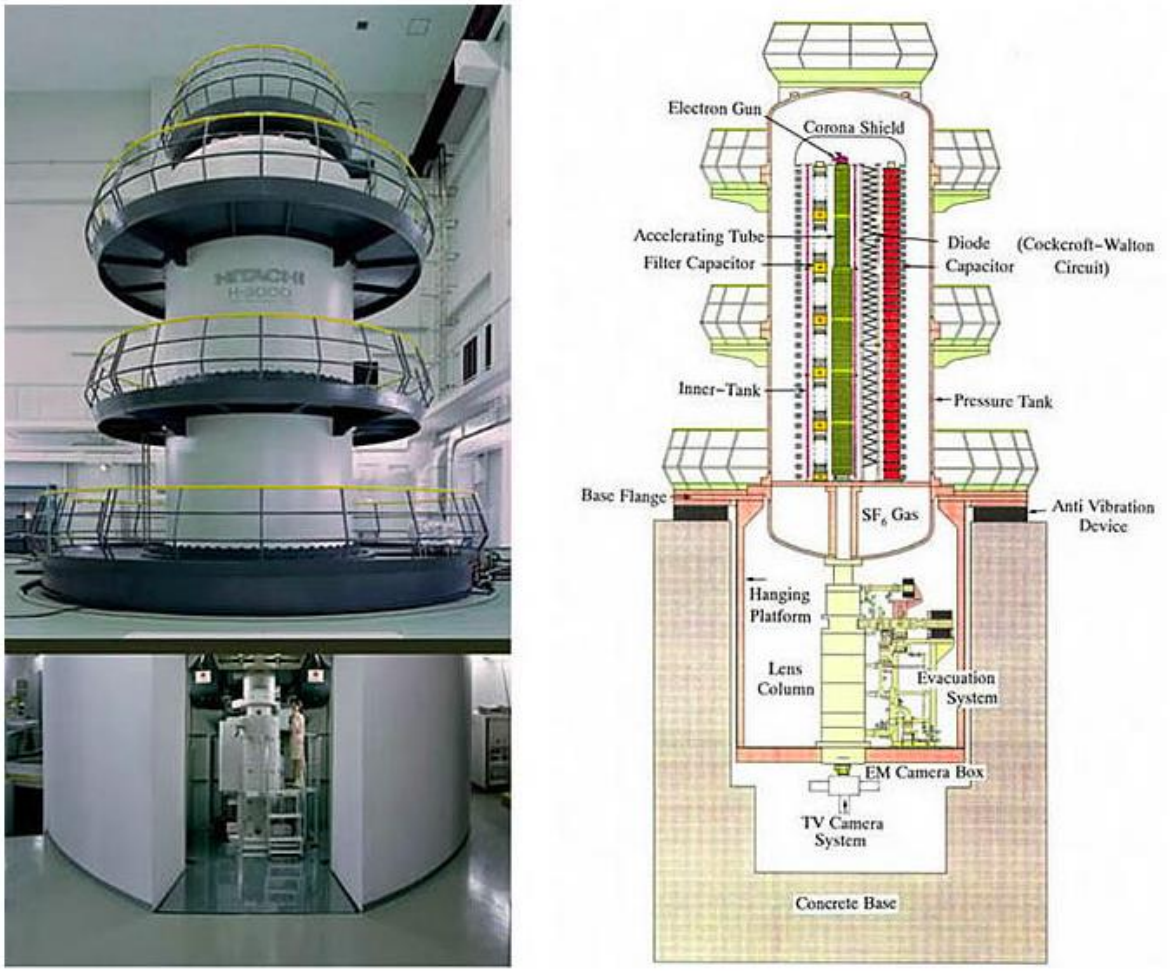

Fig. 4.3.1 Ultra High Voltage Electron Microscope (UHVEM) at Osaka University [31].

2 MeV in-situ electron irradiations were performed using Ultra-High Voltage Electron Microscopy (UHVEM) at the Research Center for UHVEM of Osaka University. Four different irradiations were performed, and each beam intensity distribution was measured with a Faraday cup which is coupled with the image shift function of the HVEM, and the focused beam intensity profiles were later fitted with Gaussian function. Due to the heterogeneous dispersion of nanoparticles, under the different irradiation experiments of the focused and the defocused beam conditions, the irradiation areas were carefully selected in which a similar

number of dispersed nanoparticles exist. The area of clustered nanoparticles was avoided to reduce experimental measurement errors for the precise size measurement of each nanoparticle. To ensure the precise measurement data, nanoparticles with distinctive contrast throughout the whole irradiation were analyzed. Also, the observation environment of nanoparticles did not change throughout the irradiation to achieve the nanoparticle size measurement in a precise manner. The microstructure evolution under irradiation was simultaneously observed in bright field image and recorded as digitized image using a CCD system.

In case of the Osaka University HVEM experiment, there were total of four experiments being performed. The controlled parameters were temperature and beam profile. The irradiation temperature of 723K and 823K along with beam profile of focused and defocused (uniform) were performed. The irradiation temperatures were selected based on typical Generation IV reactors operating temperature which ranges from 400 to 650 ^{e}C (673 – 923K). Under the focused beam irradiation, beam heating effect is anticipated as the maximum current locating at the center of the beam is several orders higher than the current locating at the periphery of the beam. Through utilizing the focused beam, based on the beam concentration gradient, its effect on diffusion phenomena is anticipated. However, under the uniform beam irradiation, beam heating effect can be negligible due to small observation area of interest. As the temperature distribution is rather homogeneous in the area of interest, the diffusion according to the temperature gradient can also be negligible. The magnification of the images was taken at 80,000. Through the in-situ observation, acquisition of time-sequential TEM images was possible. As the target of this research was to find a stability of nanoparticles, the acquired time-sequential images are valuable aspect of concluding the phenomena and mechanisms.

Table 4.3.1 Irradiation experimental conditions.

Osaka University		Hokkaido University
Operating voltage		
2 MV		1.25 MV
Temperature		
723K	823K	573K
Beam condition		
Uniform 1.73 x 10^{-4} dpa/s	Uniform 8.5 x 10^{-4} dpa/s	Uniform 8 x 10^{-4} dpa/s
Focused Max 3.13 × 10^{-2} dpa/s Min 2 × 10^{-4} dpa/s	Focused Max 0.18 × 10^{-2} dpa/s Min 7.8 × 10^{-4} dpa/s	

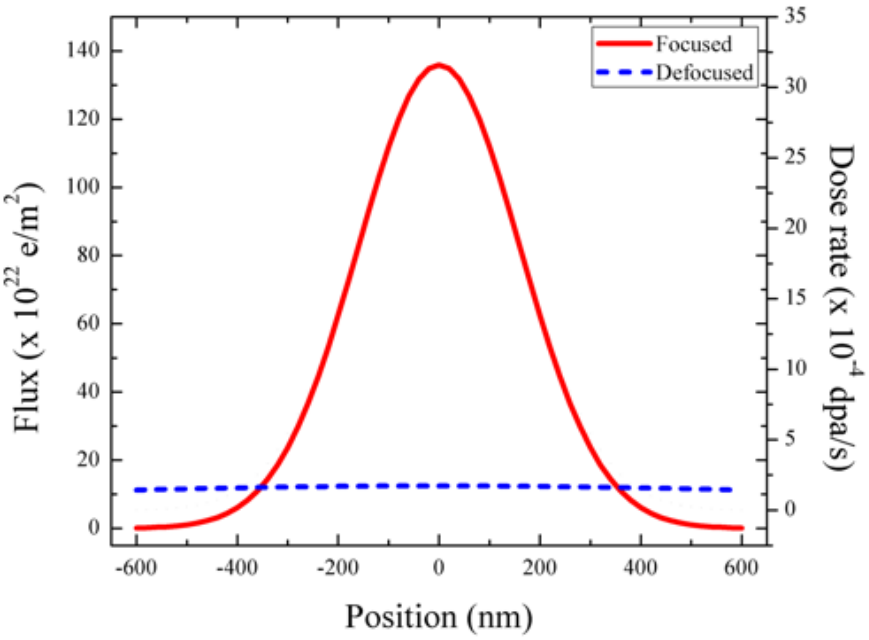

Fig. 4.3.2 Osaka HVEM beam intensity profiles for focused and defocused (uniform) beam irradiations under 2 MeV at 723K. Beam flux and dose rate are plotted with respect to position.

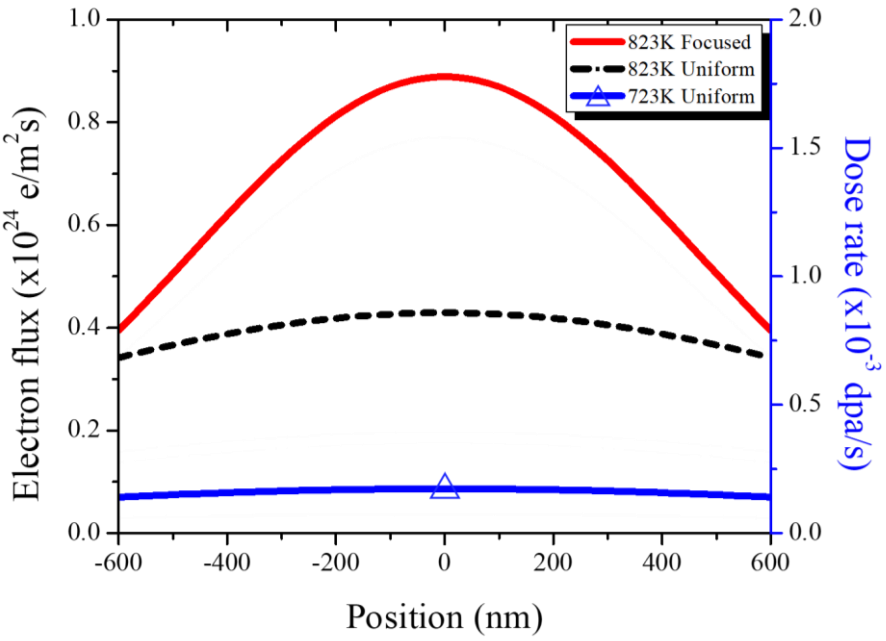

Fig. 4.3.3 Beam intensity profiles under 2 MeV for three different irradiation conditions: 823K focused beam, 823K uniform beam, and 723K uniform beam irradiations.

4.4 In-situ HRTEM at Hokkaido University

The single particle irradiation is performed using JEM-ARM1300 at Hokkaido University which is in-situ High Resolution TEM (HRTEM). This experiment is for the in-depth study on the dissolution mechanism of nanoparticle. The HRTEM was operated at 1.25 MeV with irradiation temperature at 573K. The images were taken at magnification of 300,000. The detailed description of the irradiation condition is mentioned in the previous chapter Table 4.3.1. In this experiment, time sequential TEM images were acquired for a long irradiation time up to 3480 s. Although there is an existence of beam profile for the Hokkaido HRTEM, unlike the Osaka HVEM the observation area was extremely small where one can easily ignore the effect of beam gradient.

From Fast Fourier Transformation (FFT) of the single nanoparticle, diffraction patterns are acquired time-sequentially. From Fast Fourier Transformation (FFT) of the single nanoparticle, diffraction patterns are acquired. From the detected diffraction patterns, Inverse

Fast Fourier Transformation (IFFT) was performed to acquire the interplanar distance. Areas corresponding to the interface between the NP and bulk were selected to closely investigate the dislocation movement under the electron irradiation.

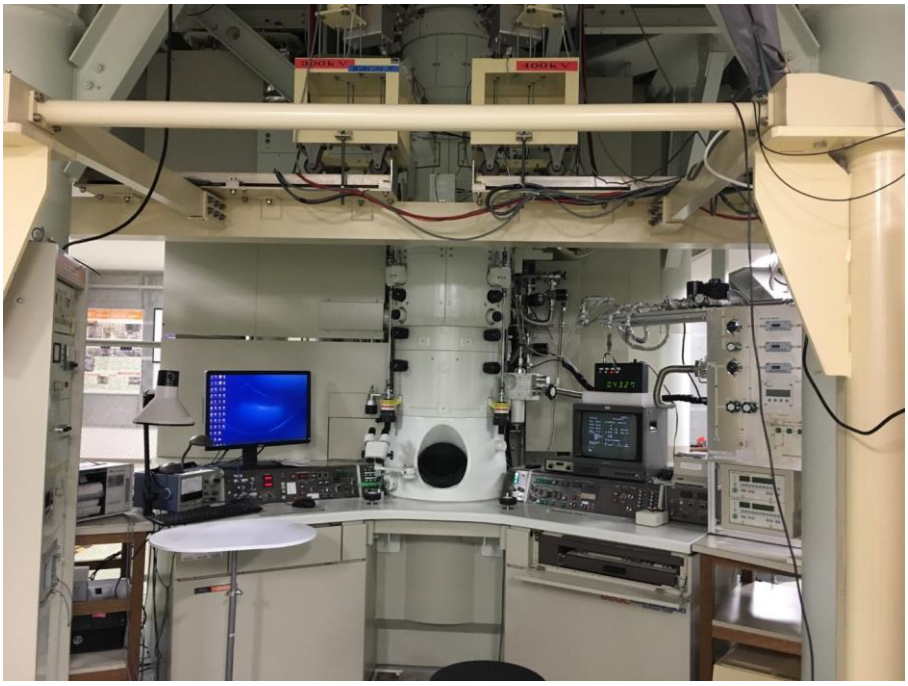

Fig. 4.4.1 High Resolution Transmission Electron Microscope (HRTEM) at Hokkaido University.

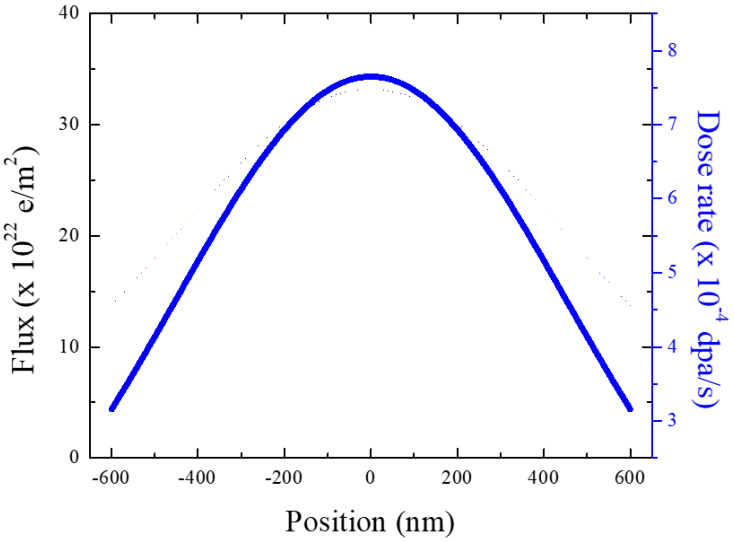

Fig. 4.4.2 Hokkaido HRTEM beam intensity profile. Beam flux and dose rate are plotted with respect to position.

CHAPTER 5.

In-situ 2 MeV Electron Irradiations at Elevated Temperatures

In-situ 2 MeV electron irradiations were performed on the 12Cr-ODS steel using Ultra-High Voltage Electron Microscopy (UHVEM) at Osaka University. Total of four different irradiations were performed with different beam profiles and temperature conditions. Due to the heterogeneous dispersion of nanoparticles, under the different irradiation experiments of the focused and the uniform beam conditions, the irradiation areas were carefully selected in which a similar number of dispersed nanoparticles exist. The area of clustered nanoparticles was avoided to reduce experimental measurement errors for the precise size measurement of each nanoparticle. To ensure the precise measurement data, nanoparticles with distinctive contrast throughout the whole irradiation were analyzed. As the investigation of the microstructure evolutions of nanoparticles is the main objective for this research, each nanoparticle in TEM images is carefully investigated with tracking of size and location for all time-sequential images as shown in Fig. 5.1.

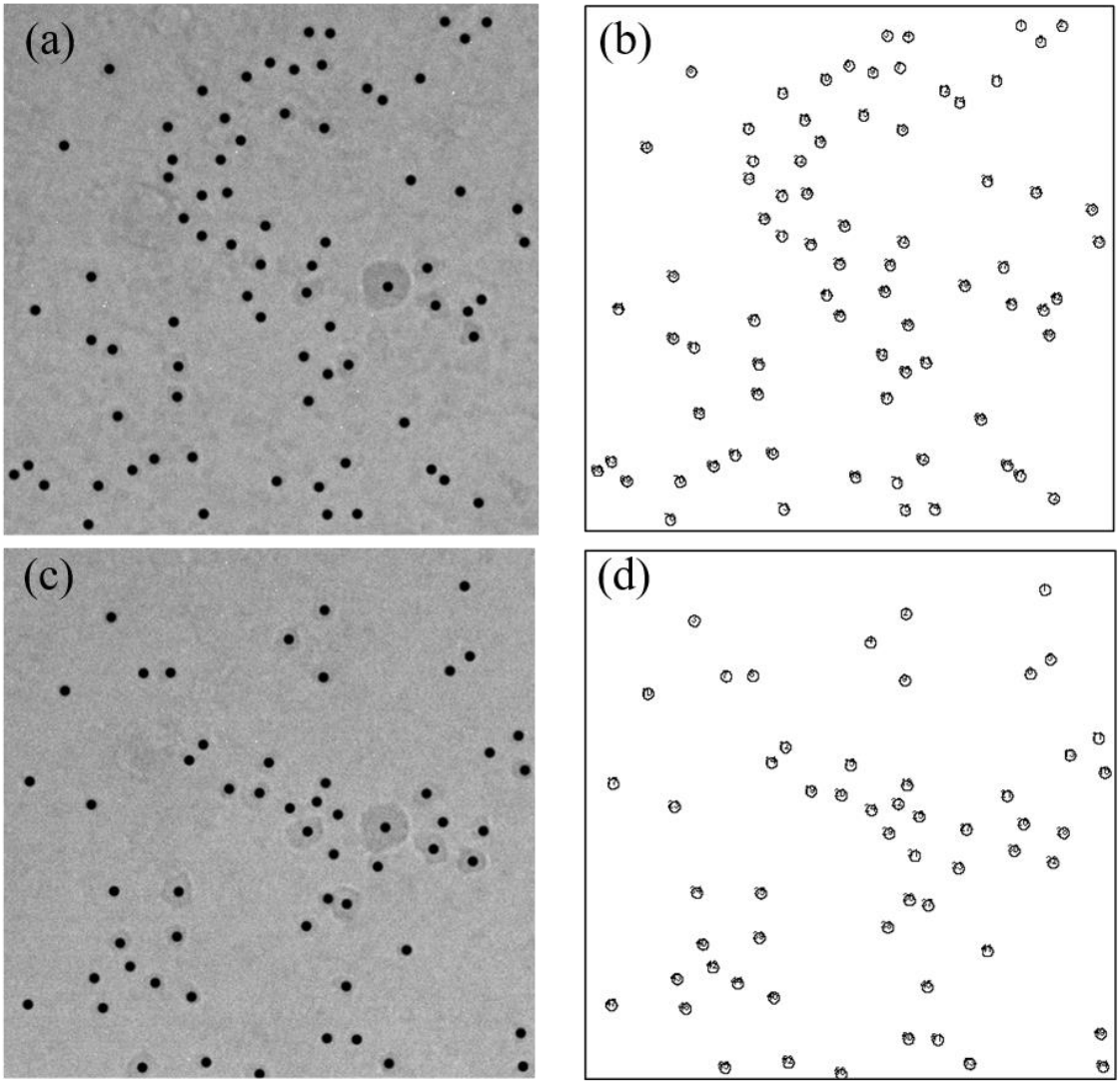

Fig. 5.1 Example of particle tracking in TEM image where the location of each nanoparticle was recorded. First image is before the irradiation and the second image is after 300 s irradiation under 2 MeV at 823K.

The flux profiles for the focused and the uniform beam condition differ significantly which also mean the flux range from minimum to maximum greatly vary. The main objective of this experiment was to observe the stability of nanoparticles under focused and uniform beam condition where the role of vacancy diffusion could be investigated. Under the focused beam irradiation with Gaussian distribution profile, dose rate which each nanoparticle receives greatly vary based on the location of existing nanoparticles. Thus, the instability of nanoparticles is described as volumetric change per fluence ($dV/d\Phi$) to precisely investigate

the microstructural evolution of nanoparticles. In this way, size change of each nanoparticle under the same total fluence could be accessed.

Also, the observation environment of nanoparticles did not change throughout the irradiation to achieve the nanoparticle size measurement in a precise manner. The microstructure evolution under irradiation was simultaneously observed in bright field image and recorded as digitized image using a CCD system. During the irradiation, images were taken thus time-sequential irradiated TEM images were acquired and analyzed.

From the TEM images during the irradiation, both the size and shape changes of the nanoparticles were detected. Then, the in-situ electron irradiations under the focused and the defocused beam were compared to investigate the effect of the vacancy concentration gradient on nanoparticle stability. To carefully investigate the microstructural evolution of the nanoparticles, as the observed shapes of nanoparticles were not perfect circles, explaining the evolution of nanoparticles using an equivalent diameter was considered inaccurate. Thus, the diameters in both major and minor axes were measured to calculate an area. Then, a mathematical assumption was applied to calculate the volume of nanoparticles by rotating ellipse-shaped nanoparticles about its minor axis so that all particles could be considered as oblate spheroids as shown in Fig. 5.2. The area to volume conversion calculation for ellipse-shaped nanoparticles is represented in Eq. 5.1. Also, the size change rate of the nanoparticle is represented as the change in volume per unit fluence as in Eq. 5.2.

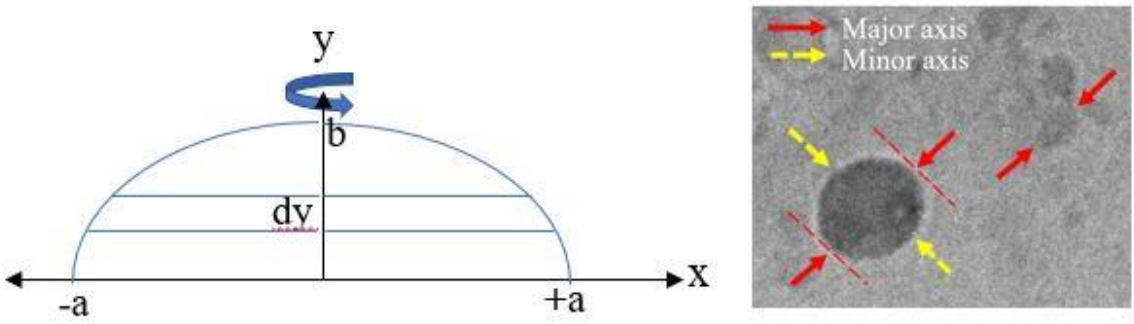

Fig. 5.2. Area to volume conversion calculation for nanoparticle which creates an oblate spheroid. Parameter *a* and *b* represent semimajor and semiminor axis respectively ($b < a$).

$$V = \pi \int_{-b}^{b} f(y)^2 dy = \pi \int_{-b}^{b} \pm a \left(\sqrt{1 - \frac{y^2}{b^2}} \right)^2 dy \qquad (5.1.1)$$

$$\frac{dV}{d\Phi} = \frac{dV}{d(\phi \mathrm{t})} = \frac{V_{final} - V_{initial}}{\phi(t_{final} - t_{initial})} \text{ in units of } \mathrm{nm}^3/(10^{25}\ \mathrm{e/m^2 s}) \qquad (5.1.2)$$

5.1 Results: Focused Beam

5.1.1 Focused Beam Irradiation at 723K

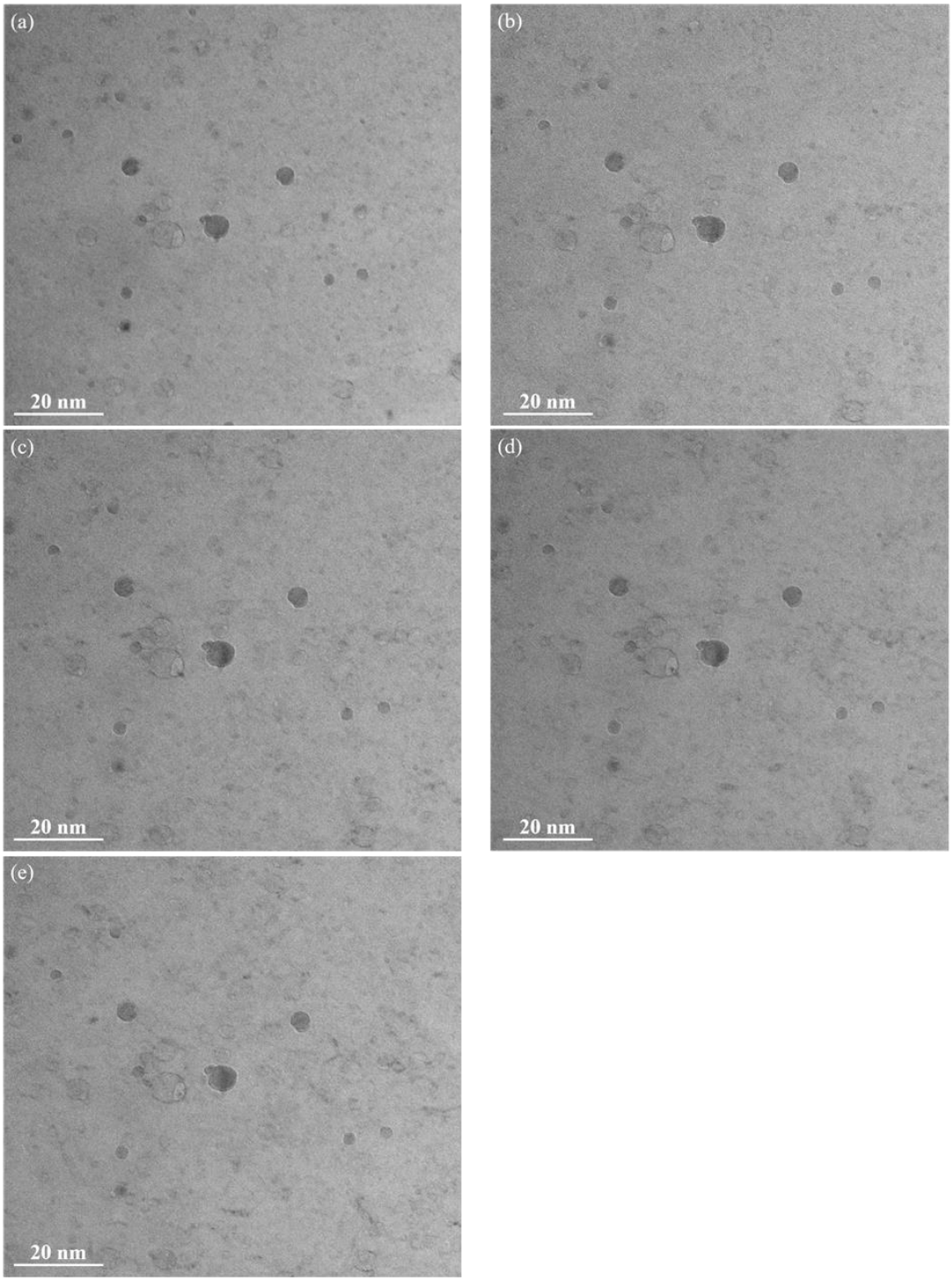

Fig. 5.1.1 Time-sequential TEM images of the irradiated 12Cr-ODS steel at 723K. (a) before irradiation, (b) 1.88 dpa, (c) 3.76 dpa, (d) 5.63 dpa and (e) 9.39 dpa irradiation. The mentioned dose is the maximum dose at the center of the beam which corresponds to the center of the images.

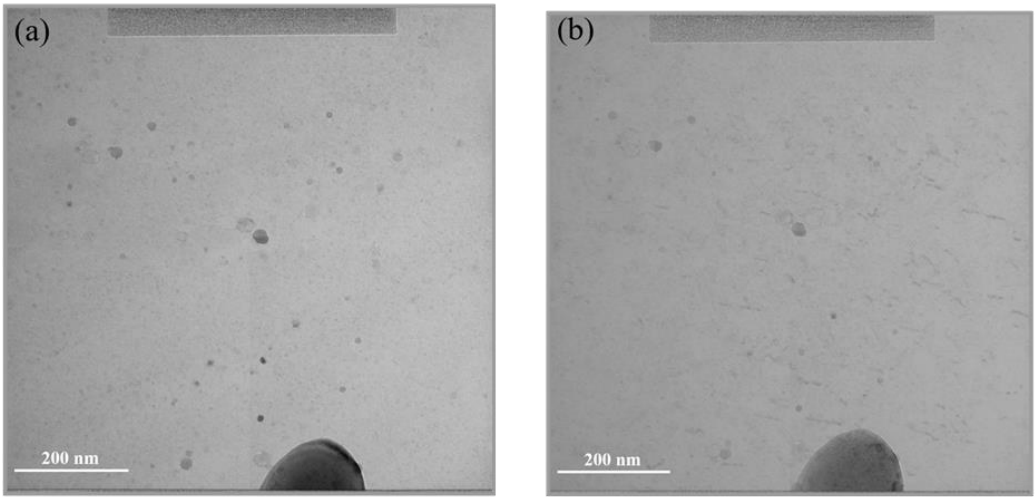

Fig. 5.1.2 TEM images of the 12Cr-ODS steel under the focused beam irradiation at 723K. (a) before irradiation and (b) after final irradiation 300 s. At 300 s irradiation, the maximum dose at the center is 9.39 dpa and minimum dose at the edge is 0.06 dpa.

The in-situ electron irradiation enables the detailed microstructural evolution of nanoparticle and the nanoparticles response in time-sequential short-time irradiation is investigated. The focused beam irradiation at 723K has minimum and maximum dose rate of 2×10^{-4} and 3.13×10^{-4} dpa/s, respectively. The volumetric change per fluence respect to the flux of both the focused and the defocused beam conditions in each consecutive irradiation time steps are shown in Fig. 5.1.3. In this figure, only the nanoparticles that survived till the end of the irradiation were plotted as the survived nanoparticles behavior should be distinguished apart from the disappeared nanoparticles. In both irradiation conditions, non-linear volumetric fluctuation have occurred. However, as the irradiation proceeds, the nanoparticles seem to gradually stabilized. This stochastic size fluctuation mainly occurred at the low flux region under 1.6×10^{23} e/m^2. At the higher flux region which only applies to part of the focused beam irradiation, the instability of nanoparticles was not dominant.

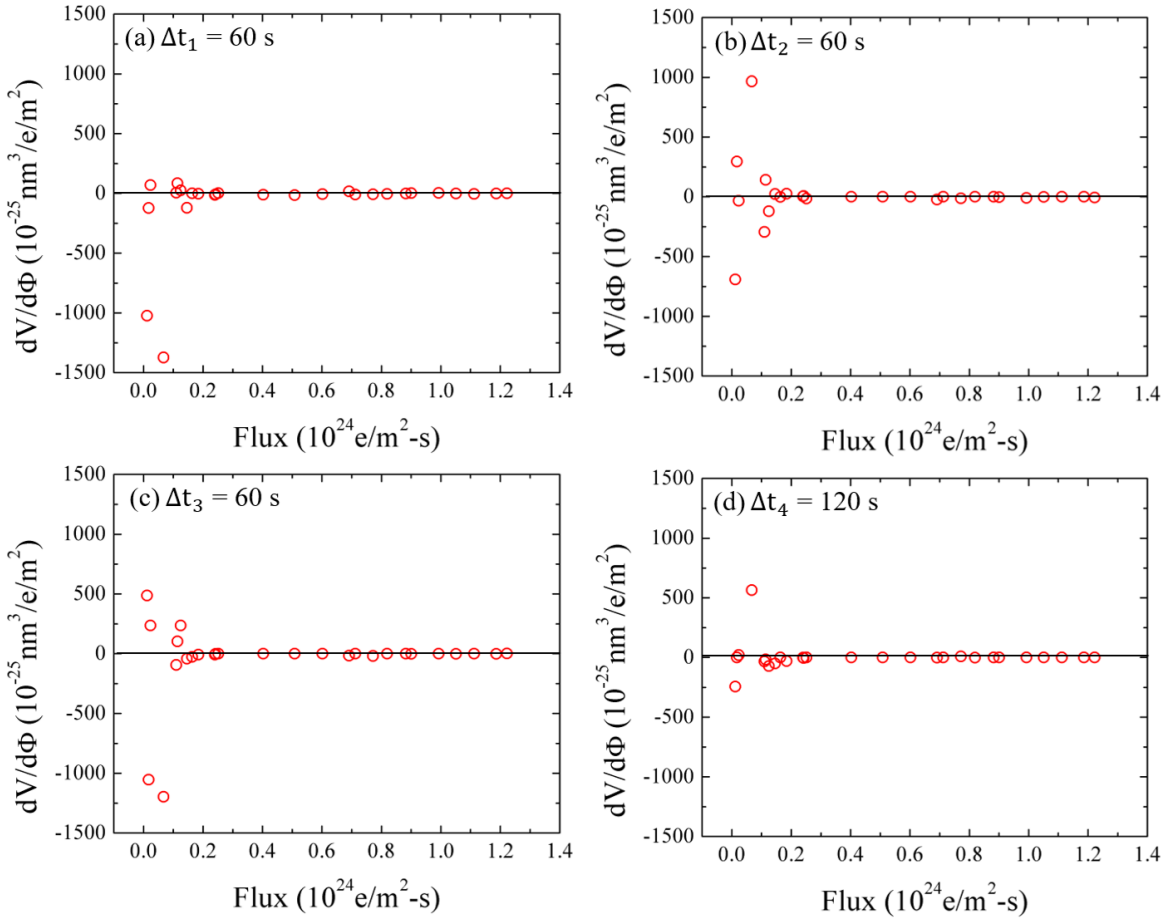

Fig. 5.1.3 Volumetric change throughout each irradiation interval under the focused beam irradiation.

All the disappeared nanoparticles under the focused beam condition were identified as small volume nanoparticles. Also, among the disappeared nanoparticles, there was no clear relation of received dose nor variation in initial size even among the small nanoparticles. This disappearance of nanoparticles only under the focused beam condition could be explained by total displacement per atom, beam heating effect.

In the focused beam condition, the received electron flux for each nanoparticle can vary significantly based on their irradiation location. Under the focused beam condition, the total dose varied from 4.2×10^{-2} up to 9.4 dpa. The disappeared nanoparticles under the focused beam condition have received a much higher dose of irradiation. Also, for the focused beam irradiation with high beam current, the beam heating effect should be considered for the

dissolution of nanoparticles as the rise in local temperature can be induced by an electron beam [46]. Thus, the disappeared nanoparticles could be influenced by the rise of the temperature which leads to an increase in vacancy diffusion.

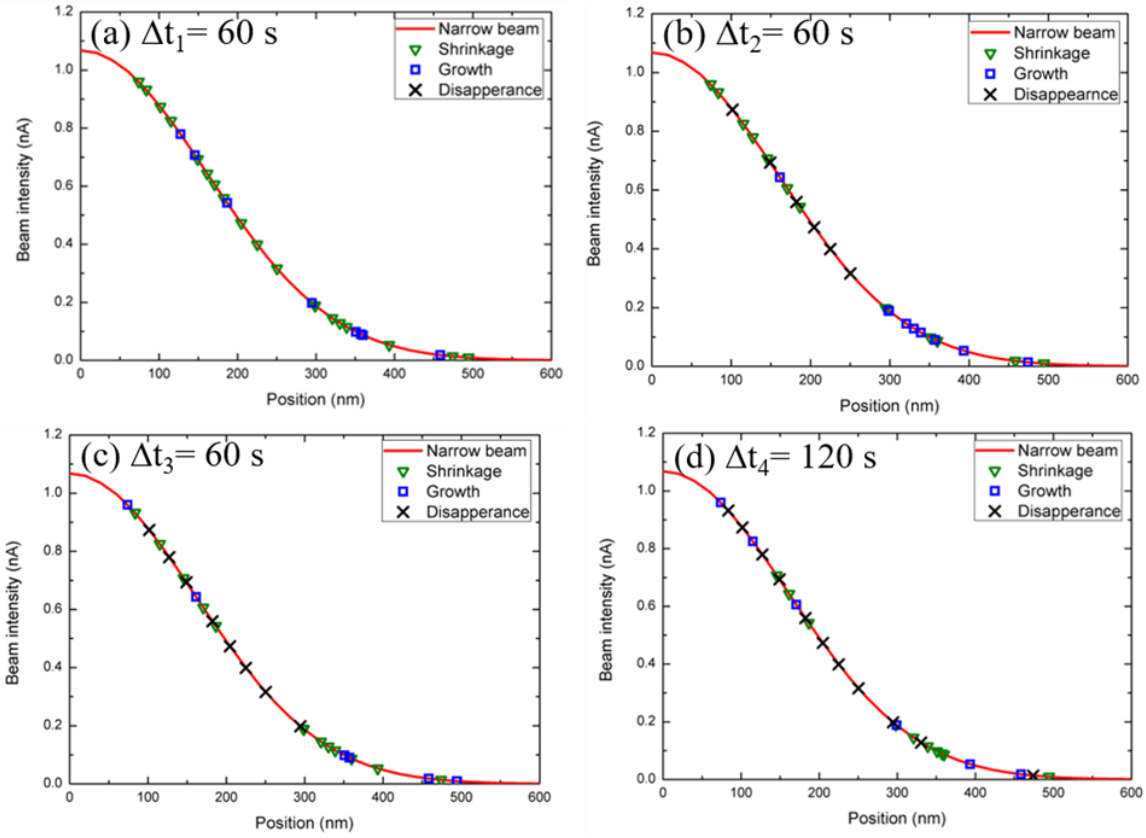

Fig. 5.1.4 Microstructure state of the nanoparticles during the focused beam irradiation at 723K. (a) 60 s, (b) 120 s, (c) 180 s and (d) 300 s irradiation.

To further clarify the microstructure evolution under the focused beam irradiation, microstructure state of the nanoparticles during each irradiation time step is plotted in Fig. 5.1.4. From the microstructure state of the nanoparticles figure, disappearance and shrinkage of nanoparticles under the high beam current region are observed. Most nanoparticles have quickly disappeared under the short time irradiation. However, near the periphery or tail of the beam, the nanoparticles were survived with the mixture of both growth and shrinkage.

5.1.2 Focused Beam Irradiation at 823K

2 MeV focused beam irradiation at 823K was performed on the 12Cr-ODS steel using H-3000 at Osaka University. Time-sequential TEM images were acquired with the minimum and maximum dose rate of 7.8×10^{-4} and 0.18×10^{-2} dpa/s, respectively. Under the focused beam irradiation at 823K, severe sublimation especially near the center of the radiation beam is observed. The particle number density decreases dramatically, and all the nanoparticles undergo size decrease. This result differs from the focused beam irradiation at 723K. Under the 723K focused beam irradiation, while many nanoparticles disappeared, still few nanoparticles undergo growth and shrinkage and survived till the end. However, in the case of 823K focused beam irradiation, most of all nanoparticles with small diameter immediately disappeared and only the large nanoparticles with diameter larger than 10 nm survived. Thus, comparing with the 723K focused beam irradiation, under 823K focused beam irradiation, gradual shrinkage of larger nanoparticles and decrease in number density were dominant. Based on the diffraction patterns for before and after the irradiation, it is confirmed that even under this severe sublimation there was no amorphization.

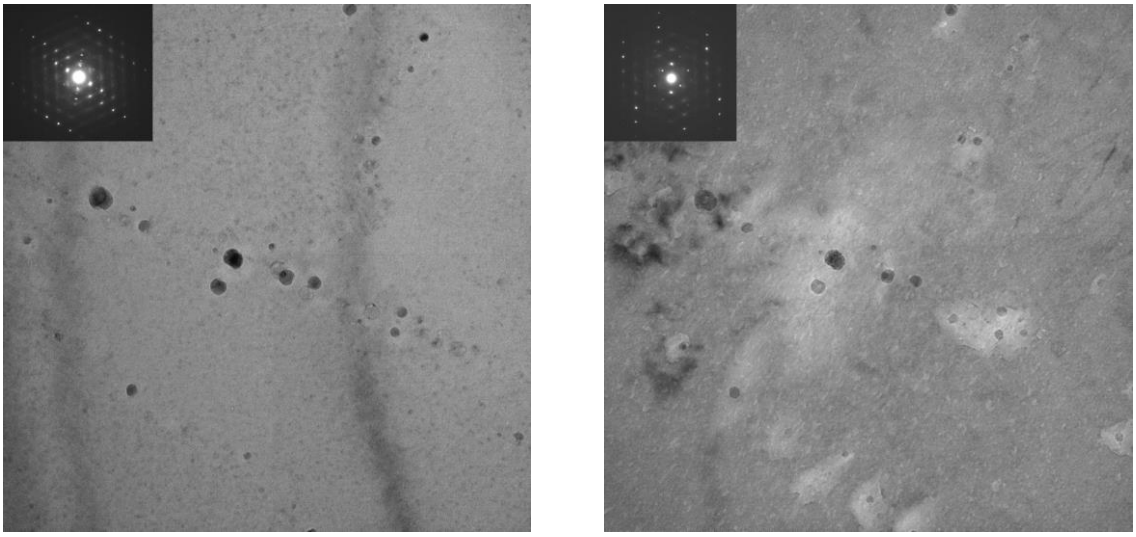

Fig. 5.1.4 Diffraction pattern and TEM image of 12Cr-ODS steel at 823K before and after the irradiation of 2.16 dpa.

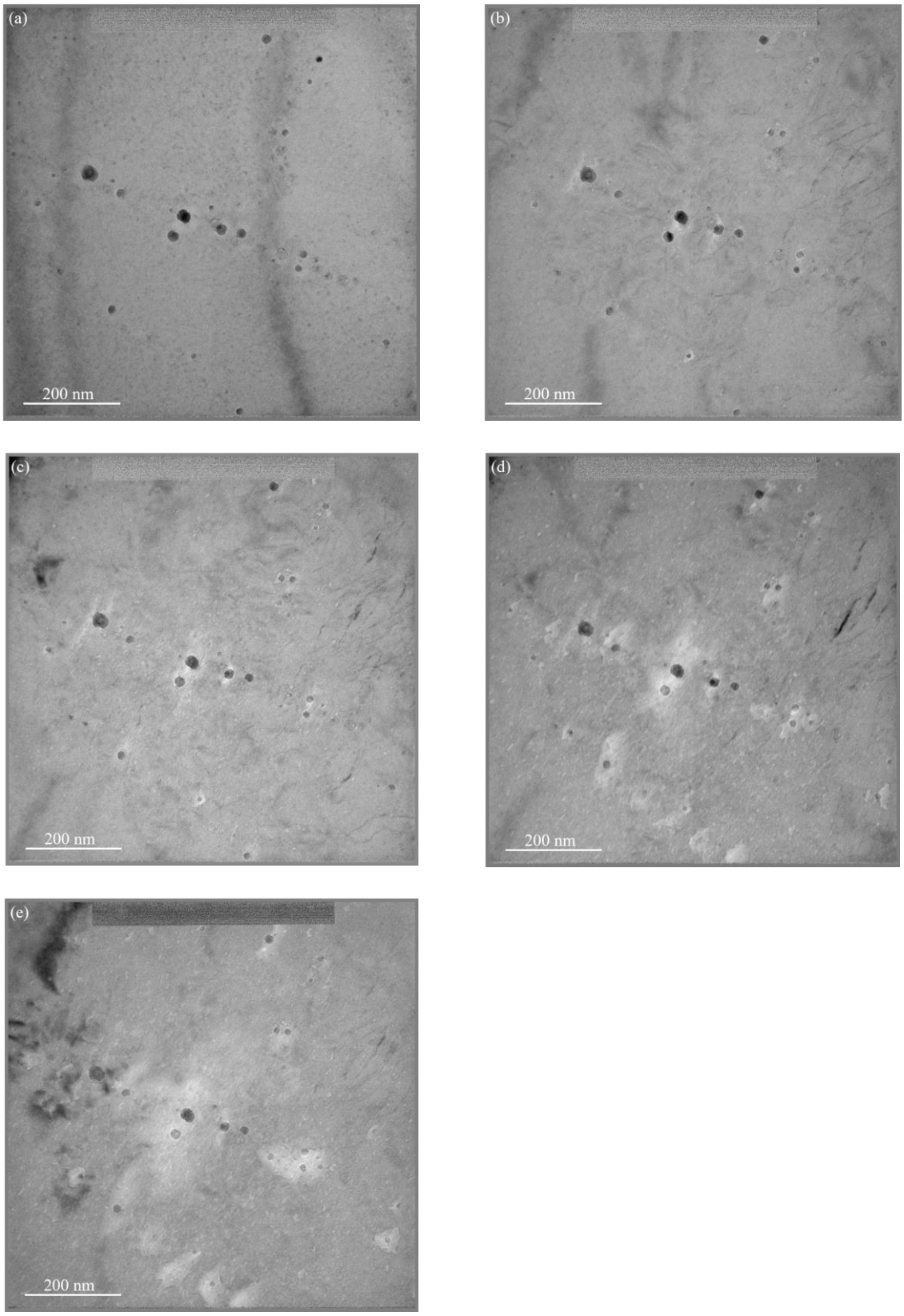

Fig. 5.1.5 Time-sequential TEM images of the irradiated 12Cr-ODS steel at 823K. (a) before irradiation, (b) 0.22 dpa , (c) 0.54 dpa, (d) 1.08 dpa and (e) 2.16 dpa irradiation. The dose mentioned is the maximum dose at the center of the beam.

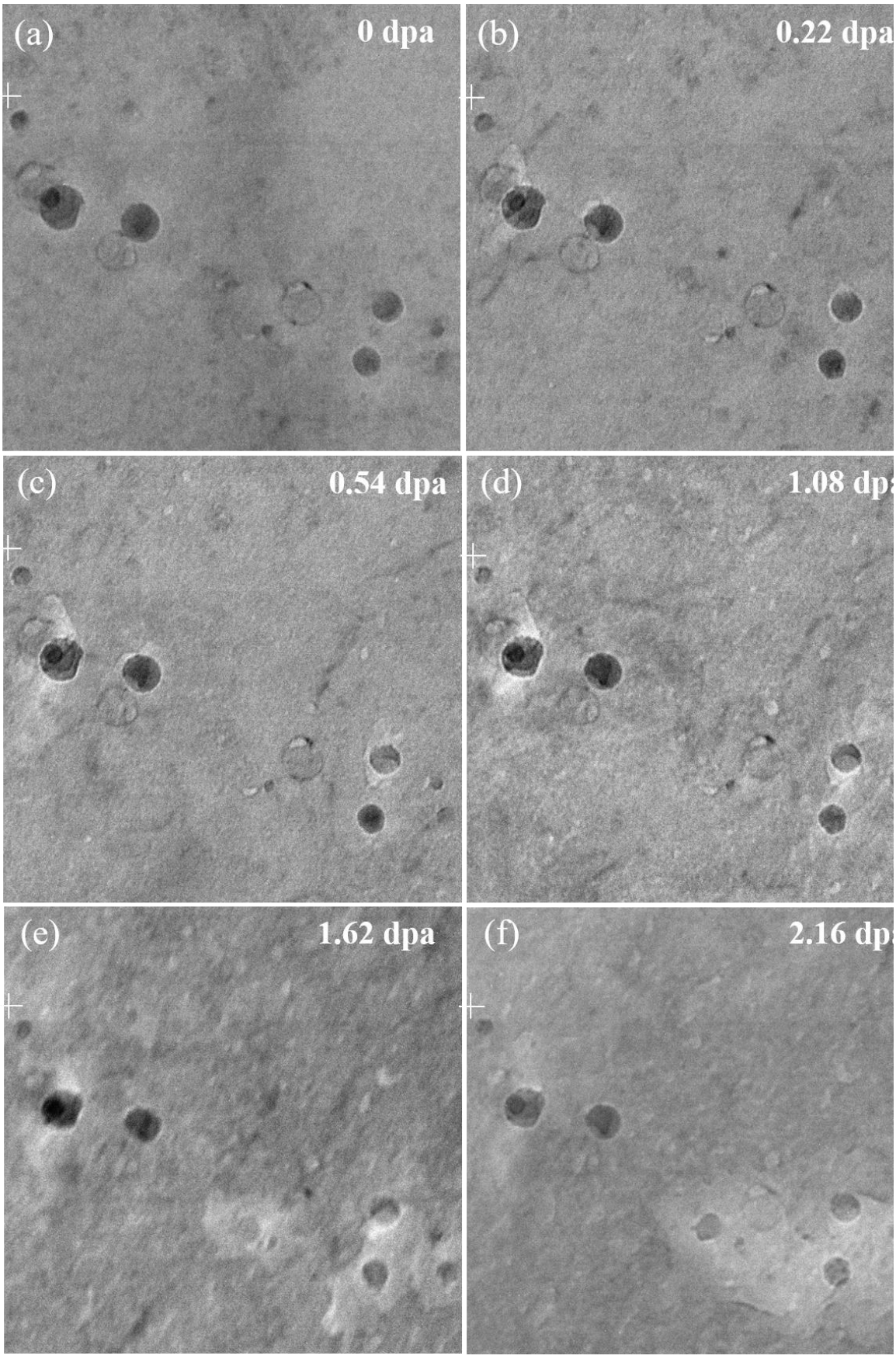

Fig. 5.1.6 Time-sequential TEM images of the focused beam irradiation at 823K. (a) before irradiation, (b) 0.22 dpa , (c) 0.54 dpa, (d) 1.08 dpa, (e) 1.62 dpa and (f) 2.16 dpa irradiation.

5.2 Discussion

5.2.1 Beam Sputtering

Under the focused beam condition of the Gaussian beam profile, many small sized nanoparticles have disappeared. This result could be explained by beam heating effect. Unlike the uniform beam irradiation, under the focused beam where the maximum beam current is several orders higher than the minimum beam current, nanoparticles and surrounding matrix under the strong beam current can easily sublimated. Thus, at the center of the focused beam where the current/flux is the maximum, temperature could increase which also leads to increase in vacancy diffusion. Through utilizing the focused beam, based on the beam concentration gradient, its effect on diffusion phenomena is anticipated. However, under the uniform beam irradiation, beam heating effect can be negligible due to small observation area of interest. As the temperature distribution is rather homogeneous in the area of interest, the diffusion according to the temperature gradient can also be negligible. This beam sputtering effect was only observed for the focused beam irradiation cases at 723K and 823K.

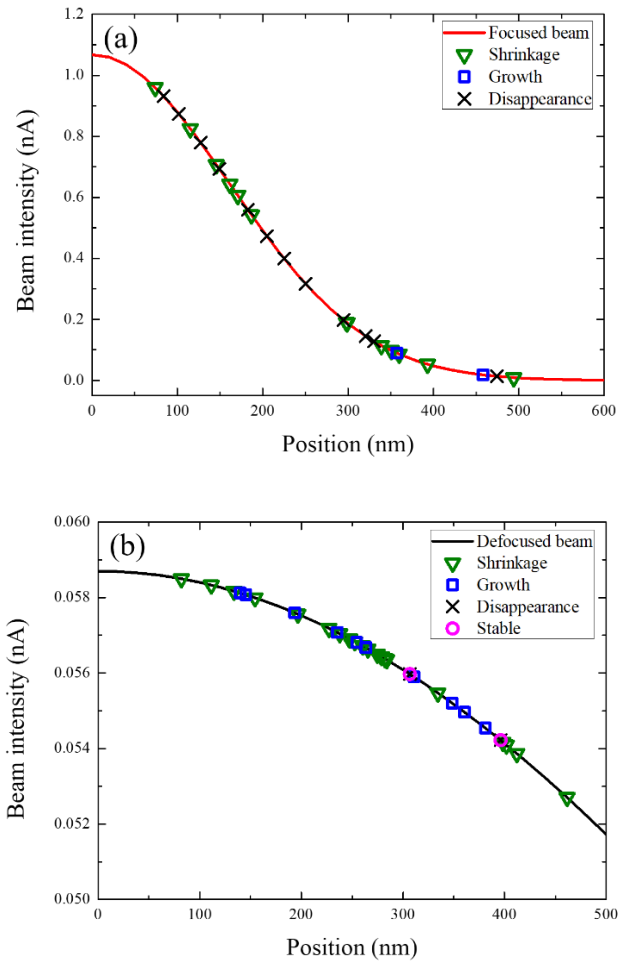

Fig. 5.2.1 Final microstructure state of nanoparticles under (a) the focused and (b) the uniform beam irradiation at 723K.

5.2.2 Vacancy Concentration Gradient Effect

The effect of vacancy concentration gradient on nanoparticle instability was investigated by comparing the two beam conditions at the same irradiation time, and higher volumetric fluctuation under the focused beam condition was found. Due to a sharp peak along the Gaussian beam profile, the vacancy concentration gradient yields vacancy flow which could contribute in a rapid dissolution of nanoparticles.

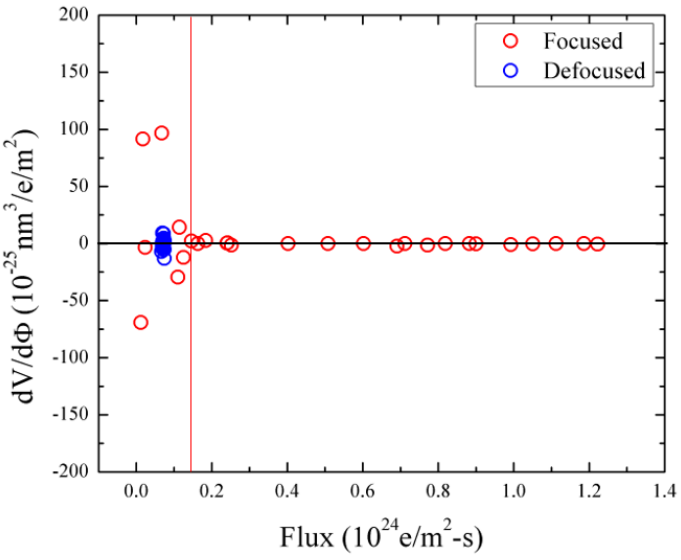

Fig. 5.2.2 Comparison of volumetric change per fluence respect to flux for two beam conditions after 120 s irradiation.

Fig. 5.2.2 compares the volumetric change of nanoparticles under the two beam conditions at the same irradiation time step of 120 s. From the figure, the magnitude of size fluctuation was much higher under the focused beam condition. Also, the occurrence of nanoparticle instability under the flux 1.6×10^{23} e/m^{2}s which is indicated by the red line was once again confirmed. This different magnitude of size fluctuation of nanoparticles under the two beam conditions can be explained by vacancy concentration gradient. In the focused beam condition, a sharp peak with a large gradient exists along the Gaussian beam profile. This focused beam distribution represents the vacancy concentration gradient, and this vacancy concentration gradient yields vacancy flow which could result in a rapid dissolution of nanoparticles.

5.3 Results: Uniform Beam

5.3.1 Uniform Beam Irradiations at 723K

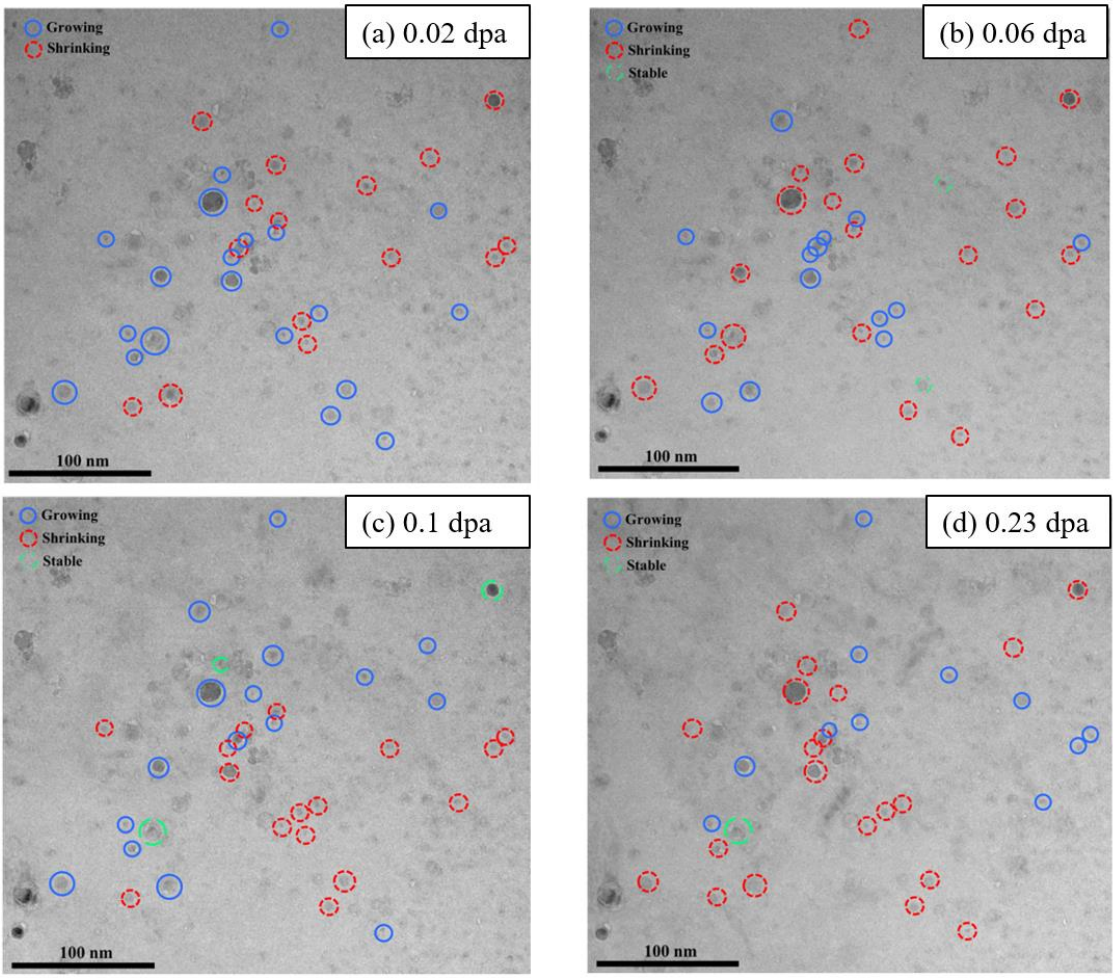

Fig. 5.3.1 Microstructure evolution during the defocused beam irradiation of 1.72×10^{-4} dpa/s: target tracking nanoparticles were marked with blue, red and green circles which represent growing, shrinking and stable, respectively.

2 MeV uniform beam irradiation at 723K was performed on the 12Cr-ODS steel using H-3000 at Osaka University. Time-sequential TEM images were acquired with the dose rate of 1.73×10^{-4} dpa/s. Total of five TEM images were acquired and irradiation was stopped at 0.23 dpa as shown in Fig. 5.3.1. The volumetric change of each nanoparticle was tracked and plotted in Fig. 5.3.2. Based on Fig. 5.3.2, in each irradiation time step, volumetric fluctuation of nanoparticles is obvious. However, towards the end of the irradiation at 0.23 dpa, the volumetric fluctuation is nearly negligible and seem to reach steady-state. To correlate this

volumetric fluctuation with beam condition, Fig. 5.3.3. is plotted which describes the microstructure state of each nanoparticle under the corresponding beam profile. Unlike the focused beam irradiation result, random mixture of growth, shrinkage and stable state of nanoparticles were observed throughout the irradiation.

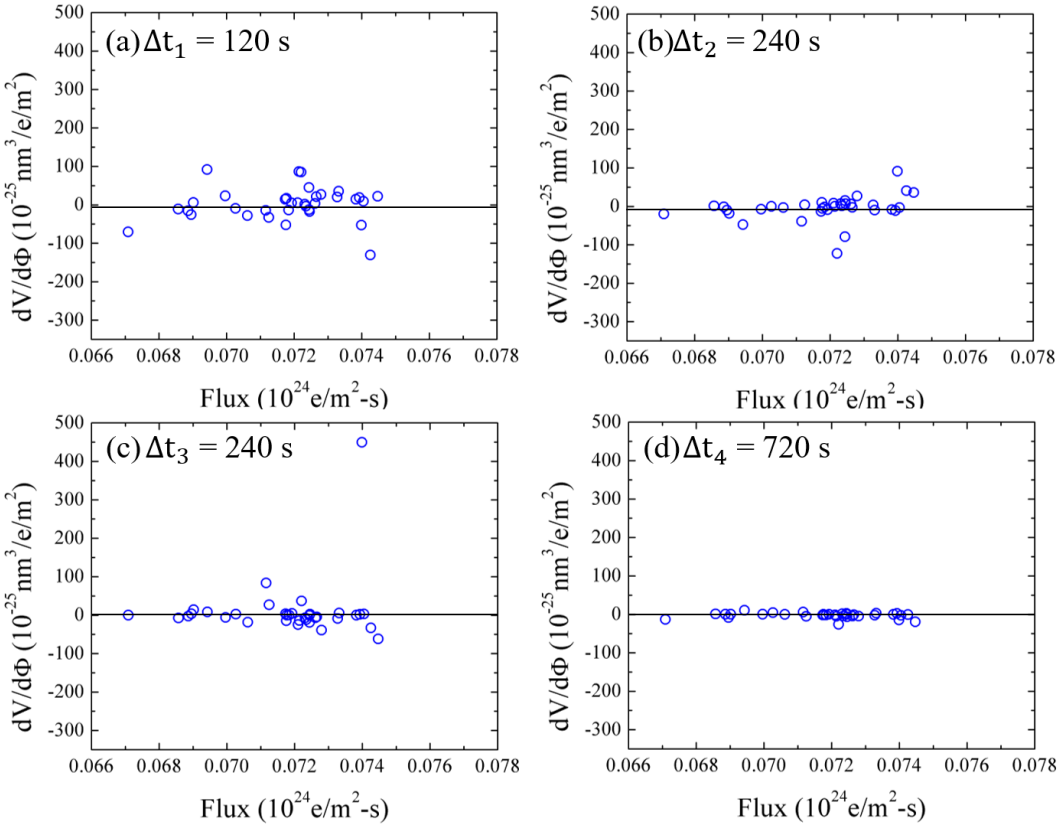

Fig. 5.3.2 Volumetric change respect to flux under the uniform irradiation at 723K. (a) 0.02 dpa, (b) 0.06 dpa, (c) 0.1 dpa and (d) 0.23 dpa irradiation.

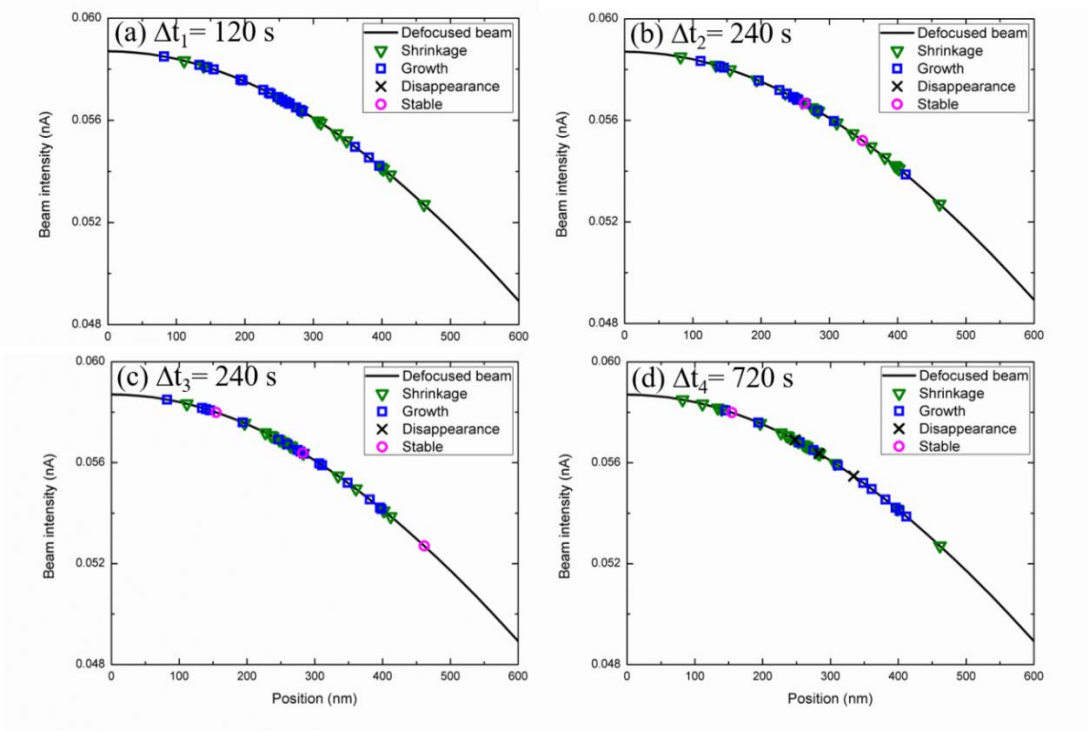

Fig. 5.3.3 Time sequential microstructure evolutions during the uniform beam irradiation with a total time 1320 s. (a) 0.02 dpa, (b) 0.06 dpa, (c) 0.1 dpa and (d) 0.23 dpa irradiation.

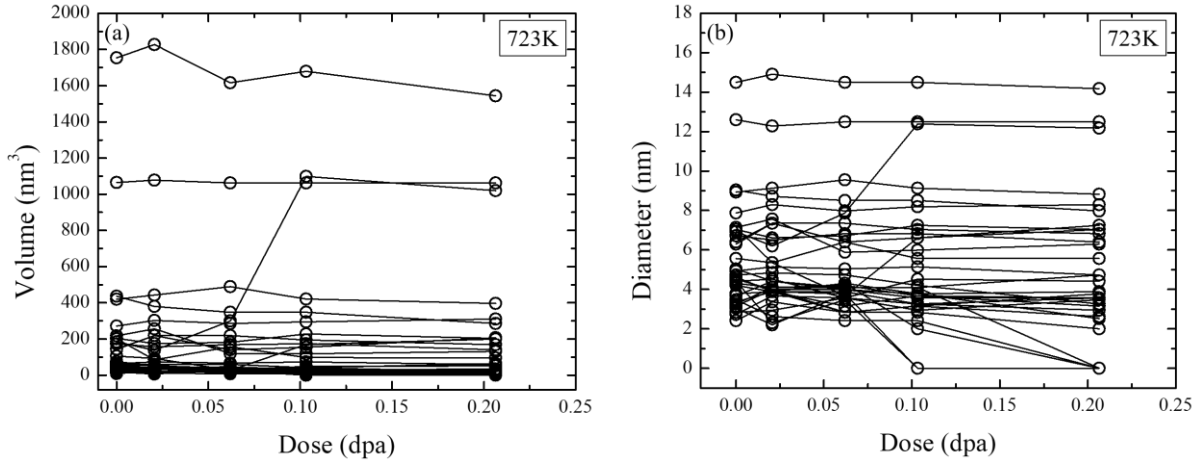

Fig. 5.3.4 Size evolution of nanoparticles during 2 MeV irradiation at 723K represented by (a) volume and (b) equivalent diameter.

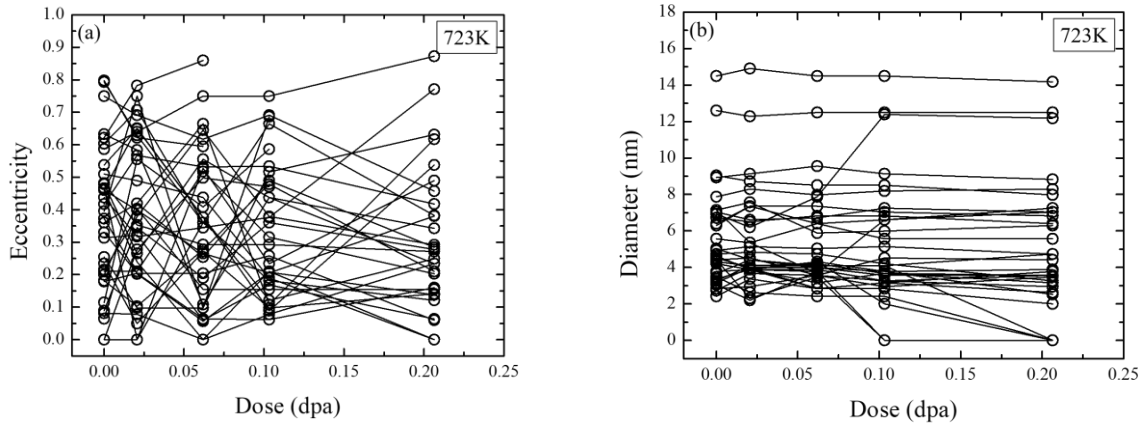

Fig. 5.3.5 Shape and size evolution of nanoparticles during 2 MeV irradiation at 723K represented by (a) eccentricity and (b) equivalent diameter.

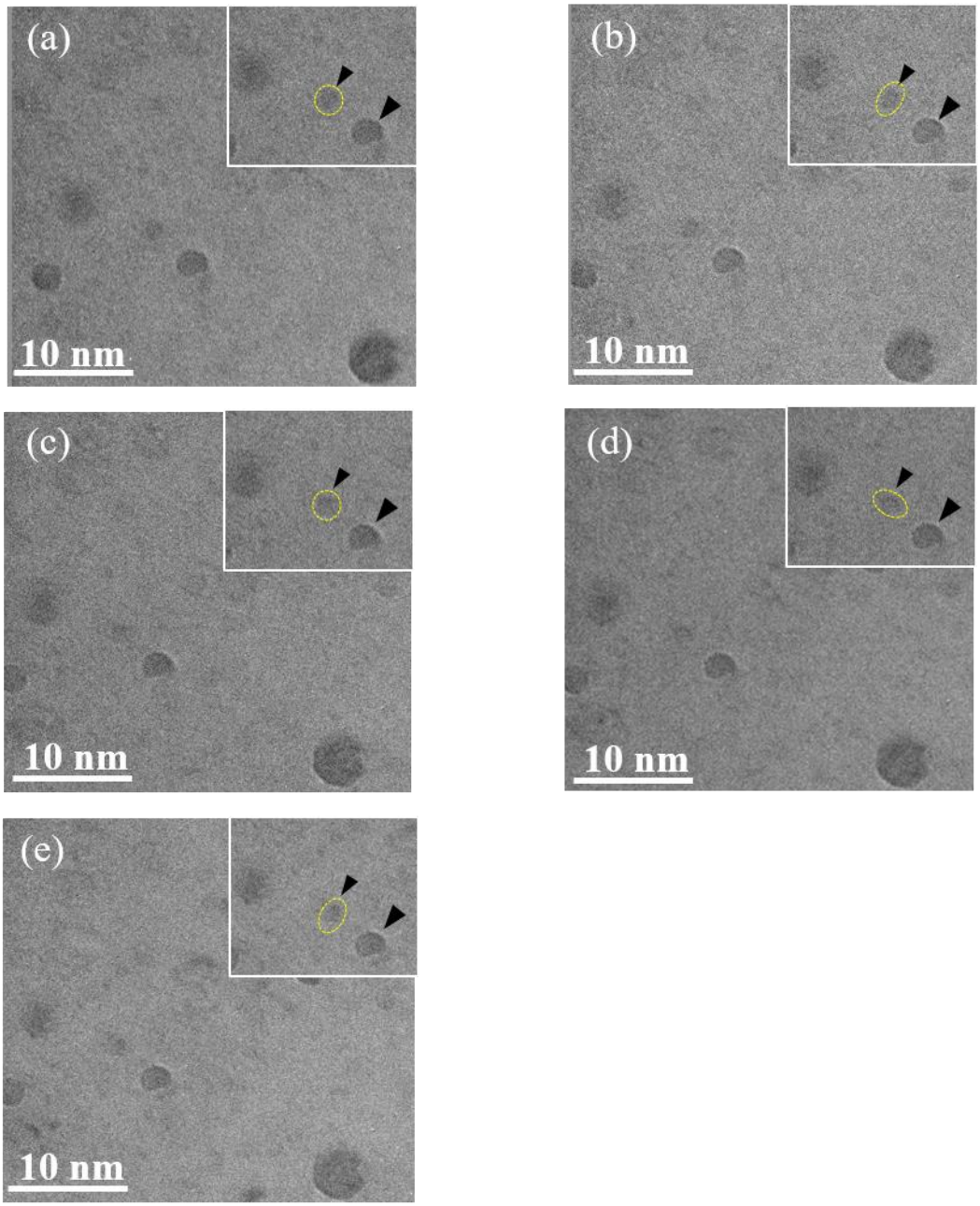

Fig. 5.3.6 Microstructure evolution of two neighboring nanoparticles under in-situ electron irradiation and upper-right inserted figure represents traced image. (a) unirradiated, (b) 0.02 dpa, (c) 0.06 dpa, (d) 0.1 dpa and (e) 0.23 dpa.

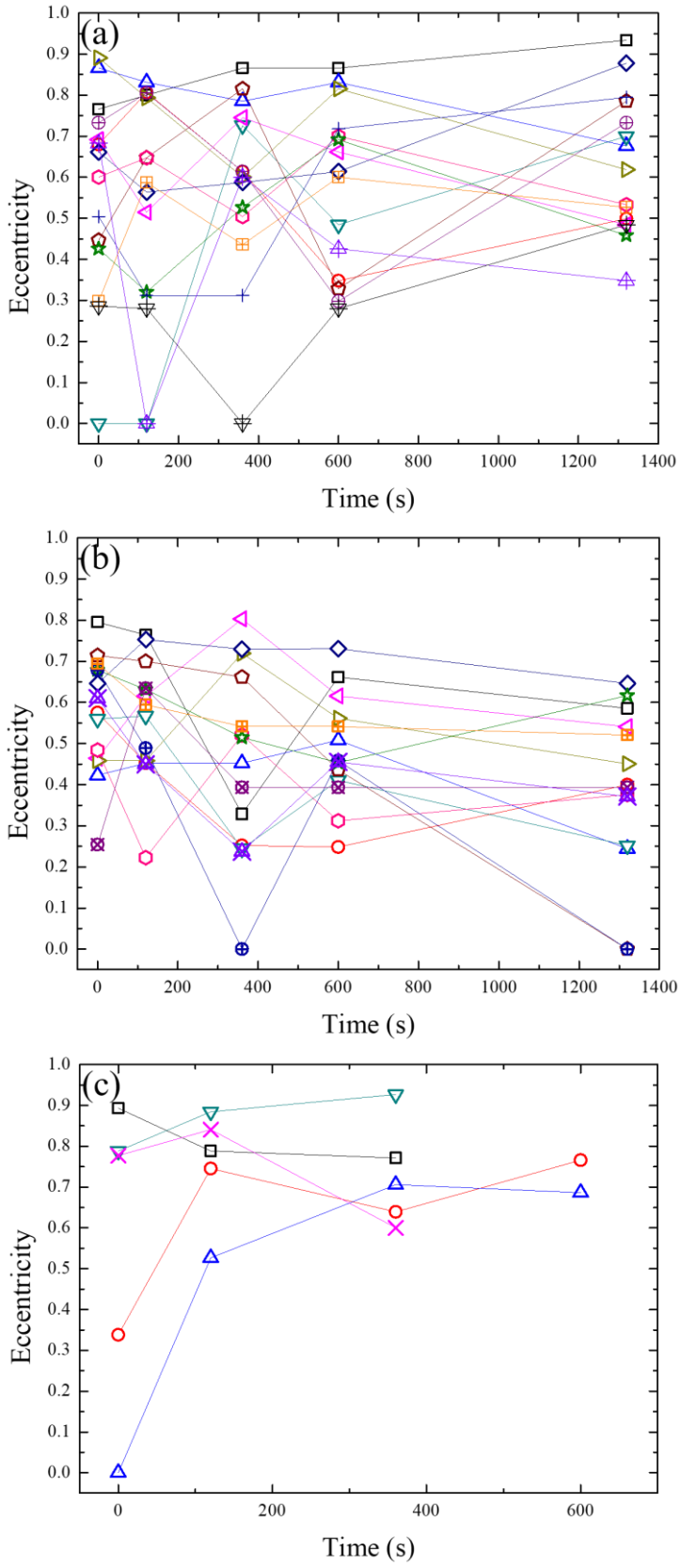

Fig. 5.3.7 Eccentricity time evolution categorized by volume under the defocused beam irradiation condition. (a) small volume, (b) larger volume, and (c) disappeared nanoparticles during irradiation.

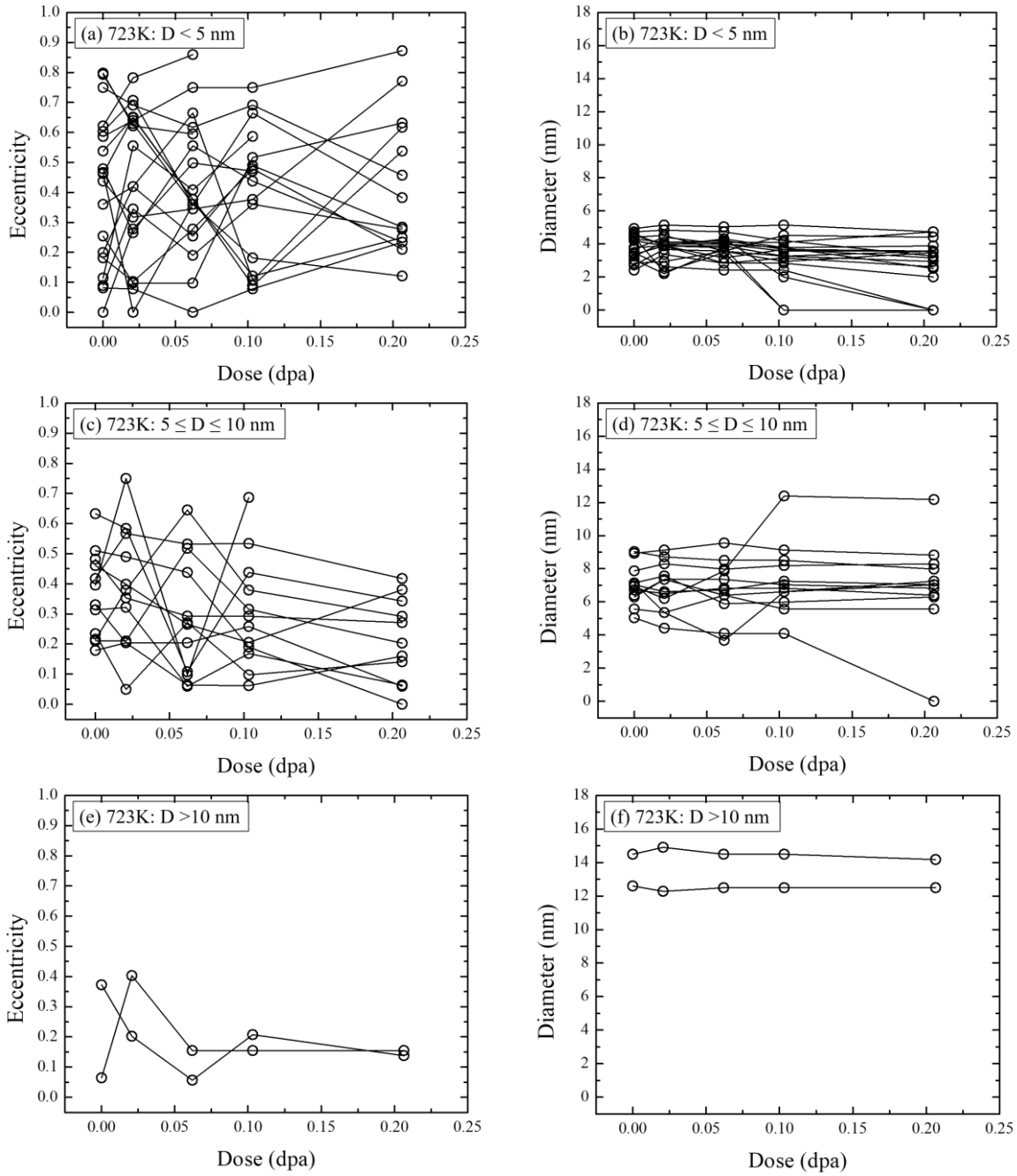

Fig. 5.3.8 Shape and size evolution of nanoparticles during 2 MeV irradiation at 723K categorized by (a),(b) of diameter smaller than 5 nm, (c),(d) of diameter between 5 and 10 nm, and (e),(f) of diameter larger than 10 nm.

Also, the shape evolution of nanoparticles was observed throughout the short-time irradiation steps. In the figure, two neighboring nanoparticles had microstructure evolution in which the small nanoparticle continued to shrink along with its change in shape, while the bigger nanoparticle grew while receiving the same dose.

A shape factor of eccentricity is employed to further understand the microstructural evolution of nanoparticles: as a shape can still change under no volumetric change. Under the uniform irradiation at 723K, the small sized nanoparticles became elongated while the larger nanoparticles became spherical. In this study, the eccentricity was used to represent the evolution of ellipsoid under the irradiation. As previously mentioned, during the volume calculation, the mathematical assumption was applied to rotate all the ellipse about its minor axis which results in an oblate spheroid. Thus, both measured major and minor axes of nanoparticles were used to calculate eccentricity which describes the shape of an ellipsoid.

$$\text{Eccentricity} = 1 - \frac{b^2}{a^2} \quad \text{for oblate spheroid (b < a)} \tag{5.3.1}$$

Based on the categorized volume of nanoparticles, the eccentricity of each nanoparticle is plotted with respect to irradiation time. Interestingly, the small nanoparticles seem to exhibit the increasing trend of eccentricity at the final irradiation state while the larger nanoparticles exhibited decreasing trend. The disappeared nanoparticles were all categorized as small nanoparticles and until the disappearance, they exhibited an increasing trend which corresponds with the figure for small nanoparticles.

5.3.2 Uniform Beam Irradiations at 823K

2 MeV uniform beam irradiation at 823K was performed on the 12Cr-ODS steel using H-3000 at Osaka University. Time-sequential TEM images were acquired with the dose rate of 8.5×10^{-4} dpa/s. Total of 6 TEM images were acquired and irradiation was stopped at 2.06 dpa as shown in Fig. 5.3.6. To investigate the microstructure evolution of nanoparticles, two different regions were selected and magnified to detect any changes, and these are shown in Fig. 5.3.8 – Fig. 5.3.10. Due to inhomogeneous dispersion of nanoparticles, under this experiment, the irradiated area has higher number of nanoparticles than the previous

experiment of uniform beam irradiation at 723K. This high number of nanoparticles in the specimen is shown in Fig. 5.3.9 and Fig. 5.3.10.

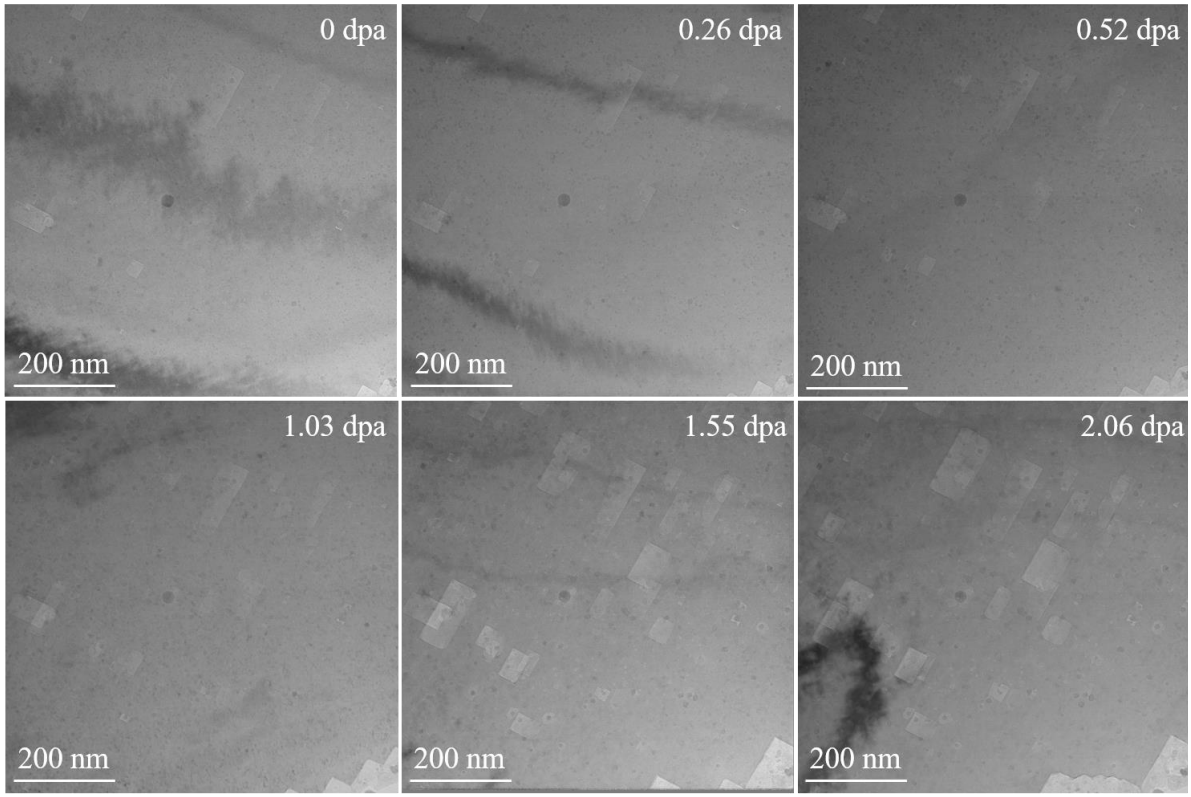

Fig. 5.3.6 Time-sequential TEM images of 2 MeV uniform beam irradiation at 823K.

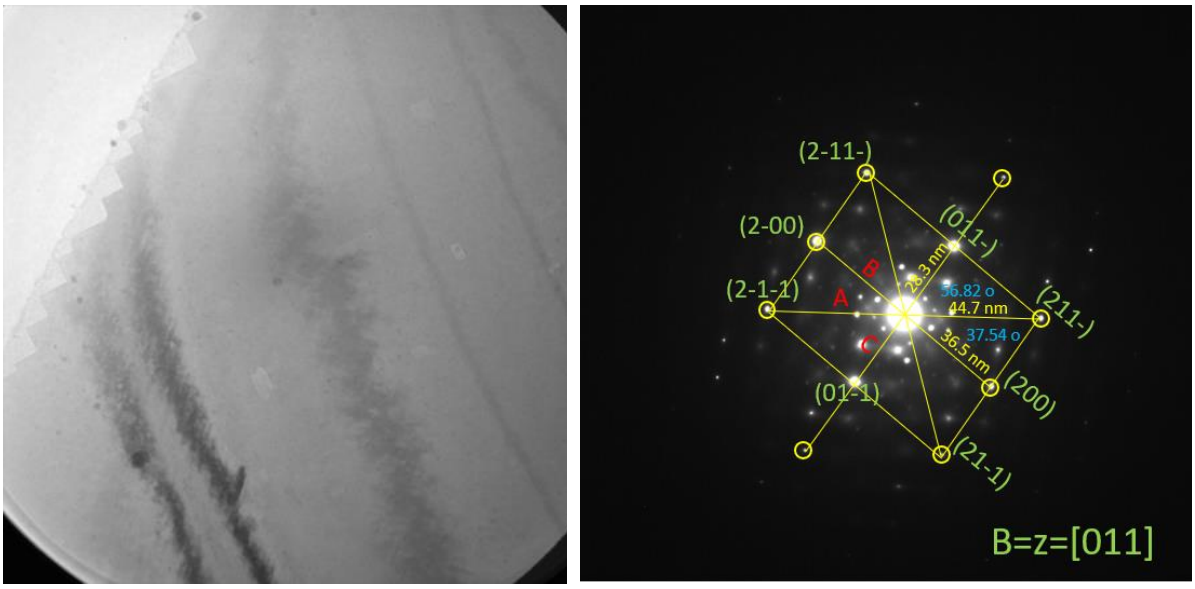

Fig. 5.3.7 Wide view image of the specimen before irradiation with corresponding diffraction pattern.

Table 5.3.1 Diffraction pattern analysis of the 12Cr-ODS steel specimen

Experimental		Experimental		Textbook	
A	44.7	A/C	1.580	A/C	1.732
B	36.5	B/C	1.290	B/C	1.414
C	28.3	angle AB	37.54	angle AB	35.26
		angle AC	56.82	angle AC	54.74

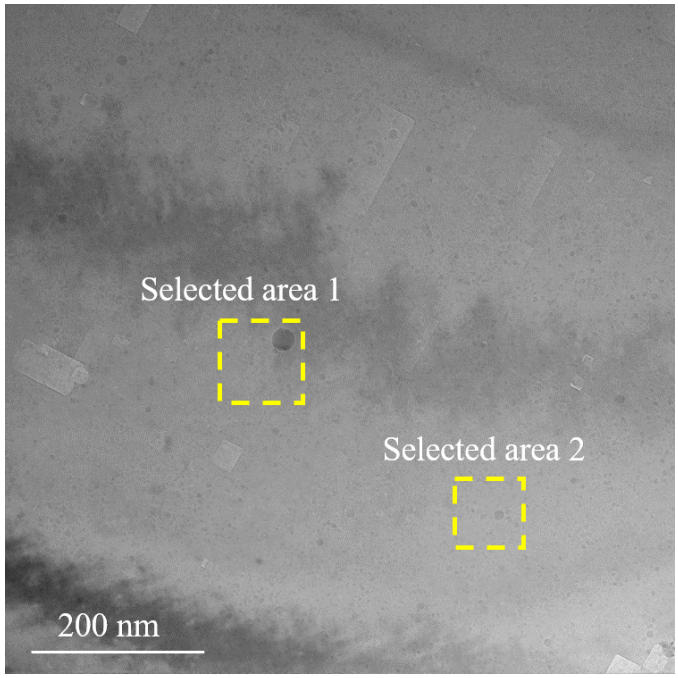

Fig. 5.3.8 Two different areas are selected to closely investigate the microstructural evolution under the uniform irradiation at 823K.

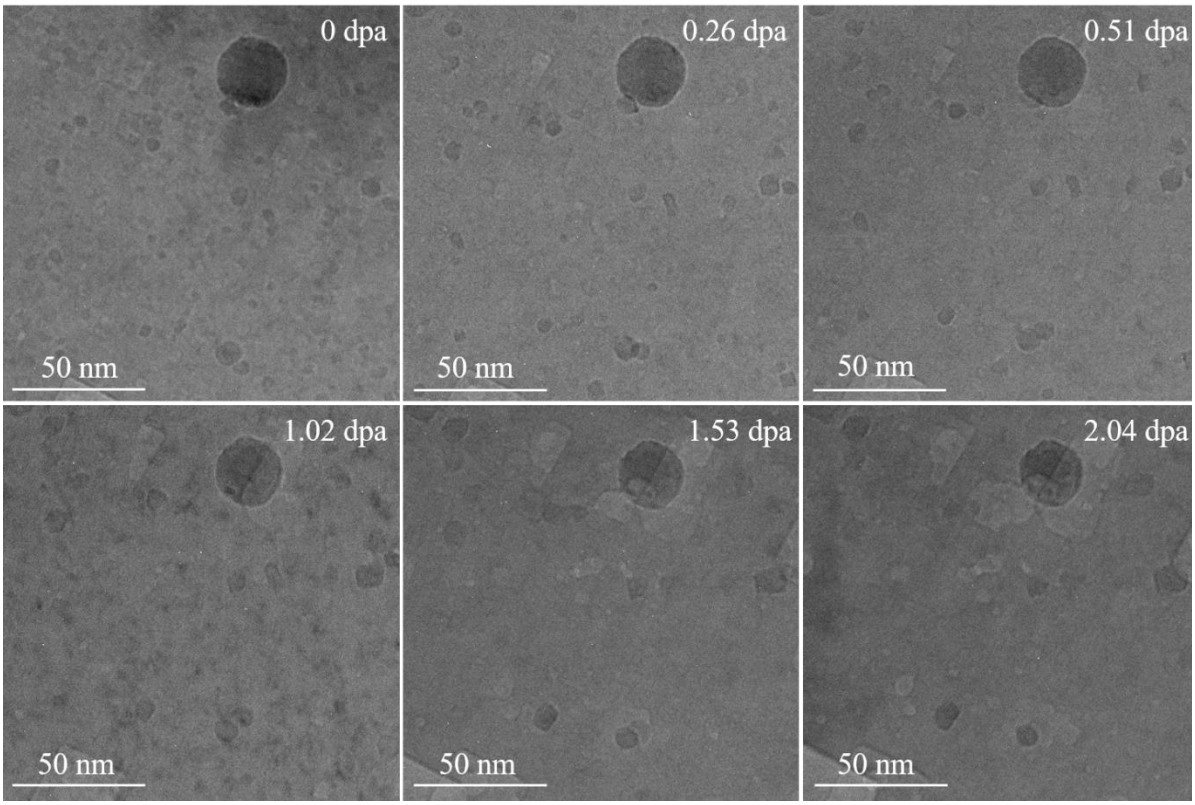

Fig. 5.3.9 Microstructural evolution of SA 1 under the uniform electron beam irradiation of 8.59×10^{-4} dpa/s at 823K.

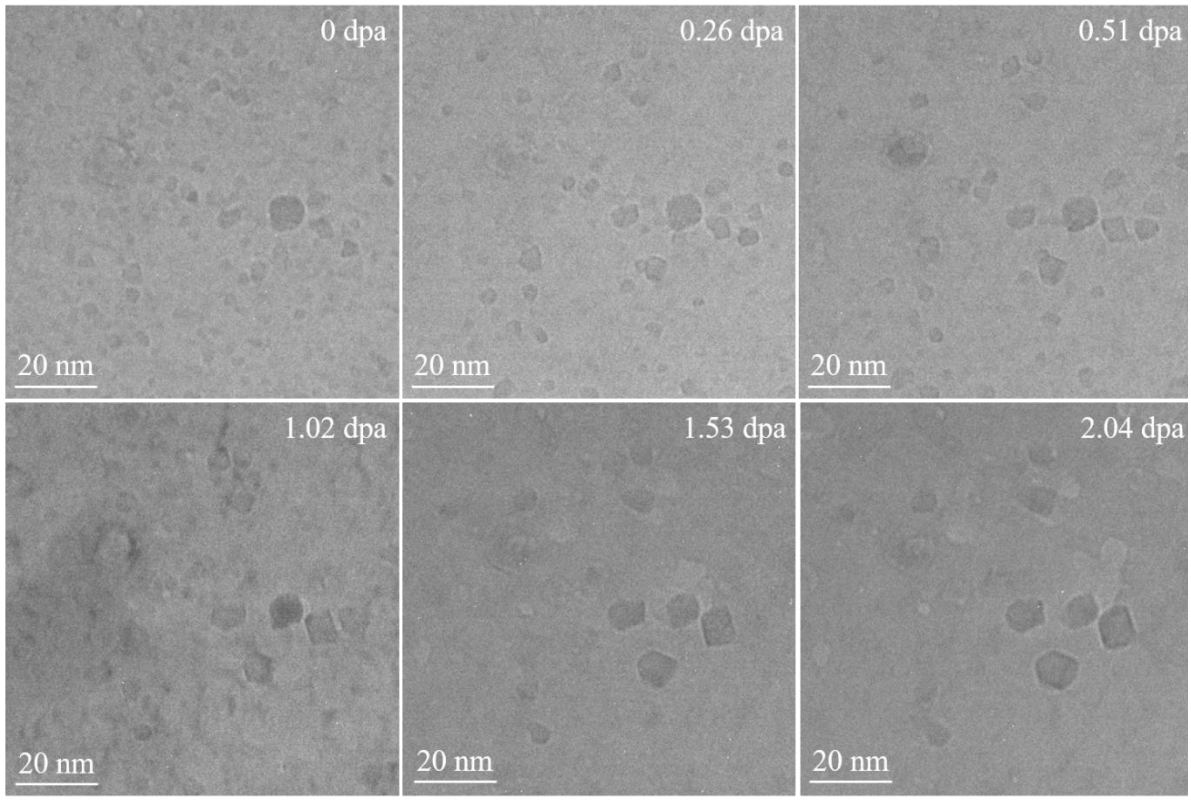

Fig. 5.3.10 Microstructural evolution of SA 2 under the uniform electron beam irradiation of 8.59×10^{-4} dpa/s at 823K.

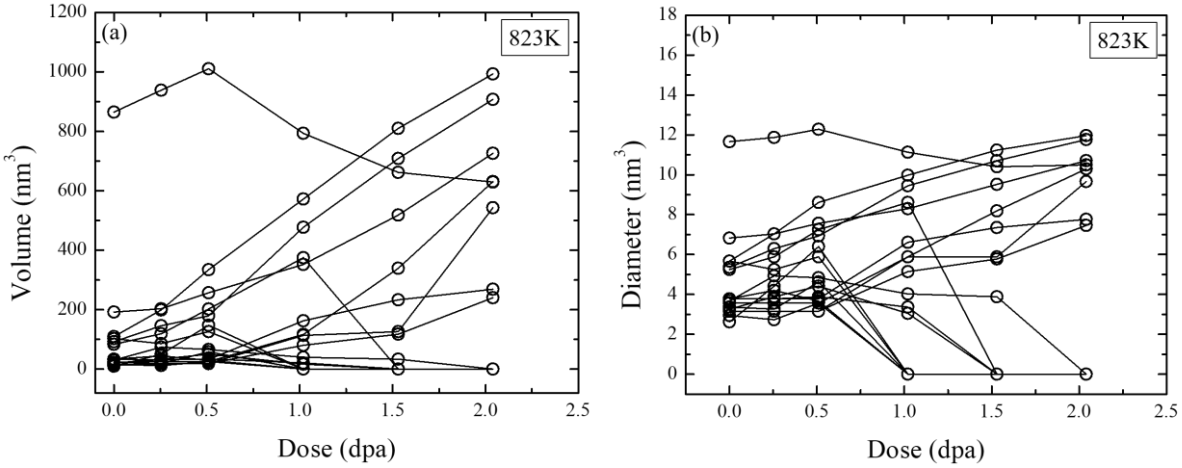

Fig. 5.3.11 Size evolution of nanoparticles during 2 MeV irradiation at 823K represented by (a) volume and (b) equivalent diameter.

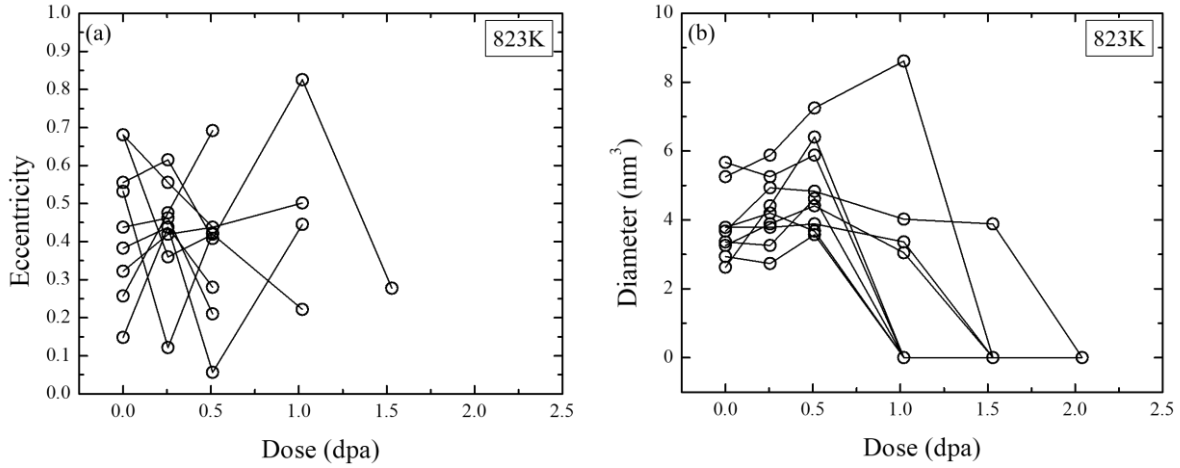

Fig. 5.3.12 Shape and size evolution of disappeared nanoparticles during 2 MeV irradiation at 823K represented by (a) eccentricity and (b) equivalent diameter.

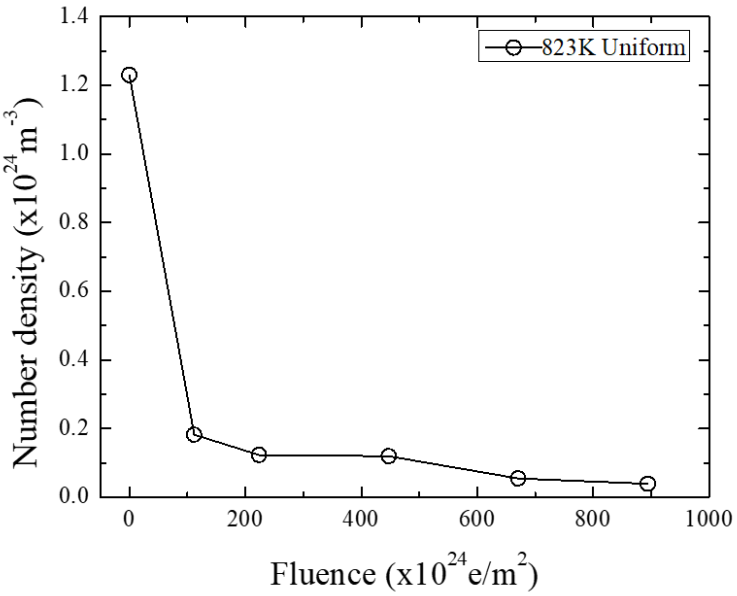

Fig. 5.3.13 Particle number density respect to fluence under the uniform beam irradiation at 823K.

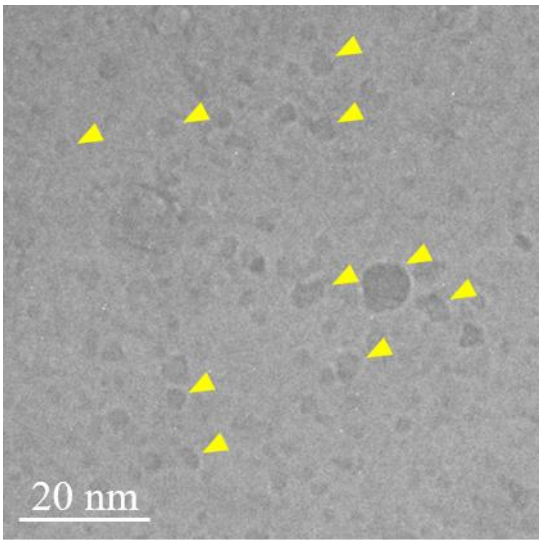

Fig. 5.3.14 The nanoparticles (marked with yellow arrows) at SA 2 which undergo growth and coarsening till the end of the irradiation.

As shown in Fig. 5.3.9 and 5.3.10, regardless of the initial population of nanoparticles, the significant decrease in the nanoparticle number density is observed. Also, the growth of few nanoparticles along with the irradiation at 823K is clearly found. Interesting part is that

under the irradiation, the initial large nanoparticles which are diameter larger than 10 nm were found to shrink under the irradiation while other smaller nanoparticles grew. Based on Fig.5.3.11, the large nanoparticle which is quite isolated from other small nanoparticles undergone shrinkage. Also, in Fig, 5.3.12, the large nanoparticle which is closely situated with neighboring small nanoparticles also shrank under the irradiation. This could once again support the idea that certain nanoparticles composition could vary based on their initial size.

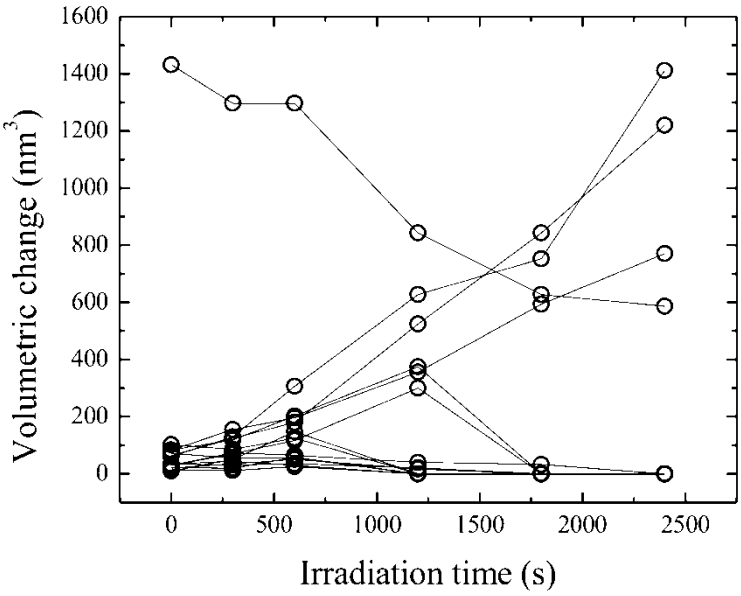

Fig. 5.3.15 Nanoparticles volumetric change respect to irradiation time under the uniform beam irradiation at 823K.

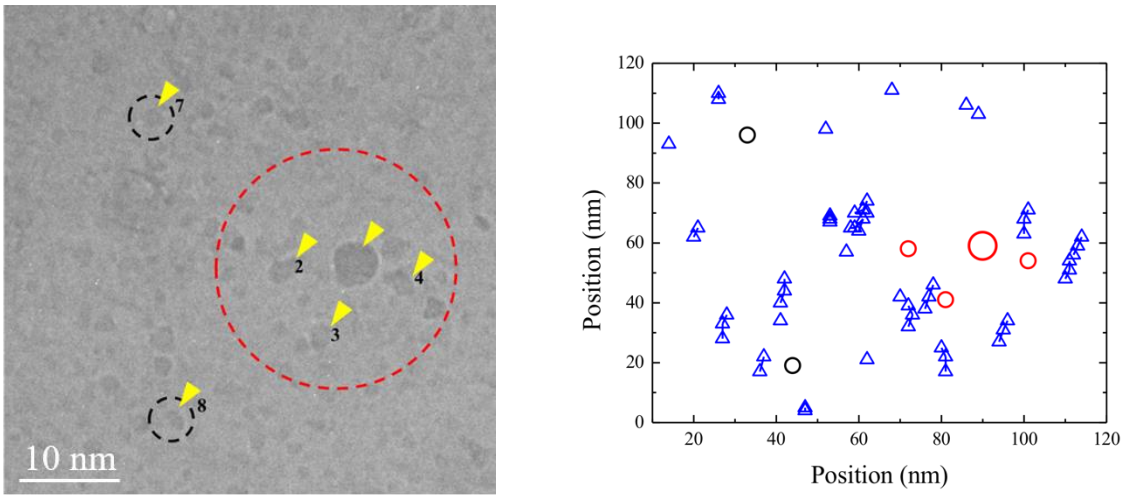

Fig. 5.3.16 Nanoparticles movement under 2 MeV irradiation at 823K.

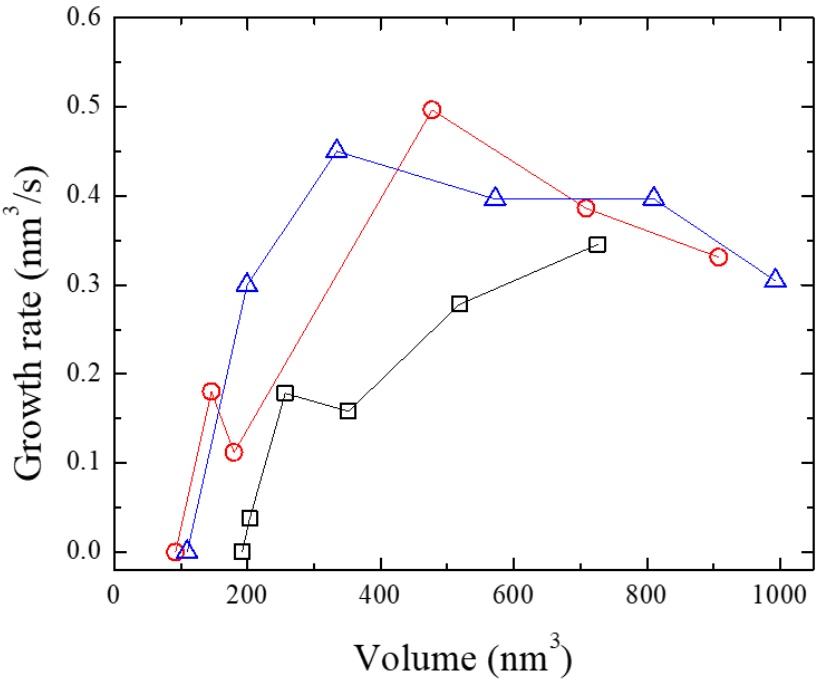

Fig. 5.3.17 Growth rate of the three nanoparticles in a clustered region under uniform irradiation at 823K. The nanoparticles correspond to yellow marked nanoparticles (2, 3, 4) in Fig. 5.3.14.

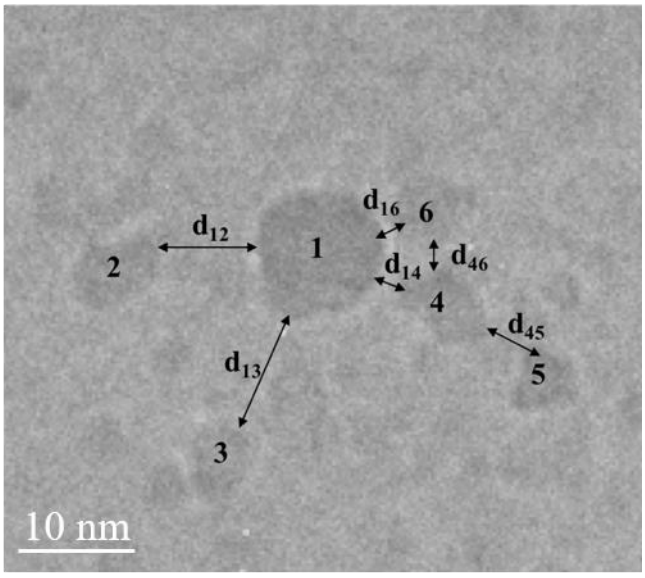

Fig. 5.3.18 Numbering of nanoparticles and their neighboring distance in the clustered region where significant growth occurs.

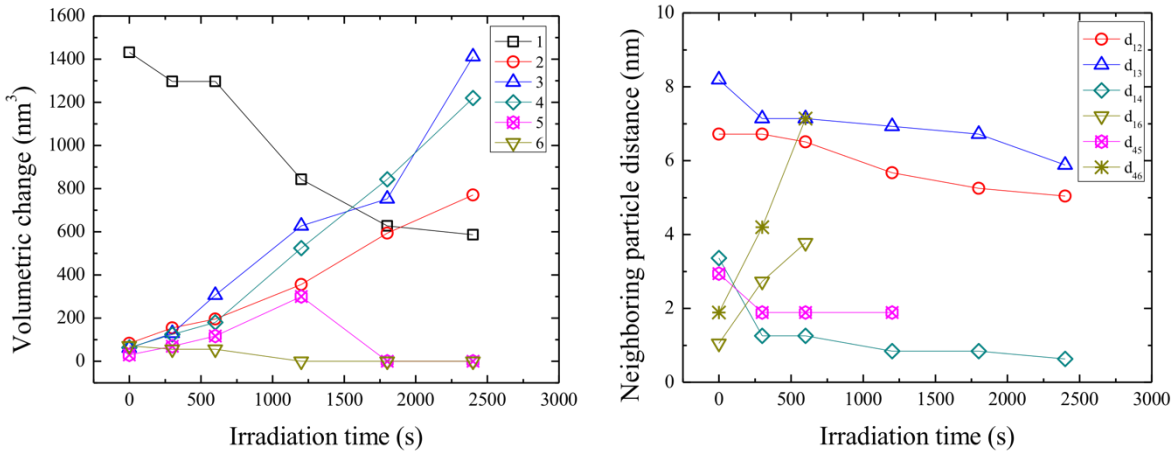

Fig. 5.3.19 Changes in volume of nanoparticles and neighboring particle distance respect to irradiation time in the clustered region which corresponds to Fig. 5.3.18.

Through the observation of the growing nanoparticles, the growth occurred only in a clustered region. In this study, the clustered region is defined as the neighboring nanoparticles being situated within 5 nm to each other. Fig. 5.3.16 and Fig. 5.3.17 represent the clustered region where dominant particle growth has occurred. The nanoparticle grew in clustered region while the shrinkage occurs in isolated/dispersed region which the neighboring nanoparticle distance far exceeds 5 nm. The growth rate of three nanoparticles situated in the clustered region is plotted in Fig. 5.3.15.

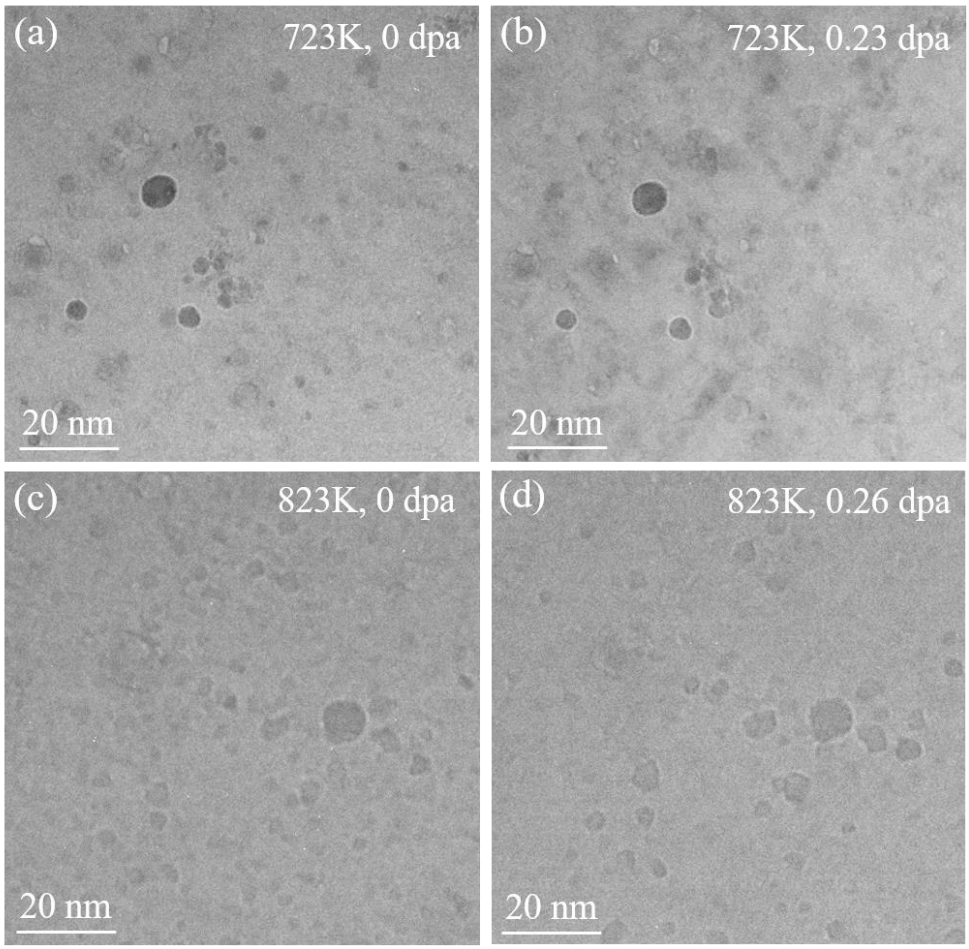

Fig. 5.3.20 Comparison of uniform beam irradiation of the 12Cr-ODS steel under different temperature conditions. (a) before irradiation at 723K, (b) after irradiation at 723K, (c) before irradiation at 823K and (d) after irradiation at 823K.

The two different irradiation temperature conditions but with similar dose are compared. The number density in both experimental cases drops significantly. From Fig. 5.3.18, particle number density between the two different irradiation experiment can be clearly shown. For the 2 MeV uniform beam irradiation at 723K, the particle number density was $1.3 \times 10^{23}\,m^{-3}$ prior to irradiation; while for the 2 MeV uniform beam irradiation at 823K, $1.23 \times 10^{24}\,m^{-3}$.

However, while at 723K only the shrinkage and/or disappearance of nanoparticles are found, at 823K the clear nanoparticles growth at few nucleation sites is observed. This could indicate that there could exist a temperature threshold where governing diffusion kinetic starts to differ. Also, under the uniform irradiation at 723K, the nanoparticles volumetric change was

observed to be non-periodic or stochastic. However, in case of the uniform irradiation at 823K, the nanoparticles either grew or disappeared under the irradiation. This growth or shrinkage which eventually leads to disappearance was periodic.

5.4 Discussion

In terms of the different chemical compositions of the nanoparticles and the matrix, the growth of the nanoparticle requires long-range diffusion of solute atoms to the precipitate-matrix interface and to the transfer of solute atoms across the interface. For the different phases of nanoparticle and matrix, the growth of nanoparticle can only occur if diffusion can transport the solute atoms toward the interface. If the solute atoms can readily transfer across the interface, then the growth rate of the nanoparticle will be governed by the diffusion rate of solute atoms. This process is called diffusion-controlled growth.

However, if the solute atoms cannot readily cross the interface, the growth rate will then be governed by the interface kinetics which is called interface-controlled growth.
When the diffusion process and interface reaction occur at similar rates, then the migration of the interface will be mixed controlled. Based on this volume diffusion-controlled coarsening equation, the equilibrium solid solubility and solid-sate diffusivity of the solute element, and the interfacial energy between the nanoparticle and the matrix phase controls the coarsening of nanoparticles.

To achieve low coarsening rates of nanoparticles at elevated temperatures, alloying elements should have low equilibrium solid solubility and low solid-state diffusivity in the matrix phase and the dispersed nanoparticles should preferably be coherent with the matrix. Also, the dispersed nanoparticles for strengthening mechanism should be intrinsically stable at elevated temperatures.

A low interfacial energy between precipitate phases and the matrix phase is critical for achieving low coarsening rates and for homogeneous solid-state precipitation of the nanoparticles.

At elevated temperatures ($T > 0.5T_m$), in terms of deformation, dislocation gliding is not the dominant mechanism. Typically, based on the applied stress and the temperature, the plastic deformation of alloys occurs primarily by mechanisms of dislocation climb, grain boundary sliding or vacancy diffusion. However, for a large volume fraction of thermally stable nanoparticles within the grains and at grain boundaries, it can provide resistance to steady-state creep at elevated temperatures which enhances the strength of the alloys.

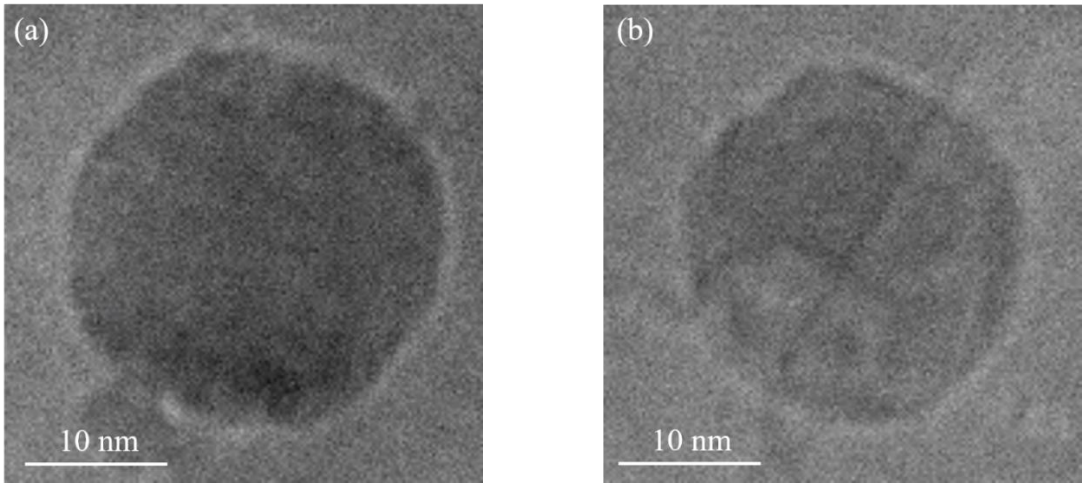

Fig. 5.3.21 The shrinkage of initial large nanoparticle in selected area 1 after the irradiation of 2.04 dpa at 823K.

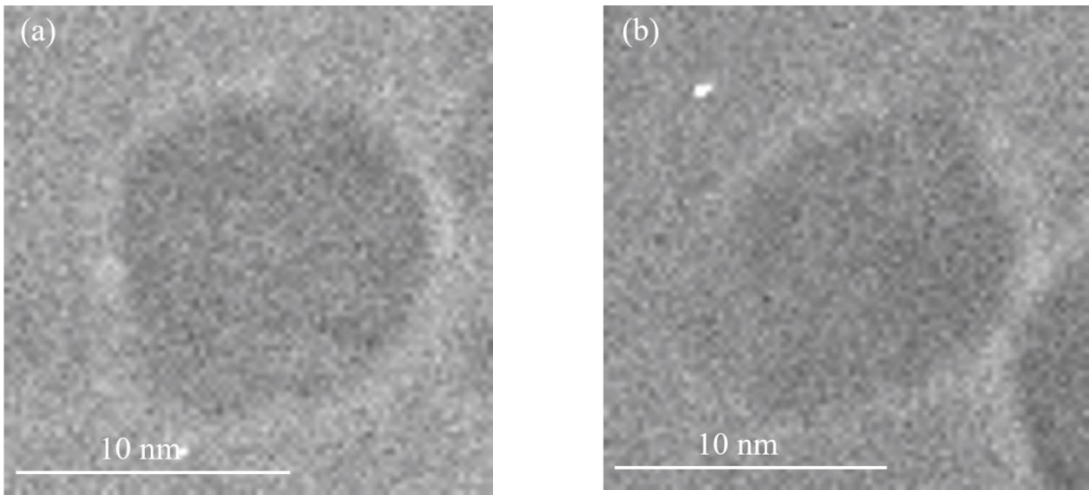

Fig. 5.3.22 The shrinkage of initial large nanoparticle in selected area 2 after the irradiation of 2.04 dpa at 823K.

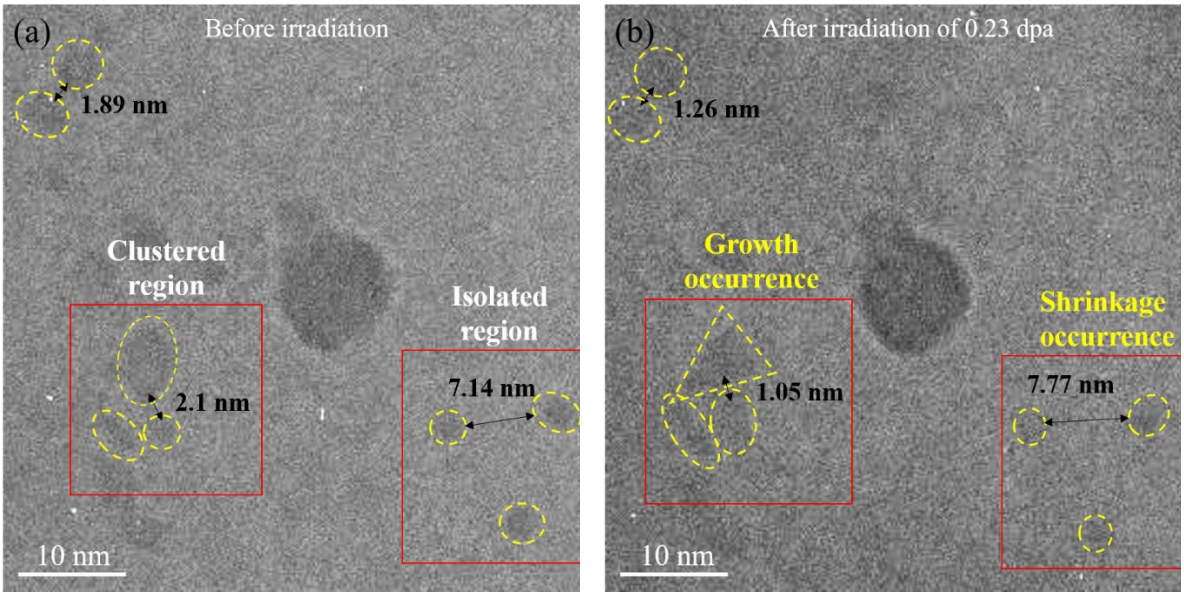

Fig. 5.3.23 Microstructure investigation under uniform irradiation at 723K (a) before irradiation and (b) after irradiation of 0.23 dpa.

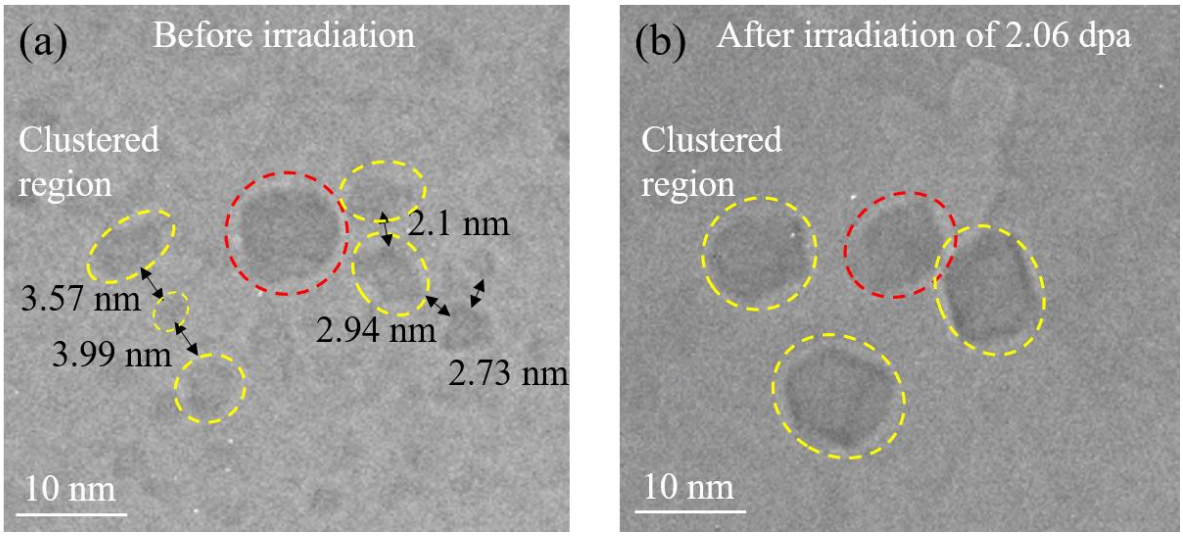

Fig. 5.3.24 Microstructure investigation under uniform irradiation at 823K (a) before irradiation and (b) after irradiation of 2.06 dpa.

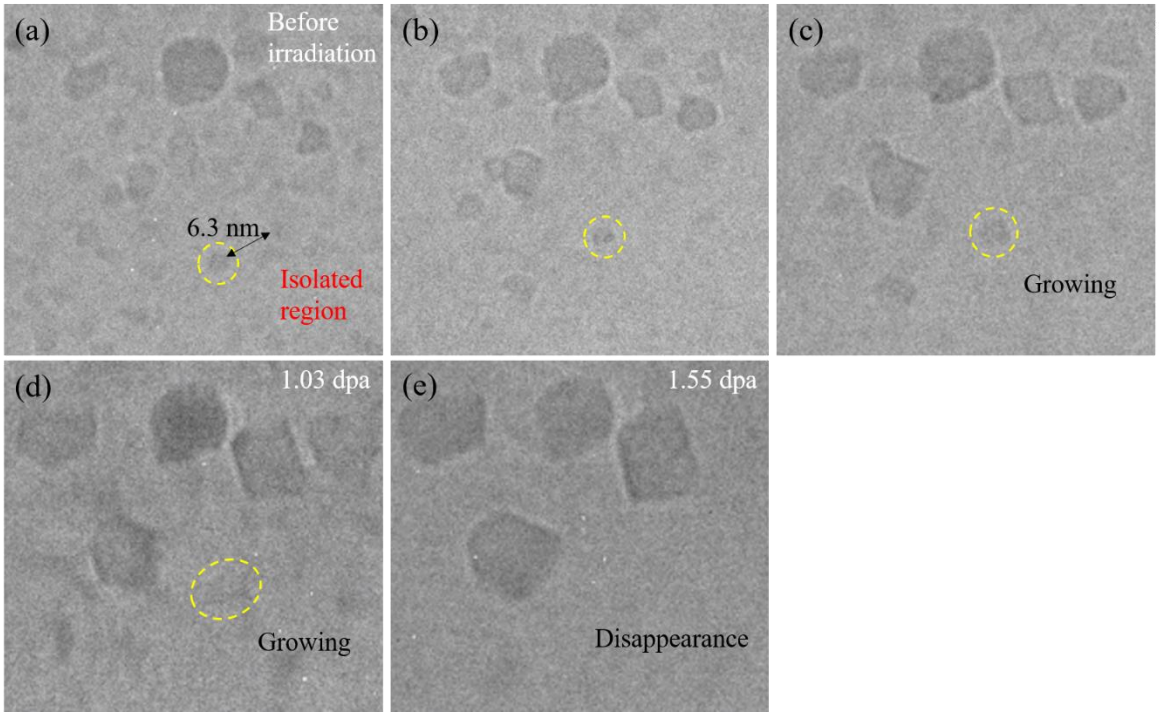

Fig. 5.3.25 Microstructural evolutions of a particle in isolated region under uniform irradiation at 823K.

Through the observation of the growing nanoparticles, the growth occurred only in a clustered region. In this study, the clustered region is defined as the neighboring nanoparticles being situated within 5 nm to each other. Both Fig. 5.3.18 and 5.3.19 support the nanoparticle growth in clustered region while the shrinkage occurs in isolated/dispersed region which the neighboring nanoparticle distance far exceeds 5 nm. The growth rate of three nanoparticles situated in the clustered region is plotted in Fig. 5.3.20.

However, other interesting phenomenon is also observed from the time-sequential images as shown in Fig. 5.3.21. In the isolated region, the nanoparticle was growing up till 1.03 dpa and then disappeared at 1.55 dpa. This similar behavior of nanoparticle undergoing growth and sudden disappearance was quite prevalent in this uniform irradiation at 823K.

5.4.1 Radiation-Enhanced Diffusion

To further understand the above results for rapid stochastic volumetric fluctuation at early irradiation but with no total volumetric change of nanoparticles, diffusion of vacancy and interstitial atoms under the irradiation condition was calculated. Electron energy higher than 1 MeV can cause atomic displacements in the iron matrix and this can result in a flow of vacancies [31,43]. This experiment was a thin foil case and the concentration of interstitials rapidly reaches a steady state as the production rate is matched by the escape rate to the surface The loss of interstitials to sinks and interstitial loops occurs. Also, in the case of high vacancy mobility (high temperature), the vacancy-interstitial mutual annihilation reaction due to the motion of vacancies becomes effective when the vacancies accumulate in the matrix. As the kinetic equilibrium of the nanoparticles can lead to the microstructure evolution, the radiation-enhanced diffusion coefficients of yttrium and titanium which are the constituent atoms of the nanoparticles are calculated and compared at 723K.

Under the uniform beam condition, electron irradiations were performed with a point defect production rate (R) of 1.72×10^{-4} dpa/s. The vacancy diffusion coefficient is defined as:

$$D_v = \alpha v b^2 e^{\left(-\frac{E_v^M}{k_B T}\right)} \tag{5.4.1}$$

where geometric factor α equals 1, υ of Debye frequency is 10^{13} s^{-1}, lattice parameter b for bcc iron is 0.287 nm and vacancy migration energy E_v^M of 0.7 eV [39].

The characteristic time for vacancies to reach the sinks can be expressed as

$$\tau = (k^2 D_v)^{-1} = 1.602 \times 10^{-4}\ \text{s} \tag{5.4.2}$$

Under the assumption that the nanoparticles are the perfect sinks for point defects, the sink strength k^2 is calculated as 5.71×10^{15} m^{-2} where the TEM measured nanoparticles mean diameter and density were 3.5 nm and 1.3×10^{23} m^{-3} [47]. Then the steady-state non-equilibrium vacancy concentration is calculated by $C_v^{Irr} = R\tau$.

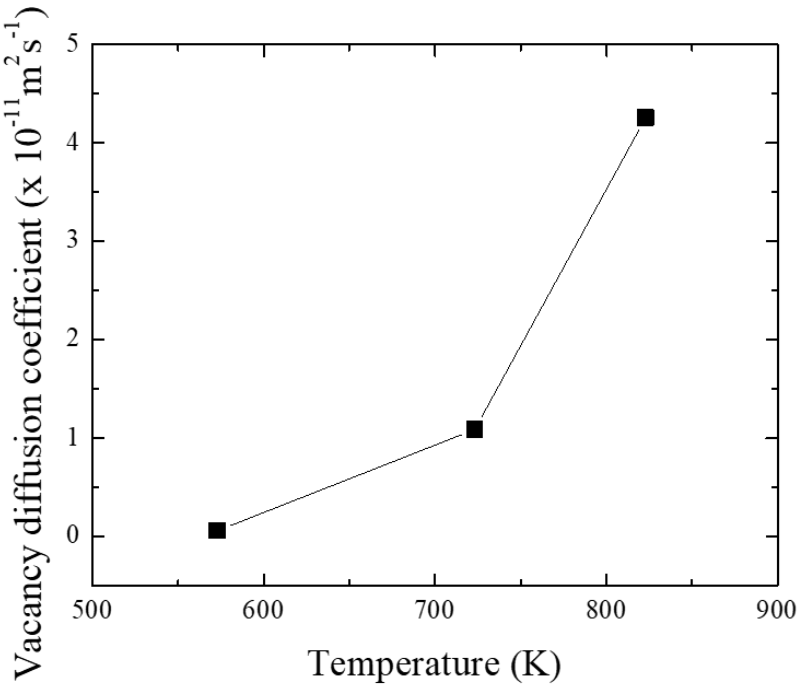

Fig. 5.4.1 Vacancy diffusion coefficient for the experimental conditions at 573, 723, and 823K.

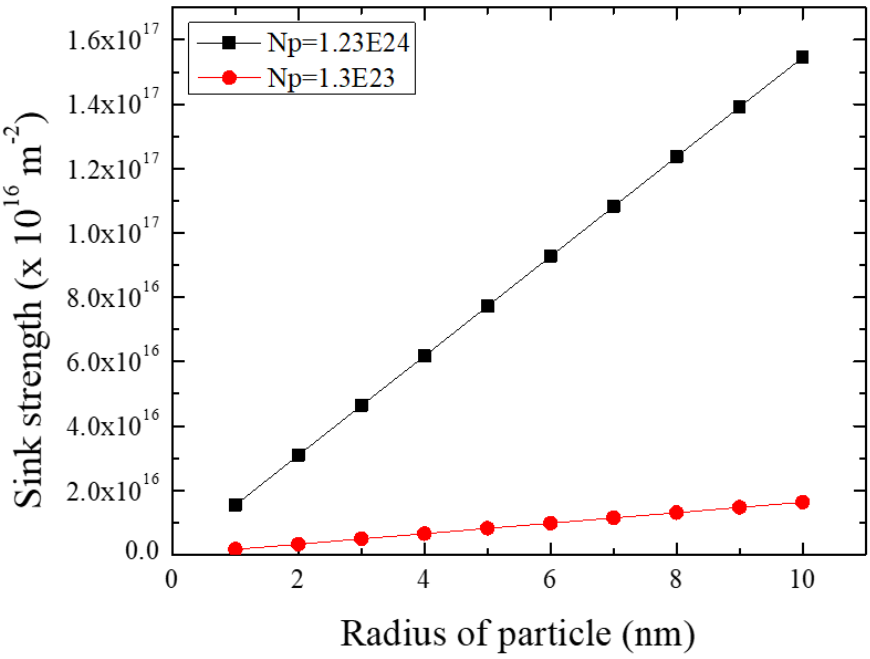

Fig. 5.4.2 Sink strength for two different particle number density respect to radius of particle.

Finally, the radiation-enhanced diffusion coefficient is defined as:

$$D^{Irr} = \frac{C_v^{Irr}}{C_v^{eq}} \times D^{th} = R\tau \times e^{\left(\frac{E_v^f}{k_B T}\right)} D^{th} \quad (5.4.3)$$

with the vacancy formation energy of E_v^f = 2.2 eV [48]. The thermal diffusion coefficients for both Y and Ti elements in pure iron with bcc structure are calculated [37,49]:

$$D_Y^{th} = (1 \times 10^{-5}) e^{\left(-\frac{3.25\ eV}{kT}\right)} \quad (5.4.4)$$

$$D_{Ti}^{th} = 0.21 \times e^{\left(-\frac{293.2 \pm 8.8\ kJ\ mol^{-1}}{RT}(1+0.079M^2(T))\right)} \quad (5.4.5)$$

D_Y^{th} = 2.24 × 10^{-28} m^2s^{-1} and D_{Ti}^{th} = 1.17 × 10^{-23} m^2s^{-1}. For the titanium element diffusion in iron, the magnetization factor M(T=723K) ~ 0.8 is used [50]. The radiation-enhanced diffusion coefficient of the elements under 723K irradiation, D_Y^{Irr} and D_{Ti}^{Irr} are calculated as 1.32 × 10^{-20} m^2s^{-1} and 2.58 × 10^{-14} m^2s^{-1}, respectively. Based on this diffusion coefficient of Y and Ti elements under electron irradiation at elevated temperature, the radiation-enhanced diffusion phenomena can be dominated Ti element rather than Y in iron matrix [51].

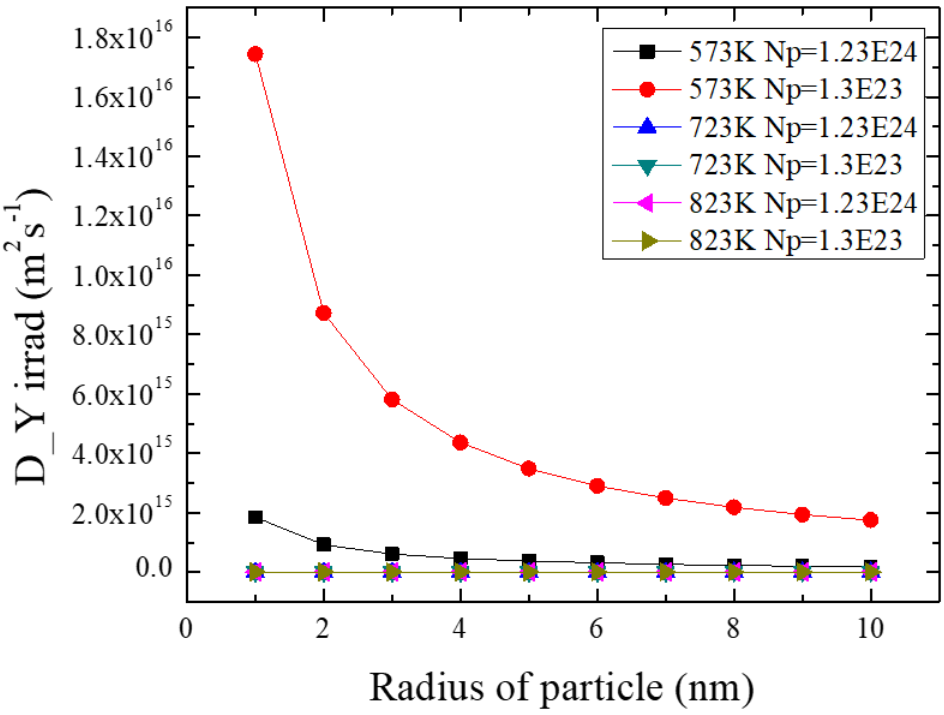

Fig. 5.4.3 Radiation-enhanced diffusion coefficient for yttrium under various experimental conditions respect to radius of particle.

However, apart from these disappeared nanoparticles, under both the focused and uniform beam conditions, rest of the survived nanoparticles presented stochastic size change behavior under the flux 1.6×10^{23} e/m^{2}s while above this flux region the nanoparticles did not undergo any size change. From the analysis of time sequential TEM images, unlike the typically reported monotonic size change behavior of nanoparticles, the nanoparticles exhibited stochastic size fluctuation behavior in each different irradiation time step. However, regardless of this stochastic size fluctuation under different time irradiation, there was no total volumetric change of nanoparticles. This stochastic phenomenon did not follow Ostwald ripening and could rather be interpreted as the radiation enhanced diffusion attributing to the volumetric change of nanoparticles with the effect of vacancy concentration gradient.

The nanoparticle dissolution could also be due to created vacancies in the matrix under irradiation. The diffusion of vacancy and interstitial atoms under the irradiation condition was calculated and found that radiation enhanced diffusion phenomena can be dominated by Ti element rather than Y in iron matrix. The radiation-enhanced diffusion can create the particle-matrix interface instability that lowers the chemical potential barrier for possible Ti dissolution. However, the diffusion length of Ti was extremely short and diffusion of these elements under short time irradiation is unlikely. Rather, the concentration and mobility of vacancies could be dominant factor in describing this stochastic size fluctuation behavior. This stochastic volumetric change could be related with the quasi-state of nanoparticles.

5.4.2 Radiation-Induced Growth

Radiation-induced growth is typically explained by Ostwald ripening which is the process by which larger particles grow at the expense of smaller ones. This process is a direct consequence of the Kelvin effect, which is the higher solubility of small particles [52].

$$C(a) = C(\infty)e^{(\frac{\alpha}{a})} \tag{5.4.6}$$

where C(a) is the solubility of a dispersed phase particle with radius a and C(∞) is the bulk solubility. α is called the capillary length and is defined by

$$\alpha = \frac{2\gamma V_m}{RT} \tag{5.4.7}$$

where V_m is the molar volume of the dispersed phase, γ is the interfacial tension, R is the universal gas constant, and T is the absolute temperature. Based on the above equation, small particles are more soluble than large particles. Thus, small particles could tend to lose their molecules and these molecules diffuse through the continuous phase and reprecipitate onto larger particles. This leads to an increase of average particle size with time.

Ostwald ripening in a two-phase system is given by the Lifshitz-Slyozof-Wagner (LSW) theory. This LSW theory is based on the following four assumptions [11]:

(1) The particles are fixed in space.

(2) The system is infinitely dilute (implying the absence of interparticle interactions).

(3) The concentration of internal phase molecules is the same throughout the whole external phase, except in the direct neighborhood of the particles (a peal with radii a and 2a, where a is the particle radius).

(4) Single internal phase molecules are transported by molecular diffusion from one particle to another.

With these above assumptions and by using Fick's first law, the mass balance, and the continuity equation for the particle size distribution, the following major results are derived:

1. At any instant of the ripening process, there exists a critical radius a_c. Particles with a larger radius grow, and smaller particles shrink. If the radius equals a_c, the size of the particle does not change. During the ripening process, a_c increases with time.

2. The Ostwald ripening rate can be defined as

$$v = \frac{da_N^3}{dt} = \frac{4\alpha D_m C(\infty)}{9} \tag{5.4.8}$$

where D_m is the molecular diffusion coefficient of the internal phase and a_N is the number-average particle radius.

According to the above results, a clear limitation for using the Ostwald ripening to describe the radiation-induced growth phenomenon can be found. During the radiation experiment under the uniform beam at 823K, the growth occurs for specific nanoparticles. However, the important part which should be emphasized is the morphological transformation along with the growth and coarsening behavior of nanoparticles.

The coarsening behavior can be explained that electron irradiation caused the surrounding oxides to decompose and grow into the most energetically favorable nanoparticles (i.e. pyrochlore-type nanoparticle). In addition, the energetically unstable decomposed oxides can diffuse into the matrix.

5.4.3 Morphological Transformation of Non-Stoichiometric Nanoparticles

During the irradiations, the nanoparticles shapes were changed along with their sizes. Under the uniform irradiation at 723K, the small sized nanoparticles became elongated while the larger nanoparticles became spherical. Variation in shape and its corresponding size change during irradiation could be correlated, and a shape factor was considered as an attempt to analyze the nanoparticles response against the irradiation. From the surface energy perspective, the larger sized nanoparticles became more stable while the small nanoparticles became rather unstable under the irradiation. Based on the TEM image of the ODS steel specimen, most nanoparticles were not simple spheres but rather ellipsoids. Both $Y_2Ti_2O_7$ and Y_2TiO_5 are non-stoichiometric nanoparticles and could be defined as a diameter smaller than 15 nm which corresponds to a volume of 1767 nm^3 [25]. In this study, all the targeted nanoparticles were smaller than the volume of 1767 nm^3. Before the irradiation, the nanoparticles that were

embedded in the 12Cr-Fe matrix were stable at 723K. However, upon the short-time interval irradiation, both shrinkage and growth of each nanoparticle were observed simultaneously.

This non-periodic stochastic behavior prevailed for some time and then reached the near steady-state towards the final irradiation state. This result is unlike the Ostwald ripening as there was no net change in the volume of each irradiated nanoparticles. Rather this stochastic volumetric fluctuation throughout the short-time irradiation intervals could be interpreted as the dissolution of nanoparticles. As the nanoparticles in the specific $Y_2Ti_2O_7$ and Y_2TiO_5 structure were reported to be non-stoichiometric, the rapid fluctuation of volume in the early irradiation without the total volumetric change could be explained as the dissolution till they reach energetically stable state.

Apart from the 723K uniform irradiation result, under the uniform irradiation at 823K, the growth of nanoparticles was observed along with their shape evolutions. From observing the shape evolution of growing nanoparticles, the final shapes of nanoparticles are either cuboid or five-sided polygon. Not all the nanoparticles under the irradiation undergo growth but only few. Also, the initial large nanoparticles size decrease is observed.

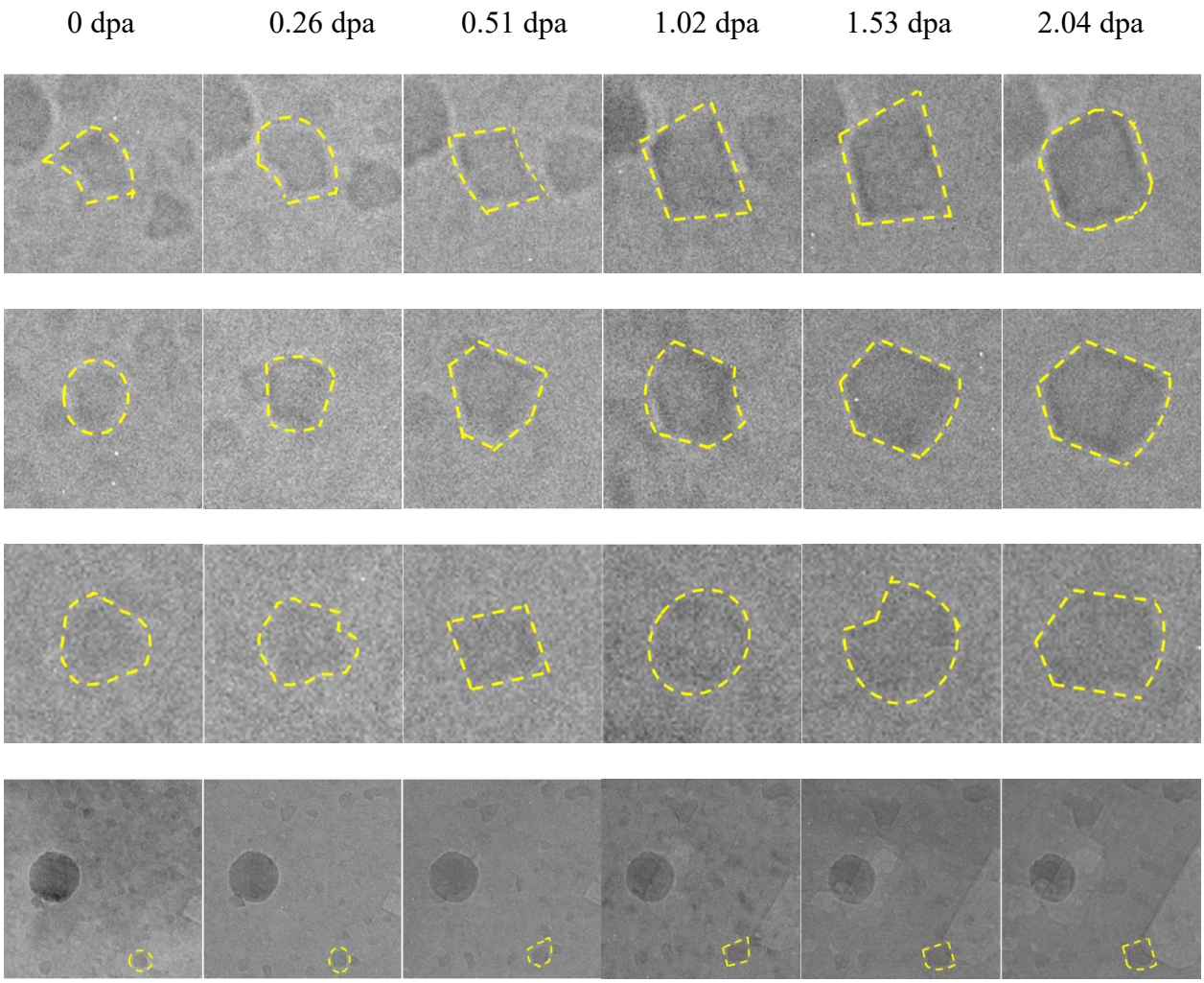

Fig. 5.4.1 Growth and shape evolutions of nanoparticles under the uniform irradiation at 823K.

The equilibrium shape of coherent precipitate is controlled by the balance between interfacial energy and elastic strain energy. In terms of coherent nanoparticles, the equilibrium shape of a coherent nanoparticle can only be predicted from the γ-plot (interfacial free energy) when the misfit is small between the nanoparticle and the matrix. When there is misfit, the formation of coherent interfaces increases the free energy of the system due to the increase in elastic strain fields.

Coherency of nanoparticle

If the total interface energy is $\sum S_i\gamma_i$ and the elastic strain energy is ΔG_s, the equilibrium shape becomes spherical which has a minimum surface energy [54].

$$\sum S_i \gamma_i + \Delta G_s = \text{minimum} \quad (5.4.9)$$

The stresses which maintain coherency at the interface distort the nanoparticle lattice, and for a spherical nanoparticle case, the distortion is isotropic. Depending on a shape of nanoparticle, misfit differs. For a thin disc shape nanoparticle, the in situ misfit is no longer equal uniaxially. Instead, the misfit is perpendicular to the disc and nearly zero in the plane of the broad faces.

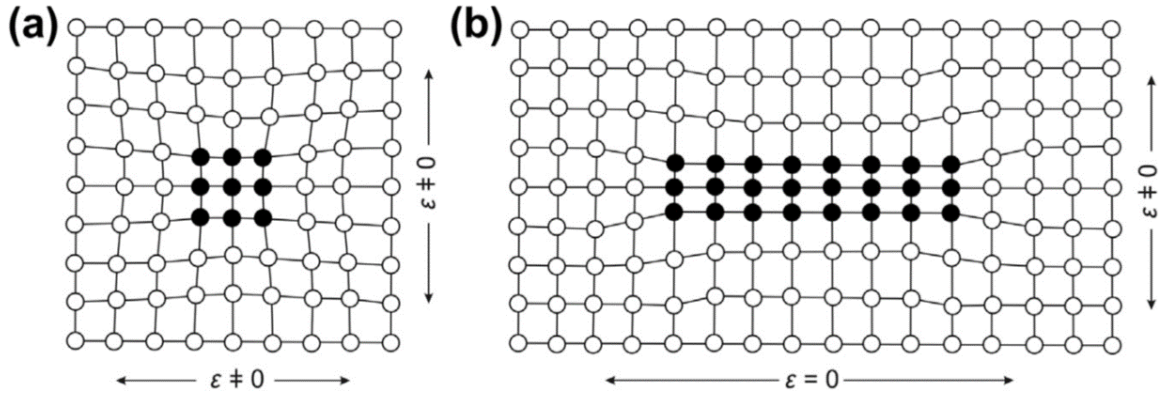

Fig. 5.4.2 Misfit between coherent precipitate and surrounding matrix. (a) Spherical particle and (b) plate-shaped particle [55].

The total elastic energy depends on the shape and elastic properties of both nanoparticle and matrix. The total elastic strain energy can be given by

$$\Delta G_s \approx 9 G_\varepsilon^2 V \quad (5.4.10)$$

where the shear modulus of the nanoparticle and matrix being G, the constrained misfit between the nanoparticle and the matrix being ε, and the volume of the unconstrained hole in the matrix being V. This equation is valid if the matrix is elastically isotropic, the elastic moduli of the matrix and nanoparticle are equal, and Poisson's ratio is 1/3.

Coherency strain produces an elastic strain energy which is proportional to the square of the lattice misfit and increases with the volume of the nanoparticle. If the nanoparticle and matrix have different elastic moduli, the elastic strain energy is no longer shape independent and it becomes minimum for a sphere.

Incoherency of nanoparticles

When the nanoparticle is incoherent with the matrix, there is no coherency strain. However, the misfit strain can still occur if the volume of the nanoparticle differs from the original matrix before the formation of the embedded nanoparticles.

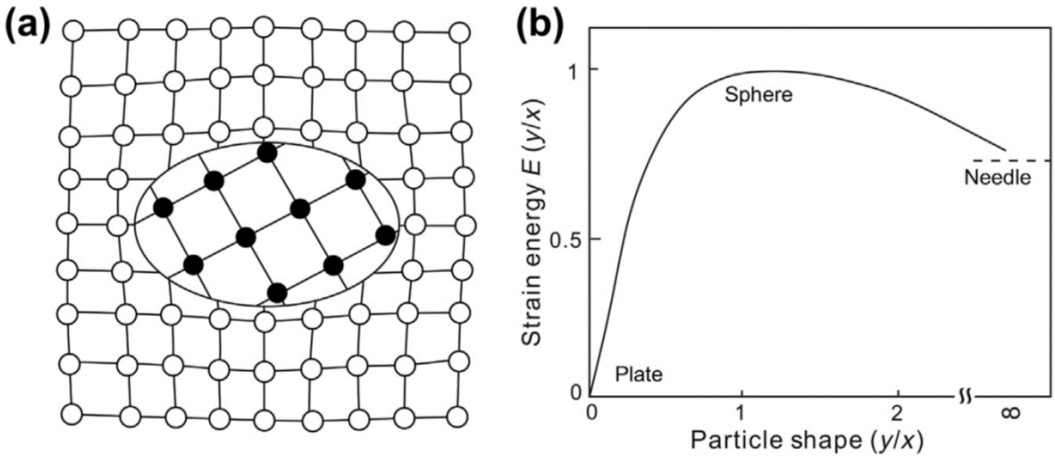

Fig. 5.4.3 (a) Misfit strain with an incoherent nanoparticle with matrix and (b) variation of the misfit energy associated with an incoherent nanoparticle with its shape [55].

The lattice misfit can be replaced by the volume misfit and can be represented as

$$\Delta = \frac{V_m - V_n}{V_m} \tag{5.4.11}$$

where V_n being the volume of the unconstrained hole in the matrix, and V_m being the volume of the unconstrained nanoparticle. When the matrix hole and nanoparticle are constrained to occupy the same volume, the elastic strain field occurs as shown in Fig 5.4.2. For a homogeneous incompressible ellipsoidal shaped nanoparticle in an isotropic matrix, the elastic strain energy is

$$\Delta G_s = \frac{2\mu(V_m - V_n)^2}{3V_m} E\left(\frac{y}{x}\right) = \frac{2}{3} G\Delta^2 V_m E\left(\frac{y}{x}\right) \tag{5.4.12}$$

where x and y are the semi-axes of the ellipsoidal nanoparticle, E(y/x) being the strain energy of the ellipsoidal nanoparticle, and G being the shear modulus of the matrix [56,57].

Morphological transformation during coarsening (for coherent nanoparticle)

Morphological transformations of nanoparticle result in a monotonic decrease of the elastic energy. Transformation from a sphere to a cube and then can decompose into doublet and octet forms. The elastic energy of each cube within an octet of cubes would be decreased by decomposing into sub-cubes. This process can indefinitely occur till the particle size downs to atomic dimensions.

However, the mentioned process is unlikely to occur due to the interfacial energy that increases monotonically as the nanoparticle morphology becomes less compact. While the elastic energy decreases as the shape evolves from sphere to cube and then to doublet to octet, the surface energy increases in the same manner. The preferred morphology should be the one that minimizes the sum of the elastic and the surface energy. Since the surface energy becomes less important as the particle volume increases, the preferred shape of the nanoparticle changes during coarsening through the sequence of possible shapes in order of decreasing elastic energy [58].

Under the assumption that the interfacial tension is isotropic, the preferred shape of a nanoparticle is spherical when its size is small ($a \ll r_o$). To make an easy comparison between a sphere and a cube, if the volume of the sphere be ($2a^3$), its surface area is

$$\mathrm{S} = 4a^2(36\pi)^{1/3} \tag{5.4.13}$$

Then the total energy becomes

$$\Delta\mathrm{F(sphere)} = 0.709E_1(2a)^3 + \sigma(36\pi)^{1/3}(2a)^2 \tag{5.4.14}$$

The relative energy of a cube with the same volume as a sphere,

$$\Delta\mathrm{F(cube)} = 0.558E_1(2a)^3 + 6\sigma(2a)^2 \tag{5.4.15}$$

Transition of a sphere into a cube represents the sphere becomes metastable when

$$0.151E_1(2a) \geq \sigma\left[6 - (36\pi)^{\frac{1}{3}}\right] \tag{5.4.16}$$

This inequality is satisfied when

$$2a \geq 7.7\left(\frac{\sigma}{E_1}\right) = 7.7r_o \qquad (5.4.17)$$

with r_o being the characteristic length of the material and represented as $r_o = \sigma/E_1$.
The size parameter r_o depends on the balance between the interfacial tension, misfit strain, and elastic constant of nanoparticle. It follows that the sphere becomes metastable with respect to transition into a cube when $\Delta F(\text{sphere}) \geq \Delta F(\text{cube})$.

Coarsening of the particles with very small size ($a \ll r_o$) is called interface controlled. The surface tension dominates their energy and they have spherical shape. Also, the LSW theory of coarsening can be applied. The LSW theory makes prediction that the nanoparticles coarsen with a constant size distribution about the mean value. Based on this theory, the elastic energy is unaffected by coarsening and influences the coarsening rate only through its effect on the diffusivity.

Coarsening of the nanoparticles with larger size ($a \gg r_o$) is called strain controlled. The elastic energy predominates over the interfacial contribution and strain-controlled coarsening occurs. The nanoparticles take on cuboidal shape and resist further growth. In some researches it is reported that as the size increases, it decomposes back into smaller nanoparticle and that the individual nanoparticle size remains nearly identical.

The preference for decomposition has its source in elastic anisotropy which introduces an effective elastic repulsion between the elementary sub-volumes of the nanoparticle. A spherical or cubic nanoparticle is held together by interfacial tension. As the nanoparticle coarsens the interfacial contribution to the free energy significantly decreases, and decomposition could be favored.

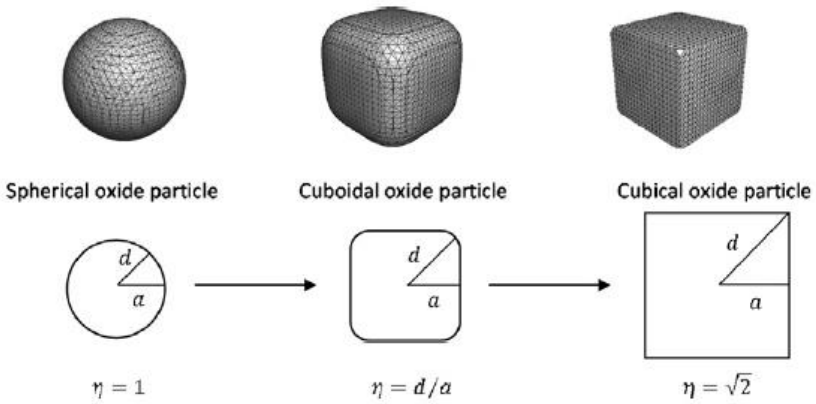

Fig. 5.4.5 Evolution of the parameter η as a function of the shape of the particle [59].

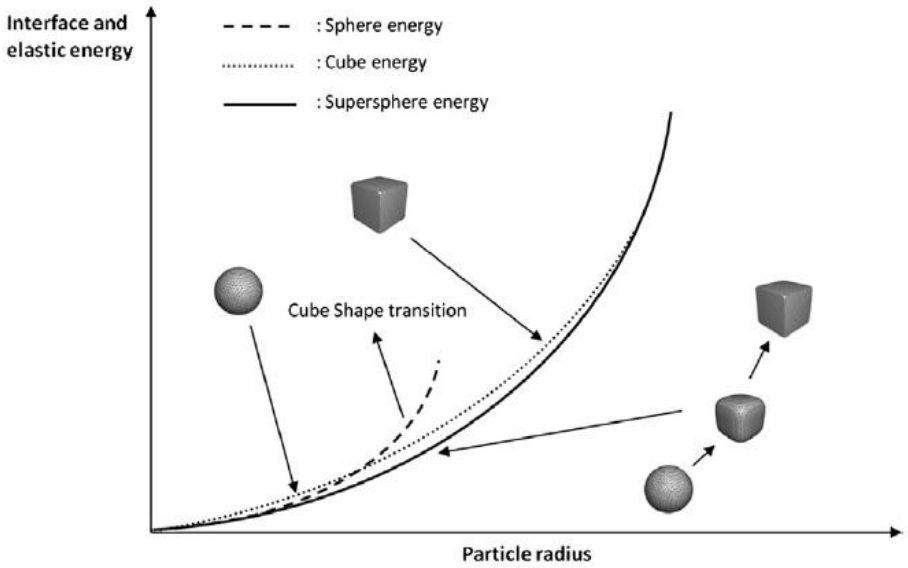

Fig. 5.4.6 Schematic drawing of the evolution of the surface and elastic energy for a spherical, a cubical and a superspherical particle showing the smooth transition shape allowed by using the superspherical equation [59].

The anisotropic elastic interaction and the surface tension allows to predict the effective size when a cube is metastable with respect to decomposition into a pair of parallel plates or an octet of smaller cubes. Using the analysis, the decomposition of cuboidal nanoparticles can be arranged in terms of morphological sequence which governs the shape evolution of a nanoparticle from a sphere to a cube. The shape transitions can be preferred at specific value of radius r_o.

The elastic interaction distance depends on the separation distance. The nanoparticles repel one another when they are close and attract when they are well separated. This coarsening

of elastic nanoparticles phenomenon includes the repulsive interaction opposes their aggregation into large size nanoparticles and at certain size, further coarsening is resisted. Also, the attraction of elastic nanoparticles that are well separated should condensate into groups of neighboring nanoparticles.

The driving force for loss of coherency increases with the misfit parameter ϵ_o. Thus, the nanoparticles are expected to lose coherency with the matrix at increasingly smaller sizes as the misfit parameter increases. The predicted size for the shape evolution from a sphere into a cube should also decrease as the misfit parameter grows. From a thermodynamic perspective, the shape transitions are first order transitions that they may proceed through intermediate states of higher energy and may be kinetically suppressed.

The elastic mismatch between the nanoparticle and matrix is significant and that a distribution of nanoparticles is likely to be at a thermoelastic quasi-equilibrium state where the nanoparticle size coarsens very slowly. Further significant coarsening requires a loss of coherency or a reconfiguration of nanoparticles distribution. The free energy of a solid which contains a distribution of coherent nanoparticles is determined by their size, shape and distribution upon their composition. Due to the elastic interaction, the size, shape and distribution of the nanoparticles are internal thermodynamic parameters whose values constrain the local equilibrium of the system.

CHAPTER 6.

In-Situ 1.25 MeV Electron Irradiation at Elevated Temperature

6.1 Results: Uniform Beam Irradiation at 573K

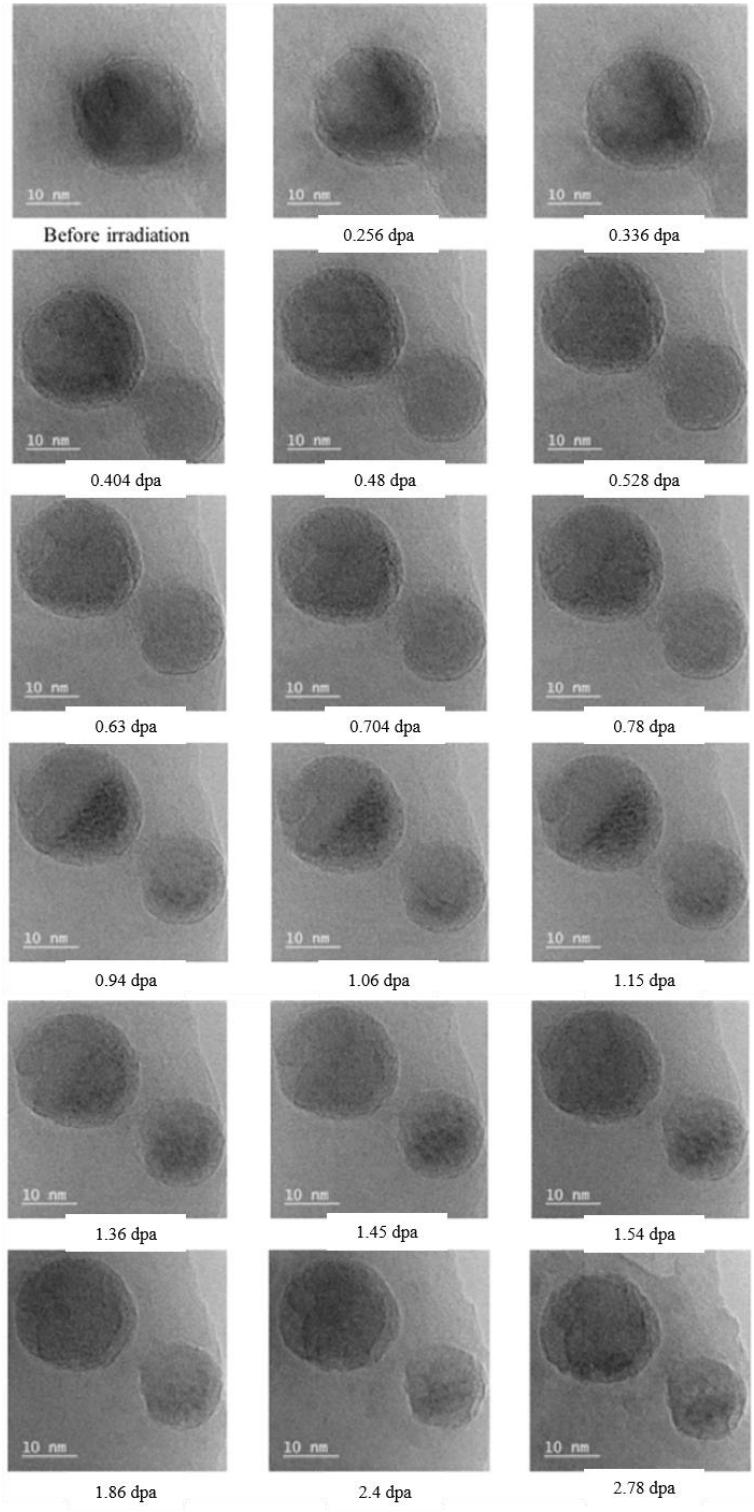

Fig. 6.1.1 In-situ HRTEM images of microstructure evolution under 1.25 MeV electron irradiation.

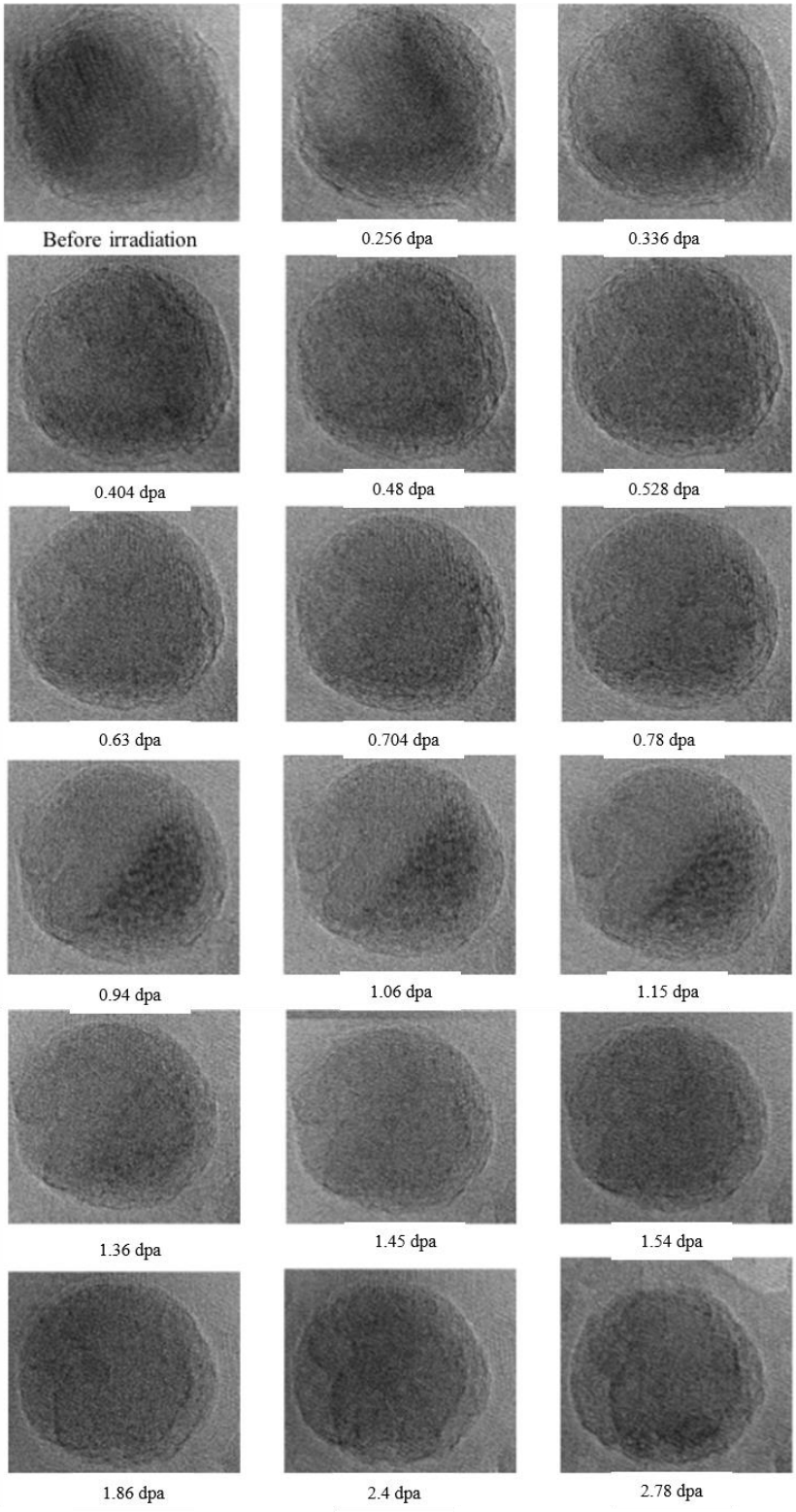

Fig. 6.1.2 Time-sequential HRTEM images of a single particle irradiation under 1.25 MeV at 573K.

For the in-depth study on the particle instability mechanism, a single nanoparticle irradiation is performed under 1.25 MeV at 573K using in-situ HRTEM (JEM-ARM1300) at Hokkaido University. This in-situ HRTEM technique provides high TEM image resolution at 300,000 magnification. For the irradiation experiment, the narrow observation area of 40 nm by 40 nm was selected where there exist two different size nanoparticles. The nanoparticles were located near the edge of the specimen indicating very thin region.

During the in-situ HRTEM electron irradiation, particle dissolution phenomena was observed as shown in Fig. 6.1.1 and 6.1.2. In the beginning of the irradiation, the smaller nanoparticle's surface edge was not clear and difficult to clearly distinguish. This unclear or blurry surface edge of the small nanoparticle was most dominant where the distance between the two nanoparticles was most near. The two nanoparticles were apart approximately by 8 nm.

Total of 18 time-sequential TEM images were acquired throughout various irradiation time steps as shown in Fig. 6.1.1 and 6.1.2. Upon the irradiation, the particle shrinkage along with specimen edge sublimation were observed, and the irradiation was stopped at 2.78 dpa. The TEM images were later treated by Fast Fourier Transformation (FFT) where two different diffraction patterns corresponding to the larger nanoparticle were spotted. The FFT and the analyzed diffraction patterns from the TEM image are shown in Fig. 6.1.3. Through Inverse Fast Fourier Transformation (IFFT) of the two diffraction patterns, lattice fringe images were acquired. From this IFFT analysis, the interplanar distance was measured from spacing measurements of lattice fringes. The measured interplanar distance of the nanoparticle was 0.26 nm.

From the IFFT of before irradiation TEM image, the existence of structural defects inside the nanoparticle was found. Based on the measurement, initial size of nanoparticle in terms of area was 1630 nm^2. After the irradiation of 2.78 dpa, the area became 1320 nm^2. Based on the acquired IFFT images, time-sequential lattice fringe patterns were acquired as shown in

Fig. 6.1.6 and Fig. 6.1.7. To further analyze the images, dislocation motions during the irradiation are indicated as in Fig. 6.1.8. Based on Fig. 6.1.8, unlike edge dislocations lying on the same slip plane were observed along with dislocation glide motions upon irradiation.

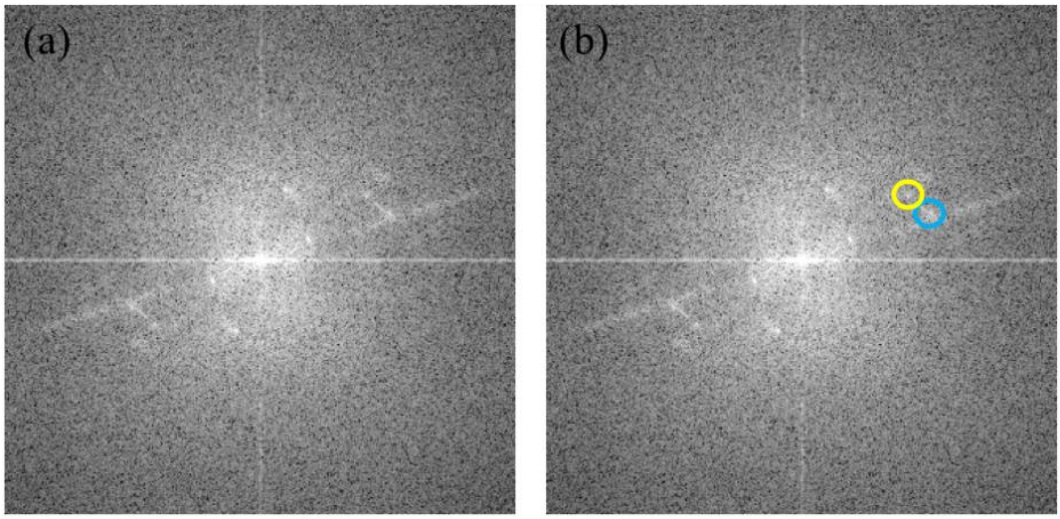

Fig. 6.1.3 (a) FFT image of HRTEM and (b) the two diffraction patterns corresponding to the larger nanoparticle in HRTEM.

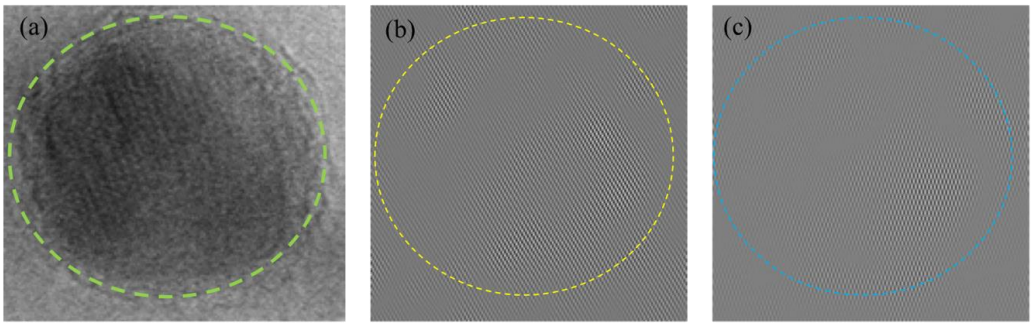

Fig. 6.1.4 (a) HRTEM image of single nanoparticle, (b) the corresponding FFT #1, and (b) the corresponding FFT #2.

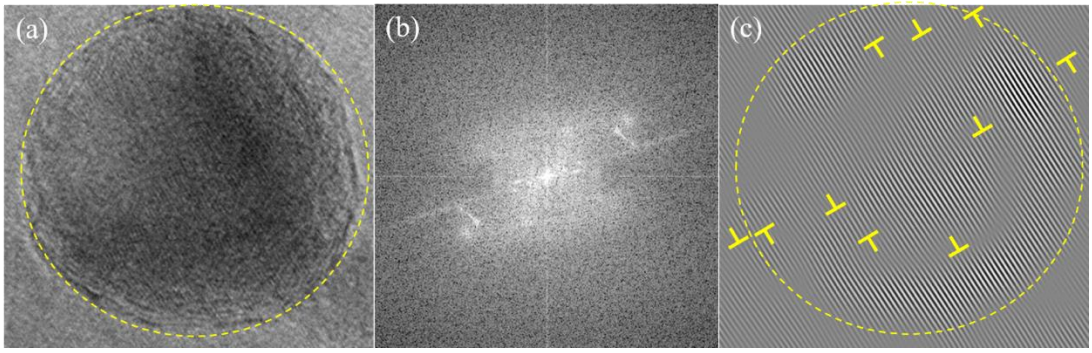

Fig. 6.1.5 (a) HRTEM image of single nanoparticle before irradiation, (b) the corresponding FFT, and (c) IFFT with dislocations being marked.

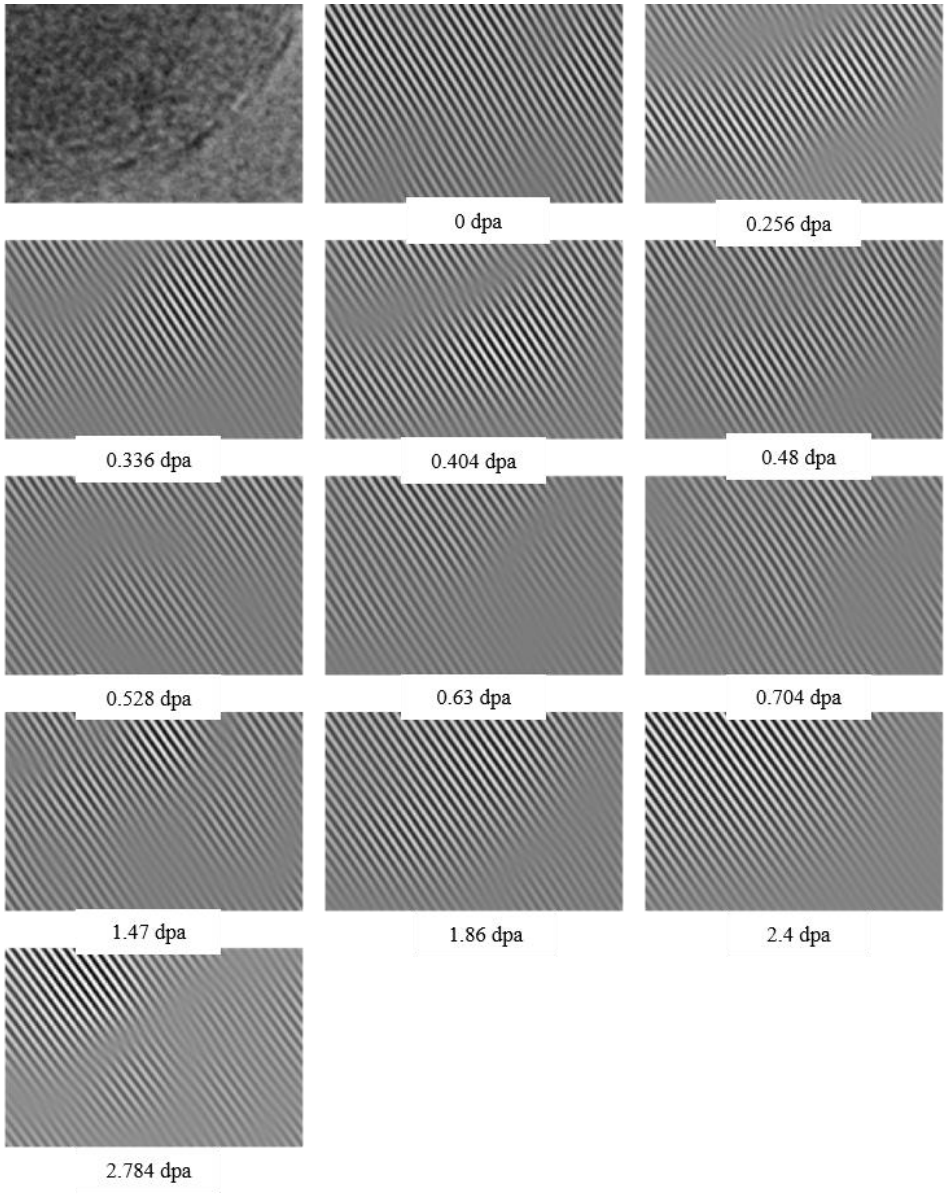

Fig. 6.1.6 Time sequential lattice fringe patterns corresponding to DP #1 for the selected area (bottom right) of the single particle during 1.25 MeV electron irradiation.

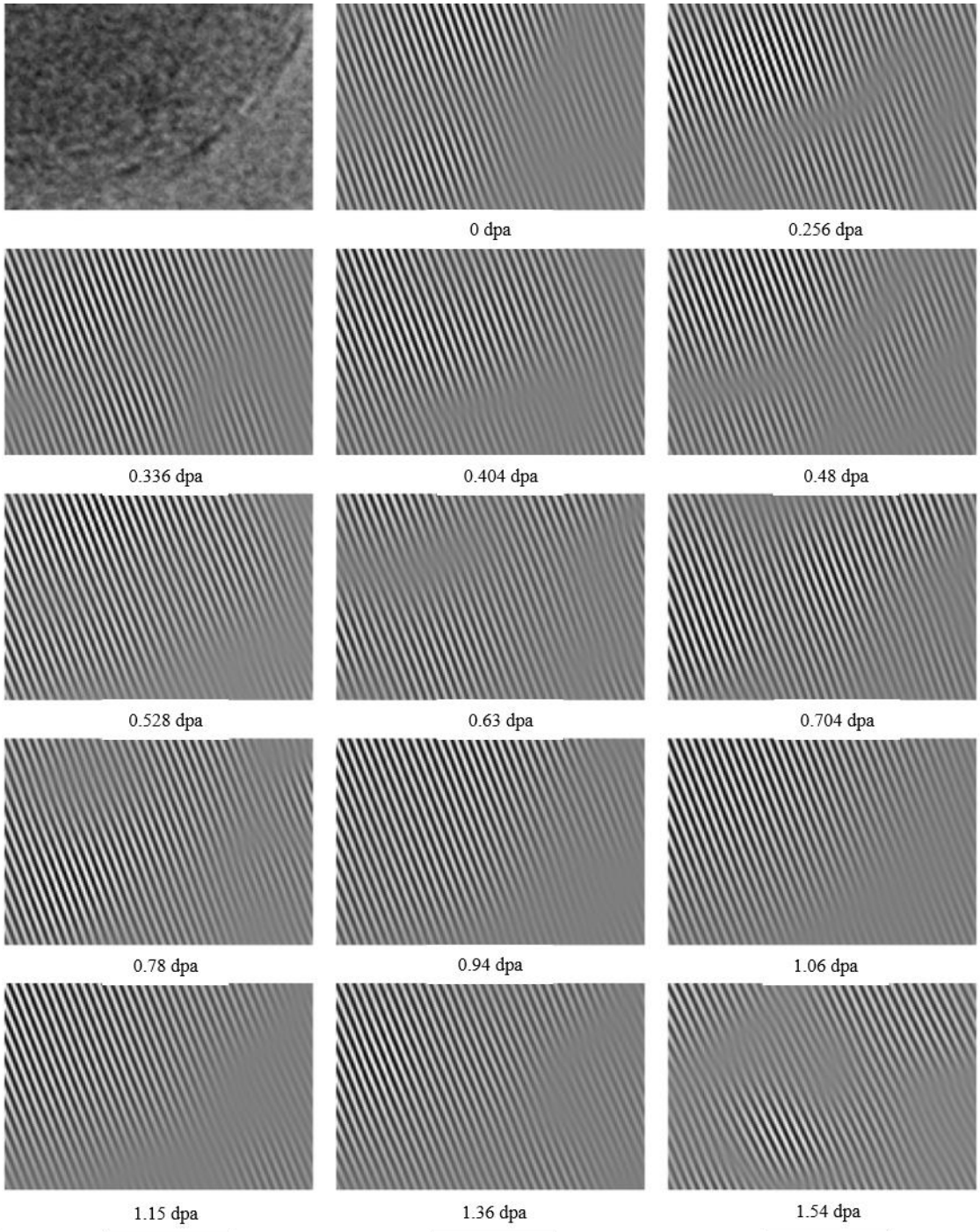

Fig. 6.1.7 Time sequential lattice fringe patterns corresponding to DP #2 for the selected area (bottom right) of the single particle during 1.25 MeV electron irradiation.

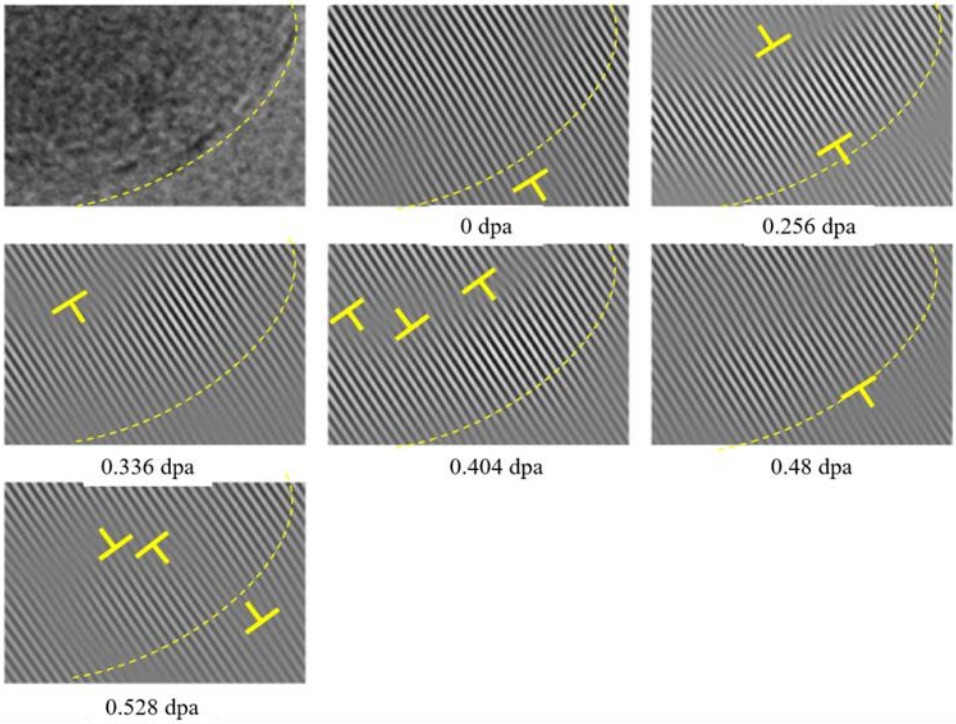

Fig. 6.1.8 Dislocation motions during 1.25 MeV electron irradiation at 573K.

6.2 Discussion

6.2.1 Dislocation Motion Enhancement

Based on literature, Y_2O_3, Y_2TiO_5, and $Y_2Ti_2O_7$ have the threshold electronic stopping power values being significantly higher than the electronic stopping powers anticipated in fission or fusion reactors. Thus, Y_2O_3, Y_2TiO_5, and $Y_2Ti_2O_7$ are suspected to be stable against irradiation due to their complicated structure and difficulty in dislocation motion inside the structure. As the nanoparticle has complex structure, it contains structural vacancies to achieve electrical neutrality.

However, based on HRTEM images during irradiation, dislocation motions are detected. From the time-sequential lattice fringe patterns, dislocation motions are clearly shown upon irradiation. Upon irradiation, unlike edge dislocations lying on the same slip plane were observed along with dislocation glide.

As the nanoparticle has complex structure, it contains structural vacancies to achieve electrical neutrality as shown in Fig. 6.1.5. Then upon irradiation, while the nanoparticle was shrinking, the dislocation motions were detected inside the nanoparticle. Based on the measurement, initial size of nanoparticle in terms of area was 1630 nm^2. Then, towards the end of the irradiation at 2.78 dpa, the area became 1320 nm^2. This nanoparticle dissolution can be explained by the excess vacancies being introduced during the irradiation which may cause instability. This dislocation motion could create a pathway for solute atoms to easily diffuse in or out of the interface between the precipitate and the matrix.

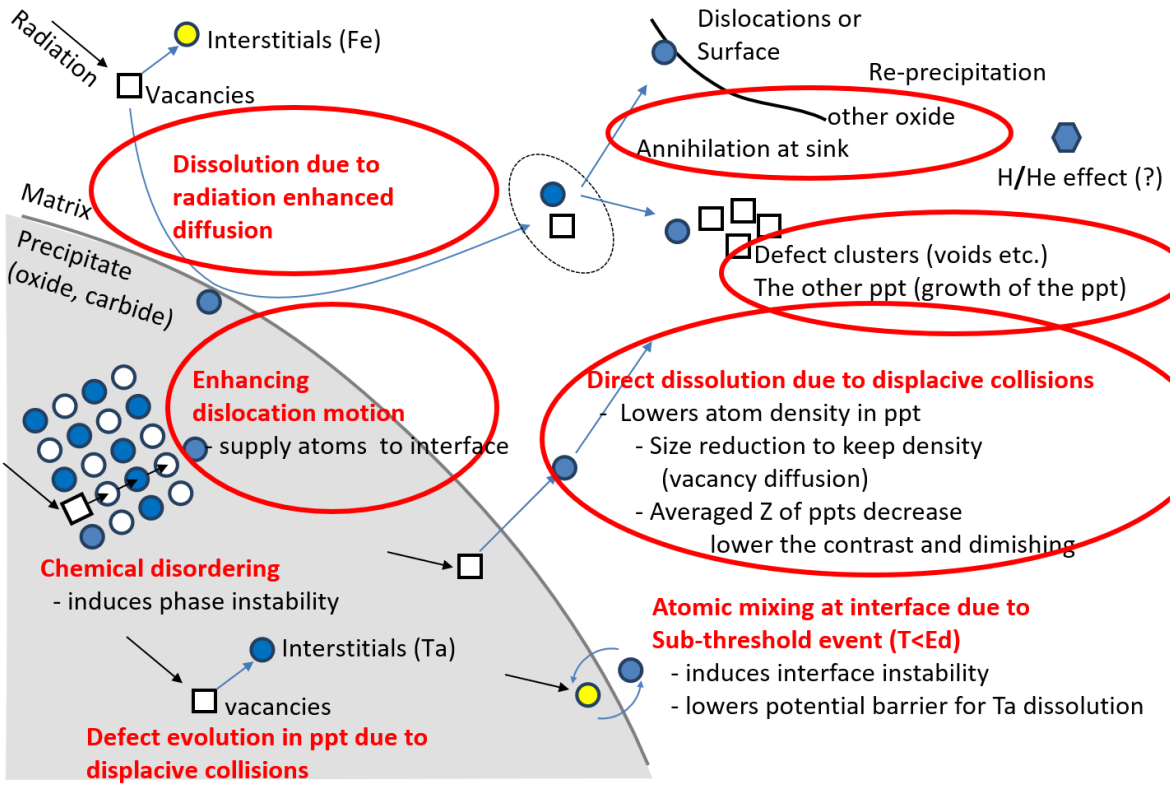

Fig. 6.2.1 Microstructural evolution mechanisms. Various phenomena responsible for particle dissolution.

So far, researchers have suggested various instability mechanisms such as

- Dissolution due to radiation enhanced diffusion
- Direct dissolution due to displacive collisions
- Atomic mixing at interface due to sub-threshold event
- Chemical disordering
- Defect evolution in precipitate due to displacive collisions

According to this experiment, a new mechanism for the particle instability under the irradiation is found: Irradiation induced dislocation motion enhancement. From the in-situ HRTEM analysis, the existing structural defects inside the nanoparticle is confirmed. As the nanoparticle has complex structure, it contains structural vacancy to achieve electrical neutrality. Then upon irradiation, while the nanoparticle was shrinking, the dislocation motions were detected inside the nanoparticle. The excess vacancies being introduced during the

irradiation may cause instability. This dislocation motion could create a pathway for solute atoms to easily diffuse in or out of the interface between the precipitate and the matrix. The irradiation induced dislocation motion enhancement is concluded to be a mechanism for the particle dissolution.

The two detected diffraction patterns could indicate that the nanoparticle is composed of two layers and has shell-like structure. Through Inverse Fast Fourier Transformation (IFFT) analysis, the change in interplanar distance of 0.26 nm was found from spacing measurements of lattice fringes.

Also, the full lattice coherency between the oxide nanoclusters and the Fe matrix gives rise to a very low interface energy between the two disparate materials, oxide and metal. The low interface energy, along with the very low solubility of O and Y in bcc Fe, can effectively prevent the coarsening of the oxide precipitates. Moreover, the intrinsic defective structure of the nanoclusters can naturally tolerate the radiation-induced damage. Therefore, the ODS steels with a large number of defective nanoprecipitates represent a novel material state, which is intrinsically distinct from conventional nano-phase materials, which are usually metastable and can rapidly become coarsened at high temperatures.

CHAPTER 7

Conclusion

Oxide Dispersion Strengthened (ODS) steels are promising structural material for fusion reactors due to both excellent mechanical strength and irradiation resistance. A high number density of the dispersed Y-Ti-O nanoparticles, mainly $Y_2Ti_2O_7$ and Y_2TiO_5, embedded in the Fe-Cr matrix contributes to enhancement in high-temperature creep strength and irradiation resistance. To implement ODS steels in fusion reactors like DEMO, the stability of the Y-Ti-O nanoparticles under high-temperature irradiation is critical. According to previous literature, based on different radiation sources and the chemical composition of the irradiated materials, the radiation response of the nanoparticles differed. For instance, under neutron irradiation on 13Cr-ODS steel, nanoparticles were stable; while under electron and Fe^{+2} ion irradiations on 9Cr-ODS steel, nanoparticles were shrinking. To clarify the radiation response of nanoparticles, three factors were controlled in this research: radiation energy, temperature, and electron beam condition. At different irradiation conditions, microstructural evolutions were closely investigated under in-situ HVEM and - HRTEM.

The microstructural evolutions of Y-Ti-O Nanoparticles in ferritic 12Cr-ODS steel under high energy electron irradiations were investigated using H-3000 at Osaka University. 2 MeV electron energy is used to irradiate the ODS steel. Under 2 MeV electron energy, irradiations were performed at 723K and 823K to investigate the temperature effect on NPs dissolution. Also, under both irradiation temperatures, electron beam conditions - focused and uniform - were controlled to study the vacancy concentration gradient effect on nanoparticles. The focused beam technique was employed to study the effect of vacancy concentration gradient where the electron beam intensity has a Gaussian distribution. The nanoparticles volumetric change under the focused and the uniform beam conditions were compared

throughout the irradiations. Also, for each nanoparticle, both the size and shape evolution were investigated throughout the short-time irradiation steps. Unlike the typically reported monotonic size change of nanoparticles, both rapid growth and shrinkage were observed simultaneously under 723K irradiation in each time step. In both the focused and the uniform beam irradiations, this stochastic size change behavior of nanoparticles at the early irradiation stage is first reported in this study. Thus, the total linear volumetric change of initial to final irradiation is found to be inaccurate to fully describe the microstructural evolution of nanoparticles.

The shape evolution was also observed and represented by eccentricity; the nanoparticles were classified by two different size groups and their eccentricity changes were plotted and compared throughout the irradiation. Based on the size category, the eccentricity of small nanoclusters increased at the final state while eccentricity of larger nanoclusters decreased. This result could indicate that nanoclusters chemical composition varies, and size of nanoclusters can be one of the factors to categorize different composition. Also, the radiation-enhanced diffusion coefficients of Y and Ti are calculated and compared.

Contrary to 723K irradiation results, at 823K uniform irradiation, the radiation-induced growth phenomenon was observed. In 823K irradiation experiment, particle number density was much higher than in 723K irradiation experiment. Thus, in 823K irradiation experiment, large number of nanoparticles were clustered. The growth of nanoparticle was observed only in the clustered region which is defined as the nearest neighboring distance of 5 nm. Also, rapid decrease of particle number density was observed at 823K uniform irradiation. The morphological evolution along with growth was also observed and regardless of initial shape of nanoparticles, the final shape was either cuboidal or polygon. Typical Ostwald ripening phenomena is proven to be inaccurate to fully describe the radiation induced growth of particles. The unique shape evolution of growing nanoparticles is observed and regardless of their initial

shapes, the final shapes were cuboidal or polygon. Interestingly, this radiation-induced growth only appeared under the uniform irradiation at 823K and not at 723K. To further verify the temperature effect, vacancy diffusion coefficients respect to 573, 723, and 823K were plotted and a huge jump between 723K and 823K is found. This result can indicate that there could exist a temperature threshold for the radiation-induced growth.

Lastly, for the in-depth study on the instability mechanism of NPs, the single particle irradiation is performed using JEM-ARM1300 at Hokkaido University. The dissolution mechanism for the NP is investigated using this in-situ High Resolution TEM (HRTEM). In-situ HRTEM irradiation under 1.25 MeV was used for microstructural evolution observation of single nanoparticle at 573K. Prior to irradiation, structural defects were found inside the nanoparticle using HRTEM. Then, upon the irradiation, the particle shrinkage along with specimen edge sublimation were observed, and the irradiation was performed up to 2.78 dpa. From Fast Fourier Transformation (FFT) of the single nanoparticle, diffraction patterns are acquired time-sequentially. Two patterns from the FFT are analyzed and the detected diffraction patterns could indicate that the nanoparticle is composed of two layers with shell-like structure. Area corresponding to the interface between the NP and bulk was selected to closely investigate the dislocation movement under the electron irradiation. Through Inverse Fast Fourier Transformation (IFFT) analysis, the change in interplanar distance was found from spacing measurements of lattice fringes. Based on the analysis, the structural vacancies in the nanoparticle before irradiation are confirmed and irradiation induced dislocation motion enhancement is concluded to be a mechanism for the particle dissolution.

References

[1] IAEA, Climate Change and Nuclear Power 2018, (2018) 1–136. https://www-pub.iaea.org/MTCD/Publications/PDF/CCNAP-2018_web.pdf.

[2] C.J. Rhodes, The 2015 Paris Climate Change Conference: Cop21, Sci. Prog. 99 (2016) 97–104. doi:10.3184/003685016X14528569315192.

[3] S. Matsuda, K. Tobita, Evolution of the ITER program and prospect for the next-step fusion DEMO reactors: Status of the fusion energy R&D as ultimate source of energy, J. Nucl. Sci. Technol. 50 (2013) 321–345. doi:10.1080/00223131.2013.773166.

[4] G. Federici, C. Bachmann, L. Barucca, W. Biel, L. Boccaccini, R. Brown, C. Bustreo, S. Ciattaglia, F. Cismondi, M. Coleman, V. Corato, C. Day, E. Diegele, U. Fischer, T. Franke, C. Gliss, A. Ibarra, R. Kembleton, A. Loving, F. Maviglia, B. Meszaros, G. Pintsuk, N. Taylor, M.Q. Tran, C. Vorpahl, R. Wenninger, J.H. You, DEMO design activity in Europe: Progress and updates, Fusion Eng. Des. 136 (2018) 729–741. doi:10.1016/j.fusengdes.2018.04.001.

[5] M. Windridge, Smaller and quicker with spherical tokamaks and high-temperature superconductors, Philos. Trans. R. Soc. A Math. Phys. Eng. Sci. 377 (2019). doi:10.1098/rsta.2017.0438.

[6] N. Taylor, P. Cortes, Lessons learnt from ITER safety & licensing for DEMO and future nuclear fusion facilities, Fusion Eng. Des. 89 (2014) 1995–2000. doi:10.1016/j.fusengdes.2013.12.030.

[7] F. Soisson, T. Jourdan, Radiation-accelerated precipitation in Fe-Cr alloys, Acta Mater. 103 (2016) 870–881. doi:10.1016/j.actamat.2015.11.001.

[8] G. Bonny, D. Terentyev, L. Malerba, New contribution to the thermodynamics of fe-cr alloys as base for ferritic steels, J. Phase Equilibria Diffus. 31 (2010) 439–444. doi:10.1007/s11669-010-9782-9.

[9] E. Aydogan, N. Almirall, G.R. Odette, S.A. Maloy, O. Anderoglu, L. Shao, J.G. Gigax, L. Price, D. Chen, T. Chen, F.A. Garner, Y. Wu, P. Wells, J.J. Lewandowski, D.T. Hoelzer, Stability of nanosized oxides in ferrite under extremely high dose self ion irradiations, J. Nucl. Mater. 486 (2017) 86–95. doi:10.1016/j.jnucmat.2017.01.015.

[10] T.R. Allen, J. Gan, J.I. Cole, M.K. Miller, J.T. Busby, S. Shutthanandan, S. Thevuthasan, Radiation response of a 9 chromium oxide dispersion strengthened steel to heavy ion irradiation, J. Nucl. Mater. 375 (2008) 26–37. doi:10.1016/j.jnucmat.2007.11.001.

[11] Y. Li, J. Shen, F. Li, H. Yang, S. Kano, Y. Matsukawa, Y. Satoh, H. Fu, H. Abe, T. Muroga, Effects of fabrication processing on the microstructure and mechanical properties of oxide dispersion strengthening steels, Mater. Sci. Eng. A. 654 (2016) 203–212. doi:10.1016/j.msea.2015.12.032.

[12] R.L. Klueh, J.P. Shingledecker, R.W. Swindeman, D.T. Hoelzer, Oxide dispersion-strengthened steels: A comparison of some commercial and experimental alloys, J. Nucl. Mater. 341 (2005) 103–114. doi:10.1016/j.jnucmat.2005.01.017.

[13] T. Muroga, M. Gasparotto, S.J. Zinkle, Overview of materials research for fusion reactors, Fusion Eng. Des. 61–62 (2002) 13–25. doi:10.1016/S0920-3796(02)00219-3.

[14] I. Monnet, P. Dubuisson, Y. Serruys, M.O. Ruault, O. Kaïtasov, B. Jouffrey, Microstructural investigation of the stability under irradiation of oxide dispersion strengthened ferritic steels, J. Nucl. Mater. 335 (2004) 311–321. doi:10.1016/j.jnucmat.2004.05.018.

[15] I. Monnet, T. Van Den Berghe, P. Dubuisson, A comparison between different oxide dispersion strengthened ferritic steel ongoing in situ oxide dissolution in High Voltage Electron Microscope, J. Nucl. Mater. 424 (2012) 204–209. doi:10.1016/j.jnucmat.2012.03.011.

[16] A. Certain, S. Kuchibhatla, V. Shutthanandan, D.T. Hoelzer, T.R. Allen, Radiation stability of nanoclusters in nano-structured oxide dispersion strengthened (ODS) steels, J. Nucl. Mater. 434 (2013) 311–321. doi:10.1016/j.jnucmat.2012.11.021.
[17] C. Lu, Z. Lu, X. Wang, R. Xie, Z. Li, M. Higgins, C. Liu, F. Gao, L. Wang, Enhanced Radiation-tolerant Oxide Dispersion Strengthened Steel and its Microstructure Evolution under Helium-implantation and Heavy-ion Irradiation, Sci. Rep. 7 (2017) 1–7. doi:10.1038/srep40343.
[18] A. Hirata, T. Fujita, Y.R. Wen, J.H. Schneibel, C.T. Liu, M.W. Chen, Atomic structure of nanoclusters in oxide-dispersion-strengthened steels, Nat. Mater. 10 (2011) 922–926. doi:10.1038/nmat3150.
[19] S. Kitaoka, Design, Development, and Applications of Structural Ceramics, Composites, and Nanomaterials: Ceramic Transactions, 244 (2014) 107–118.
[20] S.J. Zinkle, V.A. Skuratov, D.T. Hoelzer, On the conflicting roles of ionizing radiation in ceramics, Nucl. Instruments Methods Phys. Res. Sect. B Beam Interact. with Mater. Atoms. (2002). doi:10.1016/S0168-583X(02)00648-1.
[21] S.J. Zinkle, C. Kinoshita, Defect production in ceramics, J. Nucl. Mater. 251 (1997) 200–217. doi:10.1016/S0022-3115(97)00224-9.
[22] K. Persson, Materials Data on Y2Ti2O7 (SG 227) by Materials Project, (2014). doi:10.17188/1263583.
[23] J. Shen, H. Yang, Y. Li, S. Kano, Y. Matsukawa, Y. Satoh, H. Abe, Microstructural stability of an as-fabricated 12Cr-ODS steel under elevated-temperature annealing, J. Alloys Compd. 695 (2017) 1946–1955. doi:10.1016/j.jallcom.2016.11.029.
[24] H. Sakasegawa, L. Chaffron, F. Legendre, L. Boulanger, T. Cozzika, M. Brocq, Y. de Carlan, Correlation between chemical composition and size of very small oxide particles in the MA957 ODS ferritic alloy, J. Nucl. Mater. 384 (2009) 115–118. doi:10.1016/j.jnucmat.2008.11.001.
[25] H. Sakasegawa, F. Legendre, L. Boulanger, M. Brocq, L. Chaffron, T. Cozzika, J. Malaplate, J. Henry, Y. De Carlan, Stability of non-stoichiometric clusters in the MA957 ODS ferrtic alloy, J. Nucl. Mater. 417 (2011) 229–232. doi:10.1016/j.jnucmat.2010.12.056.
[26] F. Matteucci, G. Cruciani, M. Dondi, G. Baldi, A. Barzanti, Crystal structural and optical properties of Cr-doped Y2Ti2O7 and Y2Sn2O7 pyrochlores, Acta Mater. 55 (2007) 2229–2238. doi:10.1016/j.actamat.2006.11.008.
[27] A. Hirata, T. Fujita, Y.R. Wen, J.H. Schneibel, C.T. Liu, M.W. Chen, Atomic structure of nanoclusters in oxide-dispersion-strengthened steels, Nat. Mater. 10 (2011) 922–926. doi:10.1038/nmat3150.
[28] D.T. Hoelzer, B.A. Pint, I.G. Wright, A microstructural study of the oxide scale formation on ODS Fe-13Cr steel, J. Nucl. Mater. 283–287 (2000) 1306–1310. doi:10.1016/S0022-3115(00)00248-8.
[29] S.J. Zinkle, C. Kinoshita, DefectProductionInCeramics.pdf, J. Nucl. Mater. 251 (1997) 200–217.
[30] I. Monnet, P. Dubuisson, Y. Serruys, M.O. Ruault, O. Kaïtasov, B. Jouffrey, Microstructural investigation of the stability under irradiation of oxide dispersion strengthened ferritic steels, J. Nucl. Mater. 335 (2004) 311–321. doi:10.1016/j.jnucmat.2004.05.018.
[31] F. Li, H. Abe, T. Ishizaki, Y. Li, T. Nagasaka, T. Muroga, T. Nagase, H. Yasuda, Stability of oxide particles under electron irradiation in a 9Cr ODS steel at 400°C, J. Nucl. Mater. 455 (2014) 724–727. doi:10.1016/j.jnucmat.2014.09.011.
[32] T.R. Allen, J. Gan, J.I. Cole, M.K. Miller, J.T. Busby, S. Shutthanandan, S. Thevuthasan, Radiation response of a 9 chromium oxide dispersion strengthened steel

to heavy ion irradiation, J. Nucl. Mater. 375 (2008) 26–37. doi:10.1016/j.jnucmat.2007.11.001.
[33] A. Certain, S. Kuchibhatla, V. Shutthanandan, D.T. Hoelzer, T.R. Allen, Radiation stability of nanoclusters in nano-structured oxide dispersion strengthened (ODS) steels, J. Nucl. Mater. 434 (2013) 311–321. doi:10.1016/j.jnucmat.2012.11.021.
[34] R.E. Stoller, M.B. Toloczko, G.S. Was, A.G. Certain, S. Dwaraknath, F.A. Garner, On the use of SRIM for computing radiation damage exposure, Nucl. Instruments Methods Phys. Res. Sect. B Beam Interact. with Mater. Atoms. 310 (2013) 75–80. doi:10.1016/j.nimb.2013.05.008.
[35] G. Was, Fundamentals of radiation materials science: metals and alloys, Springer International Publishing, 2007.
[36] I.M. Watt, The principles and practice of electron microscopy, Second, Cambridge University Press, 1997.
[37] M.L. Lescoat, J. Ribis, A. Gentils, O. Kaïtasov, Y. De Carlan, A. Legris, In situ TEM study of the stability of nano-oxides in ODS steels under ion-irradiation, J. Nucl. Mater. 428 (2012) 176–182. doi:10.1016/j.jnucmat.2011.12.009.
[38] J. He, F. Wan, K. Sridharan, T.R. Allen, A. Certain, Y.Q. Wu, Response of 9Cr-ODS steel to proton irradiation at 400 °c, J. Nucl. Mater. 452 (2014) 87–94. doi:10.1016/j.jnucmat.2014.05.004.
[39] M.L. Lescoat, J. Ribis, Y. Chen, E.A. Marquis, E. Bordas, P. Trocellier, Y. Serruys, A. Gentils, O. Kaïtasov, Y. De Carlan, A. Legris, Radiation-induced Ostwald ripening in oxide dispersion strengthened ferritic steels irradiated at high ion dose, Acta Mater. 78 (2014) 328–340. doi:10.1016/j.actamat.2014.06.060.
[40] J.P. Wharry, M.J. Swenson, K.H. Yano, A review of the irradiation evolution of dispersed oxide nanoparticles in the b.c.c. Fe-Cr system: Current understanding and future directions, J. Nucl. Mater. 486 (2017) 11–20. doi:10.1016/j.jnucmat.2017.01.009.
[41] H. Abe, N. Sekimura, Y. Yang, Stability and mobility of defect clusters in copper under displacement cascade conditions, J. Nucl. Mater. 323 (2003) 220–228. doi:10.1016/j.jnucmat.2003.08.006.
[42] S. Kano, H. Yang, J. Shen, Z. Zhao, J. McGrady, D. Hamaguchi, M. Ando, H. Tanigawa, H. Abe, Investigation of instability of M 23 C 6 particles in F82H steel under electron and ion irradiation conditions, J. Nucl. Mater. 502 (2018) 263–269. doi:10.1016/j.jnucmat.2018.02.004.
[43] H. Abe, T. Ishizaki, F. Li, S. Kano, Y. Li, Y. Satoh, T. Nagase, H. Yasuda, New Approach to *In Situ* Observation Experiments under Irradiation in High Voltage Electron Microscopes, Mater. Trans. 55 (2015) 423–427. doi:10.2320/matertrans.md201315.
[44] H. Abe, T. Ishizaki, S. Kano, F. Li, Y. Satoh, H. Tanigawa, D. Hamaguchi, T. Nagase, H. Yasuda, Mechanism of instability of carbides in Fe-TaC alloy under high energy electron irradiation at 673 K, J. Nucl. Mater. 455 (2014) 695–699. doi:10.1016/j.jnucmat.2014.08.032.
[45] J. Shen, H. Yang, Z. Zhao, J. McGrady, S. Kano, H. Abe, Effects of pre-deformation on microstructural evolution of 12Cr ODS steel under 1473–1673 K annealing, Nucl. Mater. Energy. 16 (2018) 137–144. doi:10.1016/j.nme.2018.06.002.
[46] Z. Wang, L. Gui, D. Han, Z. Xu, L. Han, S. Xu, Measurement and Evaluation of Local Surface Temperature Induced by Irradiation of Nanoscaled or Microscaled Electron Beams, Nanoscale Res. Lett. 14 (2019). doi:10.1186/s11671-018-2821-x.
[47] J. Shen, Y. Li, F. Li, H. Yang, Z. Zhao, S. Kano, Y. Matsukawa, Y. Satoh, H. Abe, Microstructural characterization and strengthening mechanisms of a 12Cr-ODS steel,

Mater. Sci. Eng. A. 673 (2016) 624–632. doi:10.1016/j.msea.2016.07.030.
[48] C. Hin, B.D. Wirth, Formation of Y2O3nanoclusters in nano-structured ferritic alloys: Modeling of precipitation kinetics and yield strength, J. Nucl. Mater. 402 (2010) 30–37. doi:10.1016/j.jnucmat.2010.04.020.
[49] P. Klugkist, C. Herzig, Tracer diffusion of titanium in α-iron, Phys. Status Solidi. 148 (1995) 413–421. doi:10.1002/pssa.2211480209.
[50] H.H. Potter, The Magneto-Caloric Effect and other Magnetic Phenomena in Iron, Proc. Roy. Soc. A. 146 (1934) 362–387.
[51] S.-R. Oh, S. Kano, H. Yang, J. McGrady, H. Yasuda, H. Abe, In-situ HVEM observation under 2 MeV electron irradiations on Y–Ti–O nanoparticles in 12Cr-ODS steel at 723K, J. Nucl. Mater. 524 (2019) 278–285. doi:10.1016/j.jnucmat.2019.07.009.
[52] R. Finsy, On the critical radius in Ostwald ripening, Langmuir. 20 (2004) 2975–2976. doi:10.1021/la035966d.
[53] Q.B. Wang, F. Robert, H.B. Xu, X. Li, On the critical radius in generalized Ostwald ripening, J. Zhejiang Univ. Sci. 6 B (2005) 705–707. doi:10.1631/jzus.2005.B0705.
[54] K.E. Porter, D. A. Easterling, 4.3 Alloy Solidification, Phase Transformations in Metals and Alloys, (1992). doi:Porter, D. A., and K. E. Easterling. “4.3 Alloy Solidification, Phase Transformations in Metals and Alloys.” (1992).
[55] J.F. Nie, Physical Metallurgy of Light Alloys, Fifth Edit, Elsevier B.V., 2014. doi:10.1016/B978-0-444-53770-6.00020-4.
[56] F.R.N. Nabarro, The influence of elastic constants on the shape of an inclusion, Int. J. Solids Struct. 40 (2003) 4399–4416. doi:10.1016/S0020-7683(03)00183-5.
[57] F.R.N. Nabarro, The strains produced by precipitation in alloys, Proc. R. Soc. London. Ser. A. Math. Phys. Sci. 175 (1940) 519–538. doi:10.1098/rspa.1940.0072.
[58] A.G. Khachaturyan, S. V. Semenovskaya, J.W. Morris, Theoretical analysis of strain-induced shape changes in cubic precipitates during coarsening, Acta Metall. 36 (1988) 1563–1572. doi:10.1016/0001-6160(88)90224-6.
[59] J. Ribis, Y. De Carlan, Interfacial strained structure and orientation relationships of the nanosized oxide particles deduced from elasticity-driven morphology in oxide dispersion strengthened materials, Acta Mater. 60 (2012) 238–252. doi:10.1016/j.actamat.2011.09.042.
[60] Z. Oksiuta, P. Olier, Y. de Carlan, N. Baluc, Development and characterisation of a new ODS ferritic steel for fusion reactor application, J. Nucl. Mater. 393 (2009) 114–119. doi:10.1016/j.jnucmat.2009.05.013.
[61] P. Dou, A. Kimura, T. Okuda, M. Inoue, S. Ukai, S. Ohnuki, T. Fujisawa, F. Abe, Polymorphic and coherency transition of Y-Al complex oxide particles with extrusion temperature in an Al-alloyed high-Cr oxide dispersion strengthened ferritic steel, Acta Mater. 59 (2011) 992–1002. doi:10.1016/j.actamat.2010.10.026.
[62] H. Kim, J.G. Gigax, T. Chen, S. Ukai, F.A. Garner, L. Shao, Dispersoid stability in ion irradiated oxide-dispersion-strengthened alloy, J. Nucl. Mater. 509 (2018) 504–512. doi:10.1016/j.jnucmat.2018.07.015.
[63] T. Stan, Y. Wu, G.R. Odette, K.E. Sickafus, H.A. Dabkowska, B.D. Gaulin, Fabrication and characterization of naturally selected epitaxial Fe-{111} Y2Ti2O7 mesoscopic interfaces: Some potential implications to nano-oxide dispersion-strengthened steels, Metall. Mater. Trans. A Phys. Metall. Mater. Sci. 44 (2013) 4505–4512. doi:10.1007/s11661-013-1827-3.
[64] H. Saito, M. Ueda, Spontaneous magnetization and structure formation in a spin-1 ferromagnetic Bose-Einstein condensate, Phys. Rev. A - At. Mol. Opt. Phys. 72 (2005) 1–7. doi:10.1103/PhysRevA.72.023610.

[65] K. Kim, H.C. Kim, S. Oh, Y.S. Lee, J.H. Yeom, K. Im, G.S. Lee, G. Neilson, C. Kessel, T. Brown, P. Titus, A preliminary conceptual design study for Korean fusion DEMO reactor, Fusion Eng. Des. 88 (2013) 488–491. doi:10.1016/j.fusengdes.2013.02.123.
[66] V.M. Burlakov, M.S. Bootharaju, T.M.D. Besong, O.M. Bakr, A. Goriely, Reversing Ostwald Ripening, (2014) 1–15. http://arxiv.org/abs/1412.6280.
[67] A. Hishinuma, Y. Katano, K. Shiraishi, Dose and temperature dependence of void swelling in electron irradiated stainless steel, J. Nucl. Sci. Technol. 14 (1977) 723–730. doi:10.1080/18811248.1977.9730830.
[68] M. Legkostupov, Variation of the Magnetization of Nickel and Iron at Low Temperatures, Sov. J. Exp. Theor. Phys. 34 (1972) 136.
[69] M. Sigrist, Solid State Theory, Inst. Fur Theor. Phys. Course Notes. (2013) 15–21. doi:10.3390/ijms16048826.
[70] K.H. Heinig, B. Schmidt, M. Strobel, H. Bernas, Inverse ostwald ripening and self-organization of nanoclusters due to ion irradiation, Mater. Res. Soc. Symp. - Proc. 647 (2001). doi:10.1557/PROC-650-R9.6/O14.6.
[71] X. Liu, Y. Miao, M. Li, M.K. Kirk, S.A. Maloy, J.F. Stubbins, Ion-irradiation-induced microstructural modifications in ferritic/martensitic steel T91, J. Nucl. Mater. 490 (2017) 305–316. doi:10.1016/j.jnucmat.2017.04.047.
[72] Y. Gan, K. Mo, D. Yun, D.T. Hoelzer, Y. Miao, X. Liu, K.C. Lan, J.S. Park, J. Almer, T. Chen, H. Zhao, Temperature effect of elastic anisotropy and internal strain development in advanced nanostructured alloys: An in-situ synchrotron X-ray investigation, Mater. Sci. Eng. A. 692 (2017) 53–61. doi:10.1016/j.msea.2017.03.068.
[73] M.J. Swenson, C.K. Dolph, J.P. Wharry, The effects of oxide evolution on mechanical properties in proton- and neutron-irradiated Fe-9%Cr ODS steel, J. Nucl. Mater. 479 (2016) 426–435. doi:10.1016/j.jnucmat.2016.07.022.
[74] W.J. Weber, L.M. Wang, N. Yu, The irradiation-induced crystalline-to-amorphous phase transition in α-SiC, Nucl. Instruments Methods Phys. Res. Sect. B Beam Interact. with Mater. Atoms. 116 (1996) 322–326. doi:10.1016/0168-583X(96)00066-3.
[75] S.J. Zinkle, L.L. Snead, Designing Radiation Resistance in Materials for Fusion Energy, Annu. Rev. Mater. Res. 44 (2014) 241–267. doi:10.1146/annurev-matsci-070813-113627.
[76] F. Granberg, K. Nordlund, M.W. Ullah, K. Jin, C. Lu, H. Bei, L.M. Wang, F. Djurabekova, W.J. Weber, Y. Zhang, Mechanism of Radiation Damage Reduction in Equiatomic Multicomponent Single Phase Alloys, Phys. Rev. Lett. 116 (2016) 1–8. doi:10.1103/PhysRevLett.116.135504.
[77] H. Inui, H. Mori, T. Sakata, H. Fujita, Electron irradiation induced crystalline-to-amorphous transition in quartz single crystals, J. Non. Cryst. Solids. 116 (1990) 1–15. doi:10.1016/0022-3093(90)91039-T.
[78] M. Kiritani, Microstructure evolution during irradiation - Kiritani, 216 (1994) 220–264. http://ac.els-cdn.com/0022311594900140/1-s2.0-0022311594900140-main.pdf?_tid=621fd4ac-adaf-11e4-b9e5-00000aacb360&acdnat=1423193130_371d399caf8e671142e0046369c4a97e.
[79] N. Yoshida, M. Kiritani, Point Defect Clusters in Electron-Irradiated Gold, J. Phys. Soc. Japan. 35 (1973) 1418–1429. doi:10.1143/JPSJ.35.1418.
[80] A. Kawasuso, H. Itoh, T. Ohshima, K. Abe, S. Okada, Vacancy production by 3 MeV electron irradiation in 6H-SiC studied by positron lifetime spectroscopy, J. Appl. Phys. 82 (1997) 3232–3238. doi:10.1063/1.365630.
[81] Y. Satoh, Y. Abe, H. Abe, Y. Matsukawa, S. Kano, S. Ohnuki, N. Hashimoto,

Vacancy effects on one-dimensional migration of interstitial clusters in iron under electron irradiation at low temperatures, Philos. Mag. 96 (2016) 2219–2242. doi:10.1080/14786435.2016.1194533.
[82] T. Liu, L. Wang, C. Wang, H. Shen, H. Zhang, Feasibility of using Y2Ti2O7 nanoparticles to fabricate high strength oxide dispersion strengthened Fe-Cr-Al steels, Mater. Des. 88 (2015) 862–870. doi:10.1016/j.matdes.2015.08.118.
[83] D. Chen, K. Murakami, H. Abe, Z. Li, N. Sekimura, Investigation of interactions between defect clusters in stainless steels by in situ irradiation at elevated temperatures, Acta Mater. 163 (2019) 78–90. doi:10.1016/j.actamat.2018.10.011.
[84] Z.S. Chen, W.P. Gong, T.F. Chen, S.L. Li, Synthesis and characterization of pyrochlore-type yttrium titanate nanoparticles by modified sol-gel method, Bull. Mater. Sci. 34 (2011) 429–434. doi:10.1007/s12034-011-0116-2.
[85] A. Baldan, Progress in Ostwald ripening theories and their applications in nickel-base superalloys, J. Mater. Sci. 37 (2002) 2379–2405. doi:10.1023/A:1015408116016.
[86] Y. Wu, E.M. Haney, N.J. Cunningham, G.R. Odette, Transmission electron microscopy characterization of the nanofeatures in nanostructured ferritic alloy MA957, Acta Mater. 60 (2012) 3456–3468. doi:10.1016/j.actamat.2012.03.012.
[87] Y. Wu, J. Ciston, S. Kräemer, N. Bailey, G.R. Odette, P. Hosemann, The crystal structure, orientation relationships and interfaces of the nanoscale oxides in nanostructured ferritic alloys, Acta Mater. 111 (2016) 108–115. doi:10.1016/j.actamat.2016.03.031.
[88] F. Maury, M. Biget, P. Vajda, A. Lucasson, P. Lucasson, Anisotropy of defect creation in electron-irradiated iron crystals, Phys. Rev. B. 14 (1976) 5303–5313. doi:10.1103/PhysRevB.14.5303.
[89] A.J. Brooks, Z. Yao, M.R. Daymond, H. Yu, M.A. Kirk, Z. Zhou, G. Zhang, Quasi in-situ energy dispersive X-ray spectroscopy observation of matrix and solute interactions on Y-Ti-O oxide particles in an austenitic stainless steel under 1 MeV Kr2+ high temperature irradiation, Acta Mater. 141 (2017) 241–250. doi:10.1016/j.actamat.2017.07.047.
[90] Begoña Gómez-Ferrer, Resistivity Recovery in Fe and FeCr alloys, 1st ed., Springer International Publishing, 2016. doi:10.1007/978-3-319-38857-1.

Acknowledgement

I would like to show my deep gratitude towards my advisor Professor Hiroaki Abe who guided throughout my academic journey at the University of Tokyo. His excellent expertise in a study of radiation damage along with subtle notes of encouragement instilled confidence in me to pursue my study. It has been a real privilege to be a doctoral student under his leadership.

I would also like to thank all of my committee members: Professor Naoto Sekimura, Professor Takayuki Terai, Professor Kenta Murakami, and Professor Dongyue Chen. I am indebted to the outstanding committee members who generously provided detailed suggestions and comments since the pre-defense up to the final defense.

The open-minded discussions with Professor ShoKano, Professor Huilong Yang, and Dr. John McGrady from the Abe laboratory also helped me with the research. Also, special thanks to secretary Ms.Masami Osono who was ever so sweet, and all the lab members.

Final thanks go to my family who always trusted me. My father, mother, and sister infused sweet encouragements in me when I needed the most. I would especially thank my mother, Dr. Eunok Kim, who fervently supported my passion to be in science and engineering since my childhood. I thank her for her time and effort to mentor me.